UNIVERSITY OF OKLAHOMA

GRADUATE COLLEGE

ALTERATIONS IN LAND SURFACE-ATMOSPHERE PROCESSES RESULTING FROM THE 1988 GREATER YELLOWSTONE AREA FIRES

A Dissertation

SUBMITTED TO THE GRADUATE FACULTY

in partial fulfillment of the requirements for the

degree of

Doctor of Philosophy

By

ROBERT C. HALE
Norman, Oklahoma
2004

Downloaded from SHAREOK. Persistent Handle URL: https://hdl.handle.net/11244/718

UMI Number: 3122302

INFORMATION TO USERS

The quality of this reproduction is dependent upon the quality of the copy submitted. Broken or indistinct print, colored or poor quality illustrations and photographs, print bleed-through, substandard margins, and improper alignment can adversely affect reproduction.

In the unlikely event that the author did not send a complete manuscript and there are missing pages, these will be noted. Also, if unauthorized copyright material had to be removed, a note will indicate the deletion.

UMI®

UMI Microform 3122302

Copyright 2004 by ProQuest Information and Learning Company.

All rights reserved. This microform edition is protected against unauthorized copying under Title 17, United States Code.

ProQuest Information and Learning Company
300 North Zeeb Road
P.O. Box 1346
Ann Arbor, MI 48106-1346

© Copyright by ROBERT C. HALE 2004
All Rights Reserved

ALTERATIONS IN LAND SURFACE-ATMOSPHERE PROCESSES
RESULTING FROM THE 1988 GREATER YELLOWSTONE AREA FIRES

A Dissertation APPROVED FOR THE
SCHOOL OF METEOROLOGY

BY



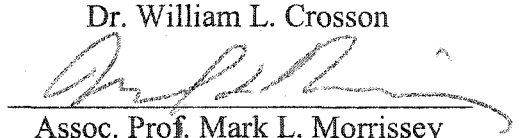
Prof. Emeritus Claude E. Duchon



Prof. William H. Beasley



Dr. William L. Crosson



Assoc. Prof. Mark L. Morrissey



Prof. Baxter E. Vieux

Acknowledgements

The work presented here would not have been possible without the encouragement, guidance, assistance, and support of countless people and organizations. Dr. Claude Duchon, my major advisor, has been an invaluable resource, mentor, and role model throughout my tenure as a graduate student. I could not have asked for a better advisor. Many thanks also are owed to my committee members for their insightful comments and suggestions: William Beasley, William Crosson, Mark Morrissey, and Baxter Vieux. Dr. Crosson has been especially generous with his time in aiding my understanding of the SHEELS model.

Numerous agencies and people provided the input data necessary for running the SHEELS model. Jim Doty and Peter Palmer of the U.S. Bureau of Reclamation, Pacific Northwest Region, were exceptionally helpful in acquiring and understanding Hydromet and AgriMet data. Thanks also to Jim Ashby of the Western Regional Climate Center for his help in acquiring RAWS data and Peter Smith at Goddard Space Flight Center for his clarification of NDVI geographic projections.

Much appreciation is extended to those at the University of Oklahoma that have contributed enormously to this project. The GIS aspects of this research would not have been possible without the considerable assistance provided by Karla Sterling and Dr. May Yuan of the Center for Spatial Analysis, and computational resources were graciously provided by the OU Supercomputing Center for Education and

Research. The School of Meteorology staff, Nancy Agrawal, Celia Jones, and Marcia Pallutto, have not only kept me enrolled and paid, but have made this a much more enjoyable process through their friendship.

This research has been funded in whole through the Canon National Parks Science Scholars Program. I am enormously grateful for the support of this program, and extend my sincere thanks to the participating organizations: Canon USA, Inc.; the National Park Foundation; and the American Association for the Advancement of Science.

Finally, a Ph.D. is not something that can be accomplished without the support of one's friends and family. These people, that have managed to keep me going in the most stressful of times, are too numerous to list, but their encouragement has been invaluable. Most of all, I am indebted to Karla Sterling for all of her love and support over the last three years. I would not have wanted to do this without her.

Table of Contents

Acknowledgements ..... **iv**
List of Figures ..... **viii**
Abstract ..... **xi**
1 Introduction **1**
2 Meteorological Input Data **10**
2.1 Meteorological Data Sources 11
2.1.1 COOP data *13*
2.1.2 SAHASR data *14*
2.1.3 RAWS data *14*
2.1.4 SNOTEL data *15*
2.1.5 Hydromet and AgriMet data *16*
2.2 Data Quality Assurance 17
2.2.1 Quality assurance techniques *19*
2.2.2 Quality assurance of SAHASR data *20*
2.2.3 Quality assurance of RAWS data *21*
2.2.4 Quality assurance of AgriMet data *22*
2.2.5 Quality assurance of Hydromet data *25*
2.2.6 Quality assurance of COOP and SNOTEL data *26*
2.3 Interpolation of Data 27
2.3.1 Temporal aggregation and interpolation *28*
2.3.2 Spatial interpolation of data *31*
2.3.2.1 Temperature and atmospheric pressure *34*
2.3.2.2 Solar radiation *38*
2.4 Modeling of Downwelling Longwave Radiation 41
2.5 Example Meteorological Input Fields 42
3 The SHEELS Model **46**
3.1 Vegetation 47
3.1.1 Land cover type-dependent vegetation parameters *47*
3.1.2 Fractional vegetation cover *50*
3.2 The Soil Column 57
3.2.1 Soil zones and soil layers *57*
3.2.2 Soil property parameters *60*
3.3 Snow Parameterizations 63
3.3.1 Partitioning of precipitation into model snow layers *64*
3.3.2 Age-dependent snow density and albedo *67*
3.4 Model Orography 69
3.5 Modeling of the Surface Energy Budget 71
3.5.1 Radiative fluxes *72*
3.5.2 Turbulent fluxes *74*
3.5.3 Soil moisture *76*

3.5.4 Ground heat flux and soil and snow temperatures *80*
4 Analysis of Model Output for the GYA **84**
4.1 Areas of Comparison and Model Scenarios 84
4.1.1 Control (CTRL) dataset *86*
4.1.2 Vegetation forcing repeated (VFR) dataset *87*
4.1.3 Meteorological forcing repeated (MFR) dataset *88*
4.1.4 Both forcings repeated (BFR) dataset *88*
4.2 Spatially Averaged Time Series 89
4.2.1 Radiative fluxes *90*
4.2.2 Turbulent and ground heat fluxes *96*
4.2.3 Soil water content and snow water equivalent *101*
4.3 Diurnal Averages 106
4.3.1 Surface and canopy temperature *106*
4.3.2 Surface energy budget variables *112*
4.4 Discussion of Results 118
5 Summary **124**
6 Conclusions and Recommendations for Future Research **128**
6.1 Conclusions 128
6.2 Future Research Opportunities 129
7 References **131**

List of Figures

Figure 1. Map of the model domain.

Figure 2. Map of the GYA showing locations of meteorological observation stations.

Figure 3. Distribution of the GYA meteorological observation stations.

Figure 4. Example of temporal interpolation of daily observed temperature using equation 1 as compared to fitting of a sinusoidal curve.

Figure 5. Elevation of the GYA (m).

Figure 6: Regression of 10-year average temperature on elevation for GYA stations reporting at least 5 years quality assured data.

Figure 7: Gridded 8-km resolution input temperature field for (a) midnight local standard time, January 1, 1984 and (b) noon local standard time, July 1, 1984.

Figure 8: Gridded 8-km resolution input (a) downwelling solar radiation and (b) precipitation for noon local standard time, June 21, 1984.

Figure 9: Time series of NDVI spatially averaged over the entire GYA model domain and its associated spatial standard deviation. The time period of the fires is shaded.

Figure 10: Time series of NDVI spatially averaged over the burn area and its associated spatial standard deviation. The time period of the fires is shaded.

Figure 11: Time series of SAVI spatially averaged over the burn area and its associated spatial standard deviation. The time period of the fires is shaded.

Figure 12: Time series of MSAVI2 spatially averaged over the burn area and its associated spatial standard deviation. The time period of the fires is shaded.

Figure 13: Schematic diagram of STATSGO map units, components, and layers.

Figure 14: Predominant wind direction by day of year for the three surface airway stations in the GYA. Based on 1984-1993 observations.

Figure 15: Spatially averaged time series of radiative fluxes over the burn area for a) CTRL, b) MFR, c) VFR, and d) BFR scenarios.

Figure 16: Spatially averaged time series of radiative fluxes over the upwind area for a) CTRL, b) MFR, c) VFR, and d) BFR scenarios.

Figure 17: Spatially averaged time series of radiative fluxes over the downwind area for a) CTRL, b) MFR, c) VFR, and d) BFR scenarios.

Figure 18: Spatially averaged time series of turbulent and ground heat fluxes over the burn area for a) CTRL, b) MFR, c) VFR, and d) BFR scenarios.

Figure 19: Spatially averaged time series of turbulent and ground heat fluxes over the upwind area for a) CTRL, b) MFR, c) VFR, and d) BFR scenarios.

Figure 20: Spatially averaged time series of turbulent and ground heat fluxes over the downwind area for a) CTRL, b) MFR, c) VFR, and d) BFR scenarios.

Figure 21: Spatially averaged time series of soil liquid water content and snow water equivalent over the burn area for a) CTRL, b) MFR, c) VFR, and d) BFR scenarios.

Figure 22: Spatially averaged time series of soil liquid water content and snow water equivalent over the upwind area for a) CTRL, b) MFR, c) VFR, and d) BFR scenarios.

Figure 23: Spatially averaged time series of soil liquid water content and snow water equivalent over the downwind area for a) CTRL, b) MFR, c) VFR, and d) BFR scenarios.

Figure 24: Diurnally averaged surface and canopy temperatures over the burn area for a) CTRL, b) MFR, c) VFR, and d) BFR scenarios.

Figure 25: Diurnally averaged surface and canopy temperatures over the upwind area for a) CTRL, b) MFR, c) VFR, and d) BFR scenarios.

Figure 26: Diurnally averaged surface and canopy temperatures over the downwind area for a) CTRL, b) MFR, c) VFR, and d) BFR scenarios.

Figure 27: Diurnally averaged surface energy budget variables for the month of August over the burn area for a) CTRL, b) MFR, c) VFR, and d) BFR scenarios.

Figure 28: Diurnally averaged surface energy budget variables for the month of August over the upwind area for a) CTRL, b) MFR, c) VFR, and d) BFR scenarios.

Figure 29: Diurnally averaged surface energy budget variables for the month of August over the downwind area for a) CTRL, b) MFR, c) VFR, and d) BFR scenarios.

Figure 30: Map of initial bottom soil layer temperatures (°C).

Abstract

During the late summer of 1988, wildland fires in Yellowstone National Park and the surrounding Greater Yellowstone Area (GYA) burned approximately 570,000 ha, an area about 10% larger than the state of Delaware. The dramatic alteration in land cover resulting from these fires coupled with the availability of surface and satellite data necessary for modeling land surface-atmosphere processes provides an ideal opportunity to study the effects of fire-induced vegetation changes on surface energy budget variables and soil moisture.

Meteorological observations for the 10-year period 1984 to 1993 have been collected from 178 stations within the GYA, quality assured, and spatially and temporally interpolated to produce gridded data suitable for model input. These data comprise 8-km resolution hourly values of seven meteorological variables: near-surface air temperature, relative humidity, precipitation, wind speed, atmospheric pressure, and downwelling solar and longwave radiation.

New algorithms for modeling of snow and frozen soil have been implemented in the Simulator for Hydrology and Energy Exchange at the Land Surface (SHEELS) model. These added capabilities, necessary for using the SHEELS model in the GYA, allow for the hydrologic, thermal, and albedo effects of snow cover and frozen soil to be realized in model output.

The SHEELS model was then used to examine time series and diurnal averages of surface energy budget and soil moisture variables before and after the 1988 fires. Four datasets of these variables were produced for each of three regions within the Greater Yellowstone Area: a burn area consisting of fire-affected regions, an area upwind of the burn area, and an area downwind from the burn area. The four datasets provide a basis for differentiation among possible causes of any observed alterations in surface energy budget or soil moisture variables and result from varying the model forcing by using either observed or repeated inputs of vegetation and meteorological data. Repeated input means that observations from before the fires were used as input in the model both before and after the fires.

Substantial alterations of the latent and sensible heat fluxes were found to result from the removal of vegetation by the 1988 fires. Specifically, latent heat flux was decreased and sensible heat flux increased in the burn area. Furthermore, these effects also were seen downwind of the burn area, indicating that regional climate may have been affected by the fires. Soil moisture was not substantially affected by the fire-induced vegetation changes, however.

1 Introduction

Wildland fires in the United States are relatively frequent summertime occurrences resulting from both natural and anthropogenic causes. Between 1960 and 2000 such fires affected an average of 1.6 million hectares each year, roughly half of which resulted from lightning and half resulted from accidental or intentional human ignition [National Interagency Fire Center (NIFC), 2002]. These fires have substantial environmental and societal impacts, including: changes in regional flora and fauna; fire-induced weather phenomena; increased particulate loading in the atmosphere and hydrosphere; economic costs from fire suppression, structural losses, and reduced tourism revenues; and loss of human life.

The fire season of 1988 proved exceptional in terms of total area burned and economic losses. Nationally, 3.0 million hectares (182% of normal) burned in 1988. A considerable portion of the total, 570,000 ha, was attributable to several fires in the vicinity of Yellowstone National Park (Christensen et al., 1989). Popularly dubbed "the Yellowstone fires," the burned regions actually comprised tracts within Grand Teton National Park, six national forests, and two national wildlife refuges in addition to Yellowstone. The region encompassing the fires is the Greater Yellowstone Area (GYA) which, for the purposes of this study, will be defined as extending from 42° to 46° north latitude and 108° to 114° west longitude (figure 1), and includes portions of Montana, Idaho, and Wyoming.

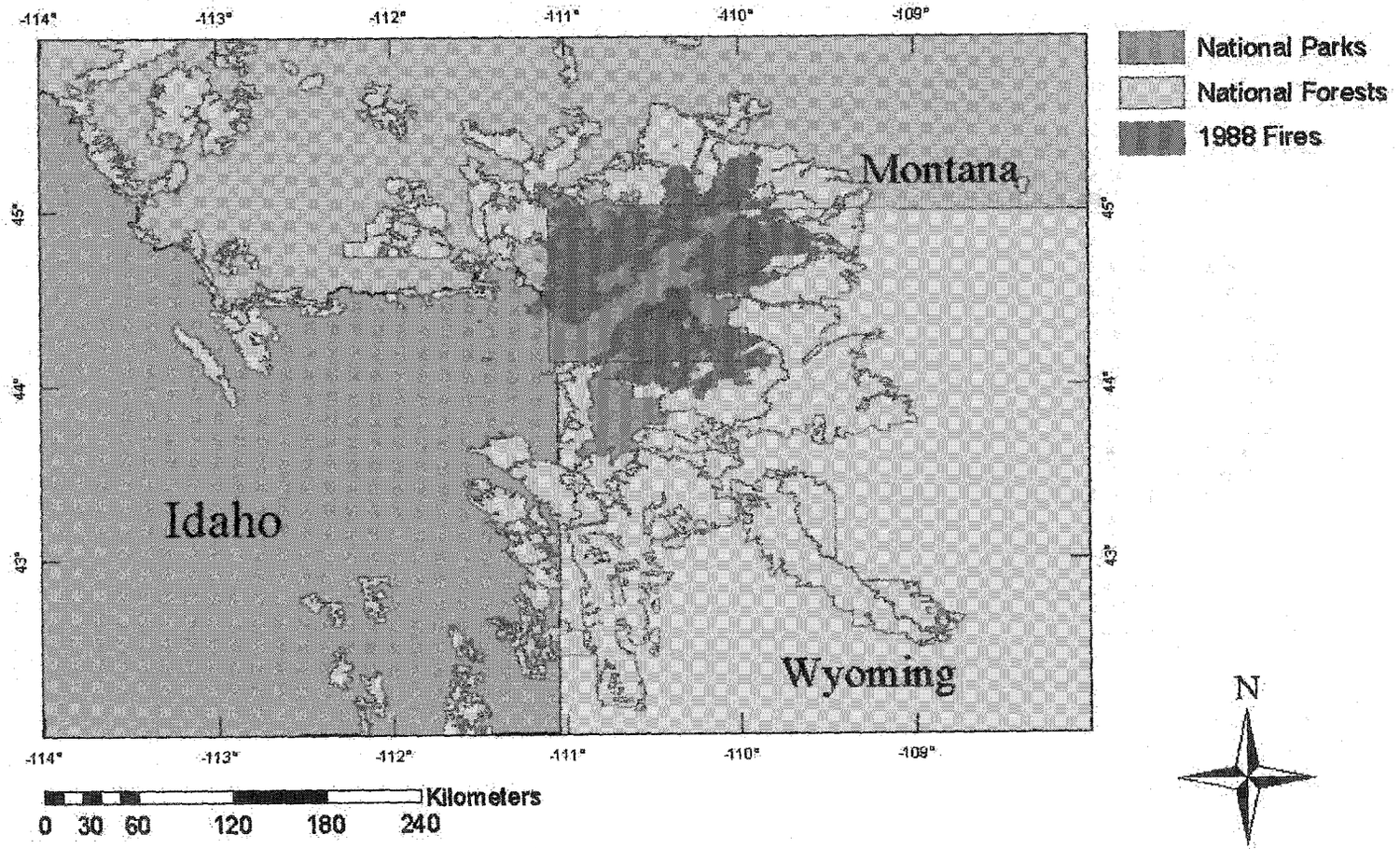


Figure 1: Map of the model domain.

Due to their proximity within and near the world's oldest and possibly most recognized national park, these fires garnered much media attention and sparked heated controversy over the fire management policies of the National Park Service and other federal agencies. For 100 years, fires in Yellowstone National Park were actively suppressed (often unsuccessfully) in attempts to limit the apparent damage they caused (Taylor, 1974). Growing ecological research, however, indicated that fire is a necessary and beneficial aspect of many natural landscapes. An often-presented example of this is the adaptation present in some lodgepole pine (*Pinus contorta* var. *latifolia*) trees causing them to produce serotinous cones. These cones are sealed with resin which prevents seed dispersal until after the cones have been heated through fire exposure (Lotan, 1975). Research has also shown that fire suppression practices can increase fuel loads, resulting in higher burn intensities than would normally occur under natural fire regimes (Allen et al., 2002). It should be noted, however, that Romme and Despain (1989) have used fire scar dendrochronology to argue that fires similar in intensity and spatial extent to those of 1988 have occurred in the GYA prior to policies of suppression, and that suppression likely did not result in exceptionally high fuel loads in 1988, but rather simply delayed an inevitable large-scale burn.

In light of new appreciation for the positive impacts of wildland fires, and following a shift in National Park Service goals toward maintenance of "biotic associations"

(Leopold et al., 1963), a natural burn policy was implemented in limited areas of Yellowstone in 1972, and then revised in 1976 to include most of the park (National Park Service, 1991). The natural burn policy precluded suppression attempts of any fires of natural origin that did not threaten human life or property and were substantially within the park boundaries. Of the seven fires that accounted for 95% of the burned area in the GYA in 1988, three were human-caused, and thus actively suppressed from the time of their discovery. Further, park personnel and Secretary of the Interior Donald Hodel decided to suspend the natural burn policy in Yellowstone in July of 1988 after only 6800 ha had burned (Schullery, 1989). Thus, contrary to public perception, the vast majority of the area burned in the GYA occurred in spite of determined attempts at suppressing the fires, with suppression costs estimated at $120 million (Schullery, 1989).

While socially and politically controversial, the 1988 GYA fires provided tremendous scientific research opportunities due both to their magnitude and their location within a relatively pristine natural setting. This, combined with immense political pressures resulting from perceived mismanagement, resulted in numerous studies examining the fires' consequences. Franke (2000) reports that over 250 investigations of fire effects in the GYA have been initiated since 1988. The majority of these are focused on the biological and ecological implications of wildland fires, including effects on indigenous mammals (e.g. Pearson et al., 1995; Wu et al., 1996), aquatic wildlife (e.g. Mihuc and Minshall, 1995; Minshall et al., 2001), and regional flora (e.g. Singer and Harter, 1996; Romme et al., 1997; Nyland, 1999).

Studies resulting from the 1988 GYA fires have not been limited to ecology alone, however. A considerable number of projects have been undertaken to examine the hydrologic effects of the fires. Generally, these have explored changes in water quality (e.g. Lathrop, 1994) or erosion and sediment transport (e.g. Marston and Haire, 1990; Meyer et al., 1992; Ewing, 1996; Meyer and Wells, 1997). McIntyre and Minshall (1996) assessed changes in river hydrograph response following the fires. They found an increase of 4-8% in annual runoff of the two main rivers in the GYA. Also, peak runoff occurred two days earlier following the fires as a result of the decrease in hydraulic roughness brought about by fire-induced removal of vegetation.

A few researchers considered the fires from a more climatological perspective. Influences of regional climate on fire frequency and severity in the GYA are to be expected since antecedent precipitation, wind speed, relative humidity, and temperature all affect the likelihood of fire ignition and growth (Deeming et al., 1977). Balling et al. (1992) investigated historical climate and fire records in Yellowstone National park and found that between 1895 and 1989 there were trends towards warmer summers and drier spring and summer seasons. These trends were significantly correlated with an increase in each fire season's total burned area. They also examined effects on temperature, precipitation, and evapotranspiration resulting from a two-fold increase in atmospheric carbon dioxide concentration using several general circulation models (GCMs). While precipitation amounts were generally

greater in the GYA with doubled carbon dioxide concentration, increased temperatures resulted in greater evapotranspiration that more than offset the precipitation surplus. They argue that the consequent intensification of aridity in the area, coupled with higher temperatures, supports continued amplification of wildland fire frequency and spatial extent.

It should be noted that studies such as the above, which examine the influence of climate on fire regime, are not limited to the GYA fires. For instance, Wotton and Flannigan (1993) considered Canadian boreal forests and estimated that climate changes brought about by a doubling of atmospheric carbon dioxide would result in a 20% increase in annual burn area and a lengthening of the fire season by about 30 days. Goldammer and Price (1998), studying the tropics, and Piñol et al. (1998), studying Europe, found similar links between predicted changes in future climate and fire frequency and extent.

Though some research has been conducted to assess the effects of tropical biomass burning on atmospheric radiation properties and concomitant changes in global climate (e.g. Andreae, 1993), effects of wildland fires on regional climate have remained relatively unexplored. The paucity of research is especially pronounced if one is interested in decadal-scale changes in soil moisture and energy and water fluxes resulting from fire-induced vegetation changes. It is widely accepted that changes in evapotranspiration and surface albedo accompany land cover changes (Shukla and Mintz, 1982; Dickinson et al., 1993). Thus, alterations of radiation

budgets, latent and sensible heat fluxes, and soil moisture might be reasonably expected following the changes in land cover brought about by the 1988 GYA fires.

In addition to the direct effects of land cover change on surface energy budget components and soil moisture, previous research has also demonstrated that albedo changes and soil moisture anomalies can in turn affect regional precipitation. Charney (1975) suggested that desert areas and persistence of drought in the Sahel are partially a result of such positive feedback mechanisms. He argued that reduced precipitation would result in less vegetation, and the subsequent higher surface albedo would ultimately lead to sinking atmospheric motion and further reduction in precipitation. Walker and Rowntree (1977) expanded on this idea by proposing that soil moisture anomalies might also persist in the absence of albedo changes due to consequent anomalies in evapotranspiration. Using the UK Meteorological Office 11-layer atmospheric model, they found that even with albedo effects excluded, desert areas received more precipitation when initialized with moist soils.

The positive feedback mechanism between soil moisture and precipitation has also been studied at midlatitudes. Dirmeyer (1994) used a land-atmosphere model coupled to a GCM to examine the effects of vegetation dormancy and soil moisture anomalies on precipitation over an idealized midlatitude continent. He found that the reduced evapotranspiration associated with dormant vegetation or dry soil can lead to severe drought conditions. Further, the combined effects of dormant vegetation and dry soil were larger than the sum of each acting alone. Koster et al. (2000) have

found that knowledge of soil moisture conditions can significantly increase precipitation predictability in extra-tropical regions. In the United States, this relationship between soil moisture and precipitation is especially pronounced in a region extending from the Gulf of Mexico, through the Central Plains, and into the Pacific Northwest, including the GYA.

The goal of this research is to establish the degree to which land cover changes resulting from the 1988 fires in the Greater Yellowstone Area affected regional climatologies of soil moisture and components of the surface energy budget. It is hypothesized that the removal of vegetation by the fires would have resulted in decreased latent heat fluxes, increased sensible heat fluxes, and drier soils. It is additionally hypothesized that if decreases in latent heat flux did in fact occur, the consequent drying of the atmosphere over the burned areas could alter precipitation and cloudiness over both the burned areas and areas directly downwind. These changes in regional climate could further impact surface energy budget and soil moisture variables. Modifications of soil moisture and surface energy budget variables, coupled with the above-described atmospheric feedback mechanisms, could have a profound impact on the hydrologic cycle over local spatial scales. Land cover change-induced alterations of precipitation and evapotranspiration would in turn have biological implications in the form of post-fire ecosystem succession and potential societal implications in terms of fire management policy. For instance, the reduction of vegetation by wildland fires might cause a several-year-long increase in aridity that would favor species adapted to dry environments (xerophytic species) during the

period of ecological succession. Such a change could also lead to drying of previously unburned fuels and a positive feedback mechanism that promotes additional fires.

For this research, the Simulator for Hydrology and Energy Exchange at the Land Surface (SHEELS) model (Smith et al., 1993) has been employed to determine soil moisture and surface energy budget variables over the GYA for the period 1984-1993. SHEELS is a numerical land-atmosphere model that simulates fluxes of heat and water within the soil and between the soil and overlying atmosphere based on input of near-surface measurements of standard meteorological variables, soil properties, orography, and satellite-derived vegetation coverage. Modeling results from the approximately five-year period before the 1988 fires have been compared with those after the fires for various climatological and land cover forcing scenarios.

The assembling of high-quality datasets of the meteorological input variables required to run SHEELS is discussed in chapter 2. Chapter 3 provides an overview of SHEELS and the modifications that have been made to allow for modeling of snow and frozen soil processes. Also considered in this chapter are the non-meteorological model inputs and their sources. Descriptions of the different forcing scenarios and analyses of results are presented in chapter 4 with conclusions of this research in chapter 5.

2 Meteorological Input Data

A significant aspect of this research study has involved compiling the necessary input data required to run the SHEELS model over the GYA for the 10-year period 1984-1993. Due to the large spatial extent of the GYA, data have been collected within the area by a variety of federal agencies and at different time scales. In all, over twenty million meteorological observations have been used in this study. This chapter describes the aggregation of these data from their varied sources into high-quality, coherent maps of suitable spatial and temporal resolution for input into the SHEELS model. Horel et al. (2002) report a similar effort to utilize meteorological data from the myriad networks across the western U.S. for producing high resolution fields of meteorological variables. Unfortunately, their undertaking deals with data extending only as far back as 1997. The 1984-1993 period of study necessitated that such data fields be generated specifically for this research.

SHEELS requires input of seven meteorological variables: air temperature, relative humidity, atmospheric pressure, wind speed, solar radiation, downwelling longwave radiation, and precipitation. The first section of this chapter describes sources of the meteorological data that will be used. Quality assurance techniques applied to the data and interpolation of the data to produce gridded fields are discussed in sections 2.2 and 2.3, respectively. Section 2.4 describes the methods used in modeling

downwelling longwave radiation. Examples of gridded fields of meteorological inputs are presented in section 2.5.

2.1 Meteorological Data Sources

In order not to bias results through sudden inclusion or cessation of data from specific observation platforms, only meteorological stations with periods of record encompassing the entire 1984-1993 study interval are utilized in creating the model input datasets, with one exception to be noted later. While this excluded a considerable number of stations from use, 178 stations within the GYA were found to have adequate periods of record for use in this research (figure 2). These data sources are summarized in Table 1 and a description of each follows.

Table 1: Surface meteorological observation networks in the GYA.

Dataset**	Agency	# of Stations	Temporal Resolution	Measured Variables+
COOP	NWS	122*	Daily	T_{max}, T_{min}, T_{obs}, P
COOP	NWS	34*	Hourly	P
SAHASR	NWS	3	Hourly	T, RH, p, U, dir, P, kdn
RAWS	BLM/USFS	9	Hourly	T, RH, p, U, dir, P
SNOTEL	NRCS	16	Daily	T_{max}, T_{min}, T_{avg}, P
Hydromet	USBR	18	15 min	T, P
Agrimet	USBR	1	15 min	T, RH, P, U, kdn

+ T = temperature; T_{max} = daily maximum temperature; T_{min} = daily minimum temperature; T_{avg} = average daily temperature; T_{obs} = temperature at time of observation; RH = relative humidity; p = pressure; U = wind speed; dir = wind direction; P = precipitation; kdn = solar radiation

* Some COOP hourly precipitation sites are colocated with daily observation sites. The total number of geographically distinct COOP sites in the GYA is 131.

** See following pages for acronym definitions.

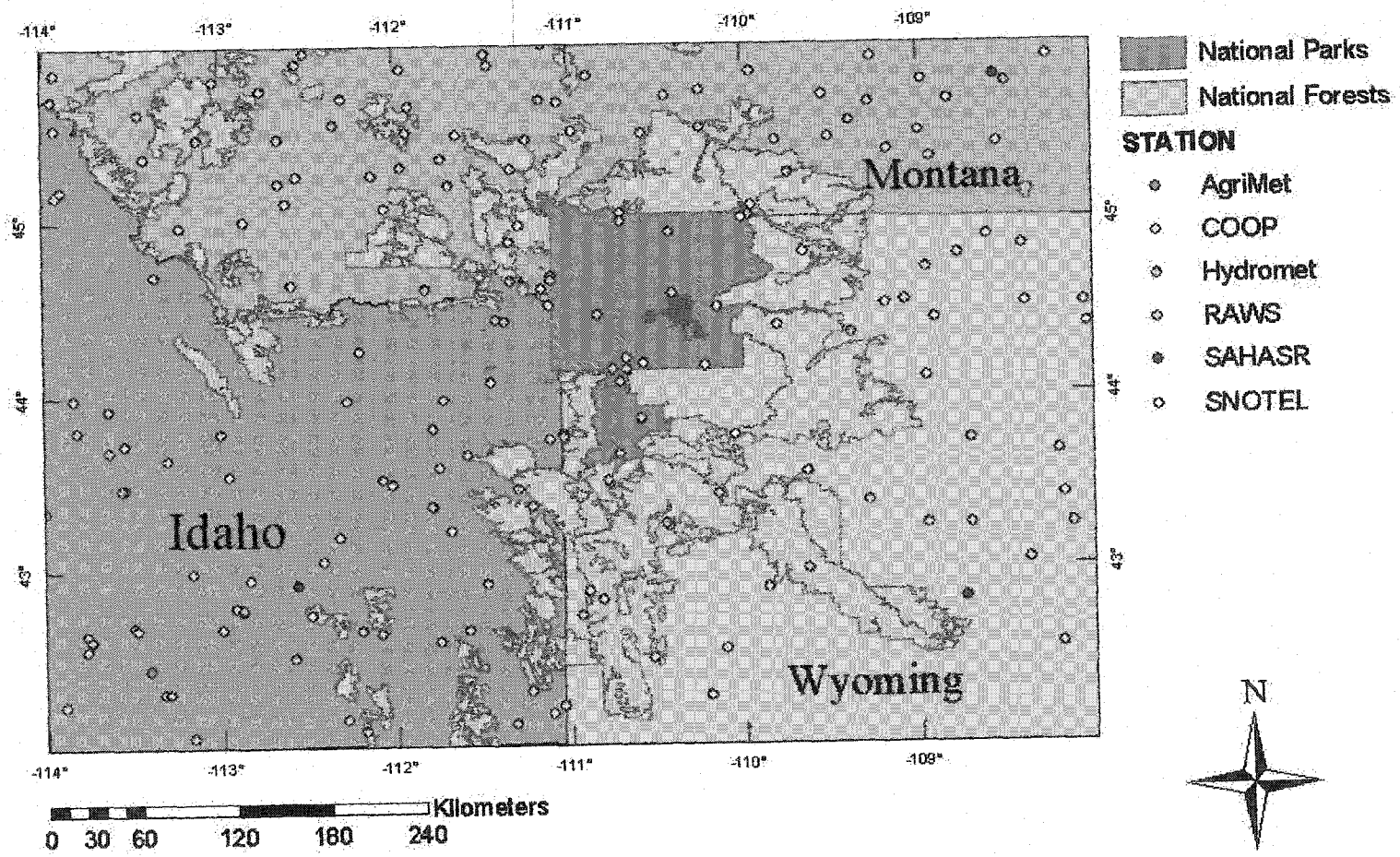


Figure 2: Map of the GYA showing locations of meteorological observation stations.

2.1.1 COOP data

Established in 1890, the National Weather Service (NWS) Cooperative Observer Program (COOP) comprises roughly 11,700 volunteers recording daily weather observations throughout the United States (NWS, 2000). Observations generally include daily maximum and minimum temperature and daily cumulative precipitation (rain or snow water equivalent). Some stations also report snow depth on a daily basis. In addition to these daily observations, many COOP platforms include automated 15-minute precipitation measurements. Such measurements may be made at a daily observation station or at a separate station where the precipitation measurements are the only meteorological data. Daily observations and 15-minute precipitation measurements are archived by the National Climatic Data Center (NCDC).

With 131 stations within the GYA during 1984-1993, the COOP network is the most spatially dense source of meteorological data used in this research. Of the 131 stations, 97 provide only daily observations, 9 provide 15-minute precipitation only, and the remaining 25 have both daily observations and 15-minute precipitation data. While the spatial density of the COOP network is quite high, temporal resolution (daily for most observations) is rather poor.

2.1.2 SAHASR data

In addition to the COOP network, the NWS oversees meteorological observations at many airports in the U.S. Modernization in 1996 introduced the Automated Surface Observing System (ASOS), but prior to that many airports still reported hourly Surface Airway Observations (SAOs). Measurements of atmospheric temperature, pressure, relative humidity, wind speed and direction, precipitation, and direct and diffuse solar radiation have been archived by NCDC as Surface Airway Hourly and Airway Solar Radiation (SAHASR) data. Airports within the GYA for which SAHASR data exist for the 1984-1993 period of study include Billings, Montana, Lander, Wyoming, and Pocatello, Idaho. While only three stations are located within the GYA, SAHASR data are valuable in their fine temporal resolution, high data quality, and as one of only two sources of measured solar radiation. Unfortunately, archiving of solar radiation data was discontinued after 1990. The paucity of solar radiation data necessitated its modeling over the GYA domain, as will be discussed in section 22.3..2.

2.1.3 RAWS data

As pointed out in the introduction, wildland fires have dramatic effects in the United States, especially in the West. Monitoring and suppression efforts, as well as fire behavior modeling, are heavily reliant upon knowledge of meteorological conditions in fire-prone areas. To address this need, the U.S. Bureau of Land Management (BLM) and the U.S. Forest Service (USFS) have deployed approximately 1500

Remote Automated Weather Stations (RAWS) to monitor atmospheric temperature, pressure, relative humidity, wind speed and direction, and precipitation. Data from these stations are transmitted to the National Interagency Fire Center (NIFC) and archived at an hourly time step by the Western Regional Climate Center (WRCC).

The GYA contains nine RAWS with periods of record spanning the majority of 1984-1993. Unlike other meteorological datasets used in this study, however, RAWS data are not available for the entire 10-year period. Installation of RAWS in the GYA occurred during early to mid-1985, thus precluding their use in the first year of this study. The high temporal frequency of observations and the remote, high-altitude location of these stations make them particularly valuable to improving the overall quality and representativeness of the meteorological dataset. For these reasons, RAWS measurements have been included despite the lack of data for 1984.

2.1.4 SNOTEL data

The Natural Resource Conservation Service (NRCS) of the U.S. Department of Agriculture (USDA) maintains a network of over 600 stations to monitor snowpack in mountainous regions for the purpose of water supply forecasting. Since 1980, these Snow Telemetry (SNOTEL) sites have collected daily measurements of minimum, maximum, and average temperature, precipitation, and snow water equivalent. The measurements are transmitted back to one of two master stations using meteor burst technology, in which VHF radio signals are reflected off ionized meteoritic particles

of the ionosphere. The data are then pooled at the NRCS National Water and Climate Center in Portland, Oregon, and archived by the WRCC.

As with the COOP data, the temporal resolution of archived SNOTEL data is rather poor. Like RAWS sites, however, SNOTEL sites are mainly located in high-altitude locations. COOP stations, which provide the majority of meteorological observations in the GYA, are generally located at lower elevations where human observers are more likely to reside. The average elevation of the 131 COOP stations used in this study is 1608 m, whereas the average elevation of the nine RAWS sites is 2090 m and that of the 16 SNOTEL sites is 2408 m. Thus, the RAWS and SNOTEL networks provide needed data for what would otherwise be underrepresented areas within the GYA domain.

2.1.5 Hydromet and AgriMet data

The Pacific Northwest Region of the U.S. Bureau of Reclamation (USBR) is charged with water resource management in the Columbia and Snake River basins. To aid decisions in flood control, power generation, and other water uses, the USBR has deployed approximately 300 observation platforms at dams, rivers, and in mountainous regions. These Hydromet platforms measure temperature, precipitation, and snow water equivalent (along with other hydrologic variables) at 15-minute intervals. Data are then archived at the regional office in Boise, Idaho. 18 Hydromet

stations within the GYA have archived data covering the 1984-1993 period and have been used in this study.

In addition to monitoring water supply and reservoirs with Hydromet stations, the USBR Pacific Northwest Region also maintains a network of AgriMet observation platforms designed for agricultural applications, such a crop water use modeling. There are over 50 AgriMet stations, but only a single location within the GYA had a sufficient period of record to provide data for 1984-1993. A key aspect of this station is archived 15-minute measurements of solar radiation for the years 1985-1993. This archive thus provides the only solar radiation data for 1991-1993, and contains data from one of four sites in the GYA with solar radiation measurements for 1985-1990.

2.2 Data Quality Assurance

Utilizing meteorological data from a variety of sources increases the spatial density of the observations, as well as reducing biases that may be inherent in any one particular dataset. For example, since the period of interest in this study predates the deployment of the ASOS network, SAHASR data have been archived only for stations located at airports of fairly substantial size. Thus, all of the latter data are from urban areas at fairly low elevation (relative to the surrounding terrain of the GYA). COOP sites, while often in more rural areas, are again confined to the lower elevations at which volunteer observers are likely to reside. Conversely, SNOTEL sites, designed for measuring snowpack in mountainous regions, and RAWS sites,

designed for fire weather monitoring, are located in remote areas and at higher elevations. Figure 3 shows the distribution of the 178 stations in terms of longitude and elevation, making evident the elevational biases of the different observation networks. Clearly it is advantageous to use as many networks as possible to ensure a meteorological dataset that is representative of the GYA domain.

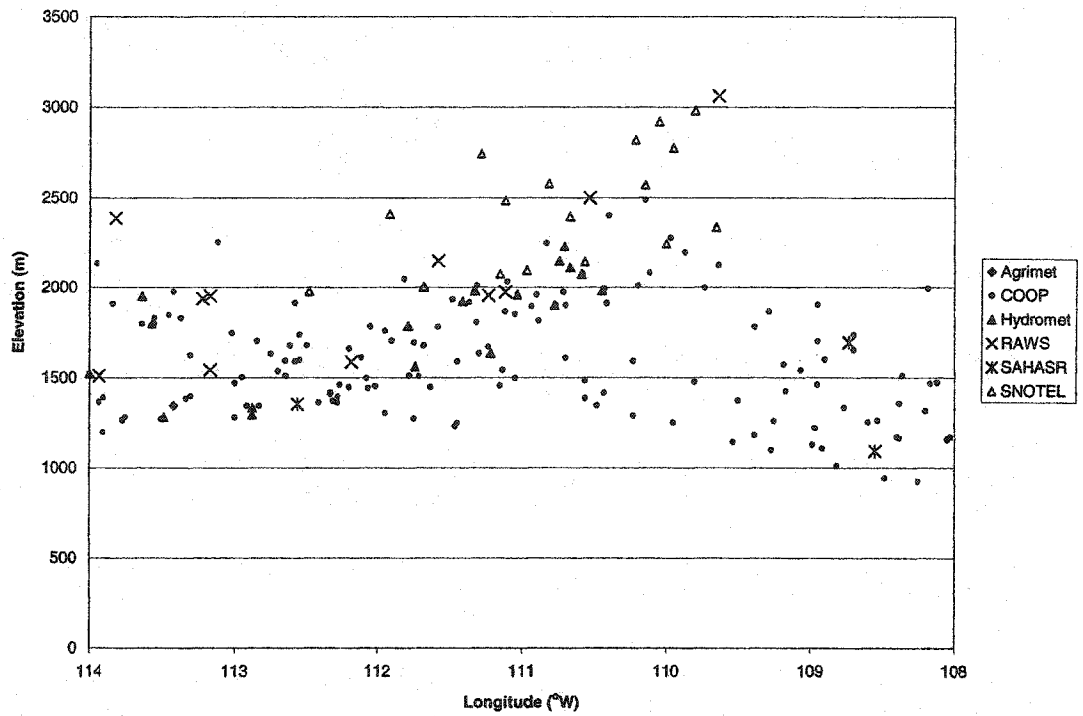


Figure 3: Distribution of the GYA meteorological observation stations.

Unfortunately, use of multiple observation networks introduces difficulties in preparing a high-quality dataset for model input. First, data provided by some of the above-described networks (RAWS, SNOTEL, AgriMet, and Hydromet) are considered provisional, and as such have not had any quality control standards applied to them. Second, data from each of the networks are provided in substantially

different formats. Third, the various networks provide data at differing temporal resolution ranging from 15 minutes to one day. The error identification techniques used in the quality assurance process for this research and descriptions of their application to the various SHEELS model meteorological inputs are provided below.

2.2.1 Quality assurance techniques

Shafer et al. (2000) describe several techniques used in automated quality assurance of data provided by the Oklahoma Mesonet. Three of these techniques have been used here: a range test, a step test, and a spatial test.

In the range test, data are examined to ensure that they fall within expected minimum and maximum values. Depending on the network and variable, some observations were initially compared to a set of elimination thresholds, for which an observation was automatically excluded if the maximum or minimum values were exceeded. For example, negative values of precipitation or downwelling solar radiation were automatically eliminated. If the observation was not compared to or excluded by elimination thresholds, it was compared to a set of warning thresholds. If the value fell outside the warning maximum and minimum, the observation was manually examined to determine if it was most likely an erroneous value, or a bona fide extreme occurrence.

The step test verifies that temporal changes in a variable at a single station are physically plausible. A maximum allowable rate of change is selected, and occurrences of the measured change exceeding this value are considered to be indicative of errors. No elimination thresholds were used in the step test, only warning thresholds. That is, if the time rate of change of an observation exceeded a specified amount, a warning was generated and the observation was manually checked to determine its quality.

The spatial test involves comparing a meteorological observation to values taken at nearby stations. This is accomplished by using a single-pass Barnes (1973) objective analysis to create a spatially interpolated field of a variable using observations from the other stations in the GYA (see section 2.3.2 for a more complete description of the Barnes objective analysis technique). The value of the interpolated field at the location of the station being checked is then compared with the measured value. If the difference between the two exceeded a predetermined amount, the measured value was manually checked.

2.2.2 *Quality assurance of SAHASR data*

Due to their location at major airports, stations used in the SAHASR dataset are generally well-maintained and provide high-quality observations. No elimination flags were used in the range test, such that all suspect data were manually examined to determine their quality. The automated quality assurance software generated 98

warnings, the majority of which (64) were for suspect pressure observations at the Lander, Wyoming site. Upon examination, these were found to be individual hours in which the reported pressure was a physically unrealistic value. In these instances, the pressure was replaced by interpolating from the hour before to the hour after the bad observation. Eleven of the 98 warnings were for observations of zero solar radiation during daytime hours at Lander. These were changed to -999 to indicate bad or missing data. Other flags were generated by the step test for large hour-to-hour changes in relative humidity at Lander and the Billings, Montana site.

2.2.3 Quality assurance of RAWS data

While similar to SAHASR in terms of automated collection of data, RAWS sites are generally located in rugged terrain where routine maintenance is difficult. Malfunctions in sensors, data loggers, and archiving all contribute to erroneous data. 4188 warning flags were generated in performing quality assurance on the RAWS data. The majority of these, however, were attributable to persistent temperature observations of -50 °C. While missing data in the SAHASR dataset are given a value of 99, 999, or 9999 (depending on the variable), -50 °C appears to be the default value used for missing temperature data in the RAWS dataset, although this is not documented. This example demonstrates that variations in how different networks deal with missing observations complicates the task of quality assurance. As mentioned above with the SAHASR data, differences in reporting of missing data can even exist for each of the variables observed in a single network.

Of the remaining flags generated for the RAWS dataset, roughly half were for physically unrealistic values that were immediately eliminated. Indicative of such cases were 216 instances of the reported temperature exceeding 100 °C and 86 reports of wind speeds in excess of 100 ms^{-1}. The remaining flags were more thoroughly checked by examination of time series of the flagged variable and comparison to other pertinent measurements. For example, a sudden increase in relative humidity that failed the automated step check might be determined to be "good" if accompanied by the onset of precipitation and a decrease in temperature. In questionable cases, a conservative approach was utilized by eliminating the flagged data. All RAWS data deemed to be of poor quality or erroneous were replaced with a value of -999 and not used in the subsequent spatial interpolation process.

Excluding the -50 °C temperature reports, approximately 10% of the flagged data were determined to be of good quality. These primarily consisted of early-morning, winter temperature observations at high elevation stations occasionally falling slightly below the -35 °C warning threshold.

2.2.4 Quality assurance of AgriMet data

With only one AgriMet station in the GYA, it would seem that quality assurance would be simplified. Unfortunately, lack of documentation regarding collection and archiving of data makes quality assurance quite problematic. For instance, time

stamps are attached to all data representing the local time of collection, which is changed for observance of daylight savings time. However, the change between tagging data with daylight savings time versus standard time was not always an automated process, and could depend upon when the system administrator manually made the change, of which there is no record (P. Palmer, personal communication). Thus, it is possible for the time of collection to be off by one hour for up to a day following daylight savings time changes. Undocumented changes in the reporting frequency of the AgriMet site between 5-minute intervals and 15-minute intervals further complicated the temporal averaging of the AgriMet data required to produce hourly data.

Quality assurance of AgriMet precipitation data was critical due to the use of an unheated tipping bucket rain gauge. Unlike other rain gauges used in this project which are either heated tipping bucket or weighing gauges, the AgriMet station gauge is unable to measure frozen precipitation accurately. In addition, there exists the potential for frozen precipitation to remain in the gauge funnel until the air temperature warms enough for it to melt. This can create perceived precipitation spikes when actually no precipitation is occurring. To alleviate these problems, AgriMet precipitation data were removed for any period during which the air temperature was less than 2 °C, and subsequently for the duration of any non-zero precipitation observations. That is, precipitation had to be reported as zero following a period of sub-2 °C air temperature before non-zero observations were kept. This prevented inclusion of melt water from trapped frozen precipitation.

Due the relatively low elevation (1344 m) of the Malta, Idaho AgriMet site, the lower warning threshold for temperature observations was set to -20 °C instead of the more commonly used threshold of -35 °C. Approximately 15 hourly observations per year were flagged as a result of this higher threshold, all of which were determined to be good data.

Of the 2058 warning flags generated for the AgriMet data, the vast majority were for solar radiation observations. Of these, 48% resulted from non-zero nighttime values, which were replaced with zero. Daytime values of zero comprised 12% of the solar radiation warnings, and these were eliminated. While 28% of the flags were generated by the step test, these often coincided with times for which other flags were issued. A lone nighttime value of 600 Wm^{-2}, for example, would result in the generation of three flags: one for a non-zero nighttime value, one for the 600 Wm^{-2} increase from the previous time step, and one for the 600 Wm^{-2} decrease to the next time step. The final 12% of the solar radiation warnings were for observations exceeding the 1100 Wm^{-2} maximum threshold, all of which were eliminated.

Fourteen precipitation warnings and 51 wind speed warnings were generated by the quality assurance software for the AgriMet dataset. All but one of the precipitation observations and a few of the wind speed observations were determined to be erroneous and eliminated.

2.2.5 *Quality assurance of Hydromet data*

As is the case with the AgriMet network, Hydromet stations transmit their data to a central ingest facility via satellite. Transmission difficulties may result in missing data or garbled data which are then archived. While noticeable in performing quality assurance on the single AgriMet station used in this research, obviously unrealistic data were rampant in the data from the 18 Hydromet stations used. Consequently, elimination thresholds were used in range tests of temperature and precipitation observations. Even with the automatic elimination of some data, over 10,000 warnings were generated by the quality assurance software for manual examination. Fortunately, most of these consisted of substantial periods of time for which temperature observations, although falling within the elimination thresholds, were obviously in error. For example, there is an approximately one-month period during April and May of 1989 in which the reported air temperature at the Huckleberry Divide, Wyoming site does not exceed -40 °C. There were, however, some instances of temperatures slightly below the -35 °C warning threshold that, through graphical examination of time series, were determined to be good data and consequently kept.

Precipitation data accounted for only 235 of the over 10,000 quality assurance warnings. Upon manual examination, all of these were deemed to be bad data and removed. It should be noted that in addition to the 235 precipitation warnings, over 2500 precipitation observations were automatically removed as a result of exceeding the 100 mm in 15 minutes elimination threshold.

2.2.6 *Quality assurance of COOP and SNOTEL data*

While the COOP and SNOTEL networks differ significantly in terms of station location and manual versus automated data collection, these networks are similar in the data they provide – daily maximum and minimum temperature and cumulative precipitation. Thus, quality assurance procedures were comparable for both networks.

Regarding the quality of COOP network data, the NCDC (2003) states:

> "These data have received a high measure of quality control through computer and manual edits. These data are subjected to internal consistency checks, compared against climatological limits, checked serially, and evaluated against surrounding stations.... In November 1993 the entire historical period of record was processed through a stringent quality control. Another round of quality control in November 2000 increased the data set's quality still more."

In spite of this, COOP data have a reputation for being of questionable quality, due in large part to collection by human observers with minimal training (aside from the automated collection of 15-minute precipitation data at some sites). SNOTEL data, although collected with automated digital sensors, have had no previous quality assurance standards applied.

Complicating quality assurance for both these networks is the fact that observations are made daily, rather than hourly. This limits the effectiveness of step tests on

temperature observations, as a large threshold must be used since significant day-to-day fluctuations in temperature are not uncommon. For COOP and SNOTEL data, step tests were performed by comparing daily maximum temperature from one day to the next, and likewise for daily minimum temperature. Daily maxima were not compared to daily minima.

In addition to the automatic elimination of daily precipitation accumulations greater than 3 inches, temperatures greater than 120 °F, and temperatures less than -50 °F, over 250 quality assurance warning flags were generated for the COOP and SNOTEL data. Each of these warnings was then manually checked, and 32 were finally determined to be caused by erroneous data. In some cases, these errors apparently resulted from interchange of the daily maximum and minimum temperatures during recording or archiving. The remaining warning flags were mostly for large day-to-day decreases in maximum temperature. Manual examination of these cases often revealed that such decreases were primarily found at higher elevation stations during the fall or spring and accompanied by precipitation and similar temperature decreases at nearby stations. These data suggest passage of cold fronts rather than erroneous observations, and were consequently left in the dataset.

2.3 Interpolation of Data

The SHEELS model requires input of gridded meteorological variables at hourly time intervals. Once quality assurance standards had been applied to the observations

collected from the six networks in the GYA and suspect data had been removed, temporal aggregation and interpolation were then performed to produce hourly data for each observing site. The hourly data were then spatially interpolated to produce the 8-km resolution gridded fields needed for model input.

2.3.1 Temporal aggregation and interpolation

Of the sources being used, only the RAWS, surface airway, and COOP hourly precipitation networks provide hourly data. Hydromet and AgriMet data, with 15-minute resolution, were temporally aggregated to hourly data by means of averaging (temperature, relative humidity, wind speed, and solar radiation) or summation (precipitation). Daily measurements from COOP and SNOTEL sites, however, required temporal interpolation to obtain hourly data suitable for SHEELS input.

Temperature data from COOP and SNOTEL sites include daily maximum and minimum temperature as well as temperature at the time of observation (COOP) or daily average temperature (SNOTEL). Unfortunately, time of occurrence of the maximum and minimum temperatures was not recorded. To alleviate this problem, the three nearest sites for which hourly or 15-minute temperature data are recorded (i.e. the nearest RAWS, surface airway, AgriMet, or Hydromet station) is found. Of these, the closest site with less than six hours of missing data for the day being interpolated is utilized in temporal interpolation of the COOP or SNOTEL

temperature data. If none of the three closest hourly recording sites has at least 18 hours of data, the daily observations from COOP or SNOTEL are not used.

First, the time of occurrence of the maximum and minimum value at the COOP/SNOTEL station is taken as the same as that for the nearby station. While it then would be possible to temporally interpolate between the maximum and minimum by fitting a sinusoid to these values, diurnal temperature cycles are rarely sinusoidal, especially at high latitudes where the number of daylight hours often differs significantly from 12. This has the potential to skew daily heating and cooling curves. To make temporally interpolated temperatures at COOP and SNOTEL sites more realistic, changes between the times of maximum and minimum were assumed to follow temperature changes at the nearest site with hourly or 15-minute data. Letting ΔT be the difference between the previous maximum or minimum and the subsequent minimum or maximum at any given time step, the change in temperature at the COOP or SNOTEL site is scaled by the ratio of ΔT at that site to ΔT at the nearest site with hourly (or 15-minute) measurements. This can be expressed as

$$T_{daily}^{N} = T_{daily}^{N-1} + \left(T_{hourly}^{N} - T_{hourly}^{N-1}\right)\frac{\Delta T_{daily}}{\Delta T_{hourly}} \qquad (1)$$

where subscripts "daily" indicate temperatures at stations where only daily maximum/minimum temperature are recorded and subscripts "hourly" indicate the temperature at the nearby hourly recording station. An example of results from this methodology as well as from a simple sinusoidal curve is shown in figure 4 using

min/max data from the Whiskey Creek SNOTEL site on July 25, 1984. Occurrence of maximum and minimum values at 0445 and 1700 LST, respectively, and the shape of the interpolated temperature curve are based on the nearby Valley View Hydromet site.

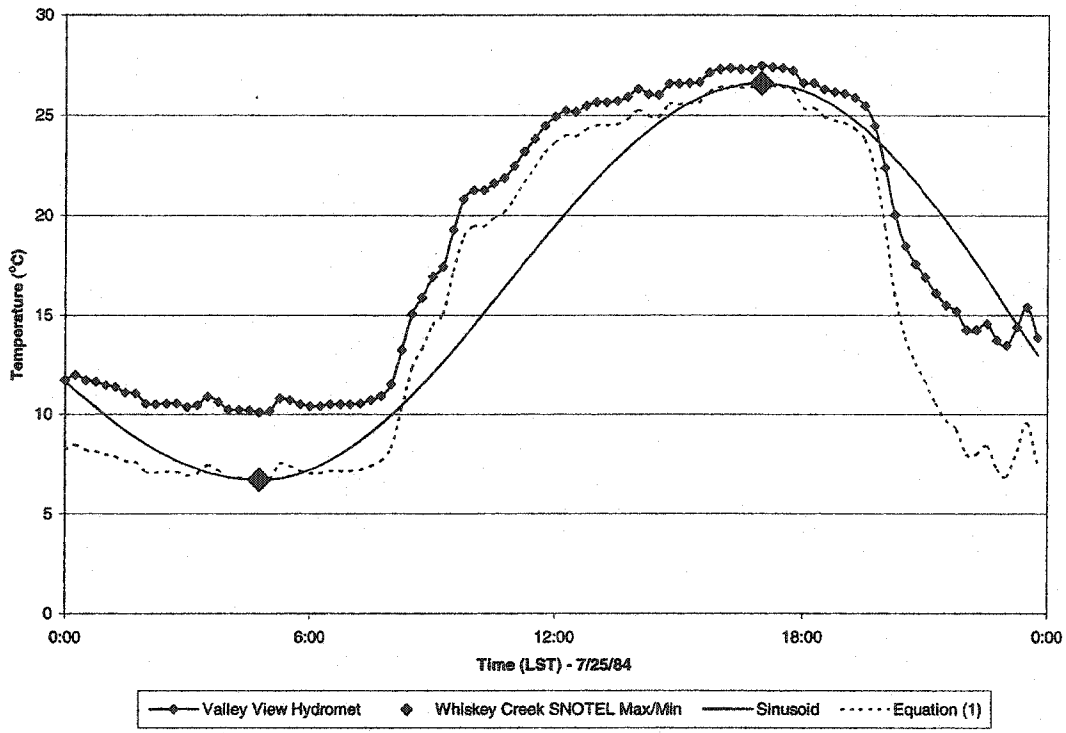


Figure 4: Example of temporal interpolation of daily observed temperature using equation 1 as compared to fitting of a sinusoidal curve.

Daily cumulative precipitation from COOP and SNOTEL sites has been temporally interpolated in a manner similar to that used for temperature. However, it is possible for precipitation to not occur at any of the three nearby hourly recording stations. In these instances, a constant precipitation rate is assumed throughout the day to account for the COOP or SNOTEL accumulation.

2.3.2 *Spatial interpolation of data*

Several methods have been developed to perform objective analysis, the production of regularly spaced fields of a variable from irregularly spaced observations. These range from relatively simple schemes in which weighting of observations is based solely on the distances of observations from a grid point (e.g. Cressman, 1959; Barnes, 1964) to more complex schemes in which weighting factors are influenced by observation density, expected observational errors, and dynamic constraints (e.g. Lorenc, 1981; DiMego, 1988). In light of the large amount of data to be spatially interpolated (seven meteorological variables over 87,672 time steps), the technique of Barnes (1973) will be used to minimize computational expense. This 1973 version allows interpolation with only two passes, compared to several passes required for convergence using Barnes' 1964 version.

Using temperature as an example, the first pass determines the temperature at grid point (x, y) by

$$T_I(x,y) = \frac{\sum_{i=1}^{M}(w_i T_i)}{\sum_{i=1}^{M} w_i} \qquad (2)$$

where T_i is the i-th of M observed temperatures and w_i is the weighting factor

$$w_i = exp(\frac{-d_i^2}{4\kappa}). \qquad (3)$$

In (3), d_i is the distance from the observing station to grid point (x, y) and κ is a parameter that determines the detail in the interpolated field (i.e. the filter response function). The second-pass temperatures are then produced using the first-pass temperatures $T_1(x, y)$ as a background field and reducing the parameter κ by a factor γ ($0 < \gamma < 1$) such that:

$$T_2(x,y) = T_1(x,y) + \frac{\sum_{i=1}^{M} w_i'\left(T_i - T_1(x,y)\right)}{\sum_{i=1}^{M} w_i'} \tag{4}$$

$$w_i' = exp\left(\frac{-d_i^2}{4\gamma\kappa}\right) \tag{5}$$

Values of γ near 1 result in smoothed values of $T_2(x, y)$ while values near 0.2 or less act to capture more detail. In this manner, γ establishes the goodness of fit of the interpolated field to the observations. Recognizing the potential for a fair amount of uncertainty in the observations used for this research, a value of $\gamma = 0.4$ was used to allow for some smoothing of the meteorological fields. Based on this γ, the value of κ was selected so as to provide a filter response of e^{-1} at a distance equivalent to twice the average station spacing (the wavelength of the smallest resolvable wave).

Following the methodology of Koch et al. (1983) the filter response function following two passes D_1^* is

$$D_1^* = D_0\left(1 + D_0^{\gamma-1} + D_0^{\gamma}\right) \tag{6}$$

where D_0 is the spectral response of the first pass as a function of wavelength λ given by

$$D_0 = exp\left[-\kappa\left(\pi/\lambda\right)^2\right]. \tag{7}$$

For a filter response of e^{-1} at the smallest resolvable wavelength, $D_1^* = e^{-1}$ in (1) and solving for D_0 with $\kappa = 0.4$ yields

$$D_0 + D_0^{0.4} + D_0^{1.4} = e^{-1} \tag{8}$$

which may be solved iteratively with result $D_0 = 0.0503$. Equation 7 may then be solved for κ such that

$$\kappa = -\left(\lambda/\pi\right)^2 ln\, D_0 \tag{9}$$

$$\kappa = -\left(2\bar{d}/\pi\right)^2 ln\, 0.0503 \tag{10}$$

where $\bar{d}$ is the average station spacing. Since not all meteorological variables are observed at each GYA station, $\bar{d}$ and κ are dependent upon the variable being interpolated. For example, pressure is routinely observed only at the three surface airway stations resulting in a value of $\bar{d}$ = 366 km, whereas precipitation may be observed at all 178 GYA stations for a given time step, with a consequent average spacing of 17.6 km. Furthermore, due to missing data and data that have been flagged through the quality assurance procedures, the actual number of stations

reporting valid observations for a variable changes with each time step. Consequently, the interpolation weighting factor has been allowed to dynamically vary as a function of both time and the variable being interpolated. This results in proper smoothing of the interpolated field even as the number of stations with valid data changes.

With the exception of downwelling longwave radiation (which will be modeled at each grid point as described in Section 2.4), interpolated fields of each of the meteorological variables used as SHEELS input have been produced using the above-described technique. However, temperature, atmospheric pressure, and solar radiation fields required some special procedures, which will now be discussed.

22.3..1 Temperature and atmospheric pressure

The orographic relief of the GYA is considerable, with elevation differences of over 2500 m across its domain (figure 5). Such large variation in elevation can result in significant modification of near-surface temperature and atmospheric pressure. Thus, measurements of these variables made at a particular observing station may not be indicative of their values at a nearby model grid point if a large gradient in elevation is present.

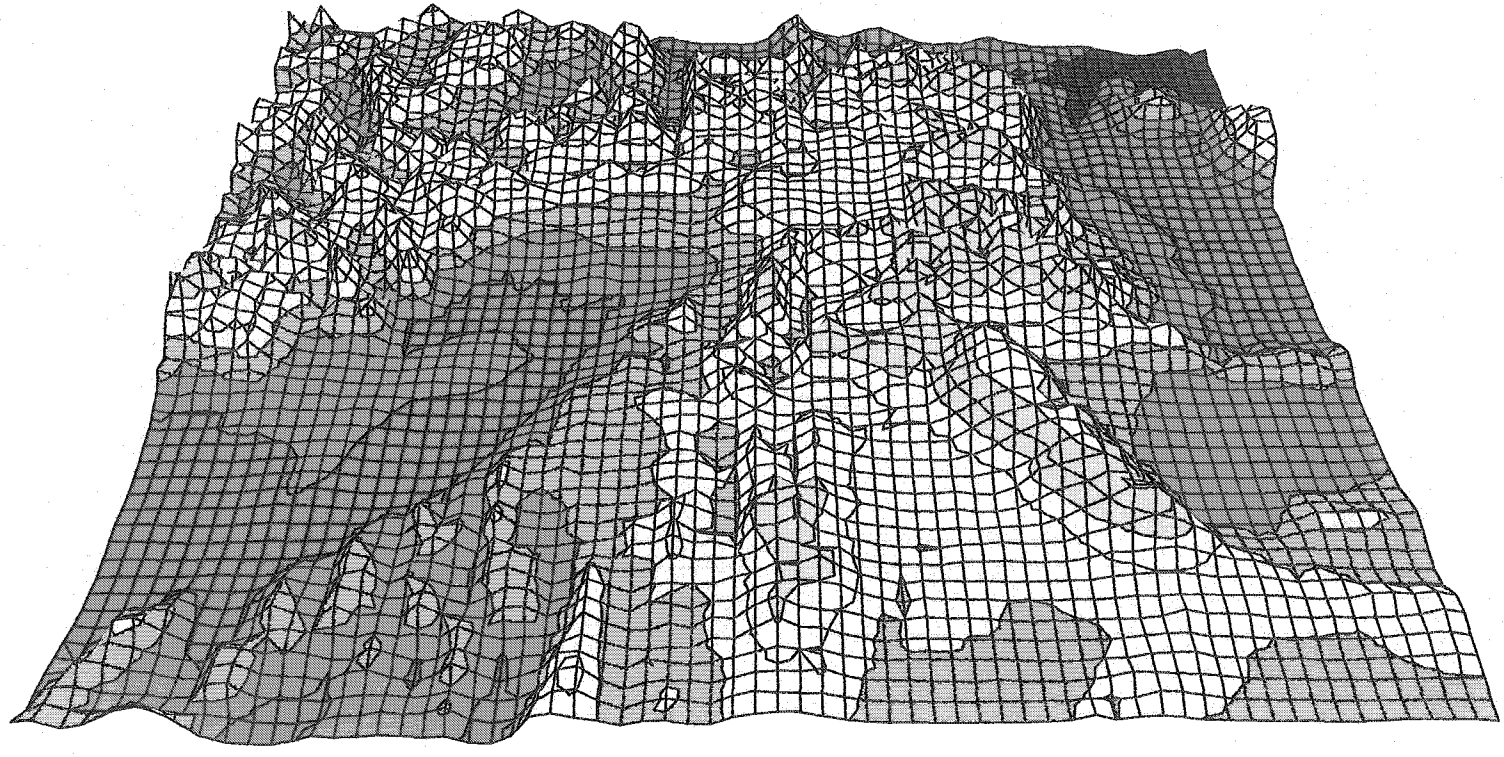


Figure 5: Elevation of the GYA (m).

While complex thermal phenomena such as cold air drainage cannot reasonably be modeled to produce the SHEELS input temperature fields, it is possible to approximate the effects of elevation on temperature in a simpler manner by assuming a constant lapse rate. By regressing near-surface temperature observations against station elevation for GYA stations reporting at least five years worth of quality assured data, a lapse rate of -5.77 K km^{-1} was found (figure 6). Station temperature observations were first standardized to sea level and then interpolated using the Barnes (1973) scheme as described above. The resulting base map of temperature in the GYA was then adjusted to account for each grid point's actual elevation using the same lapse rate, producing a more realistic field of temperature over the complex terrain of the GYA than would otherwise be obtained.

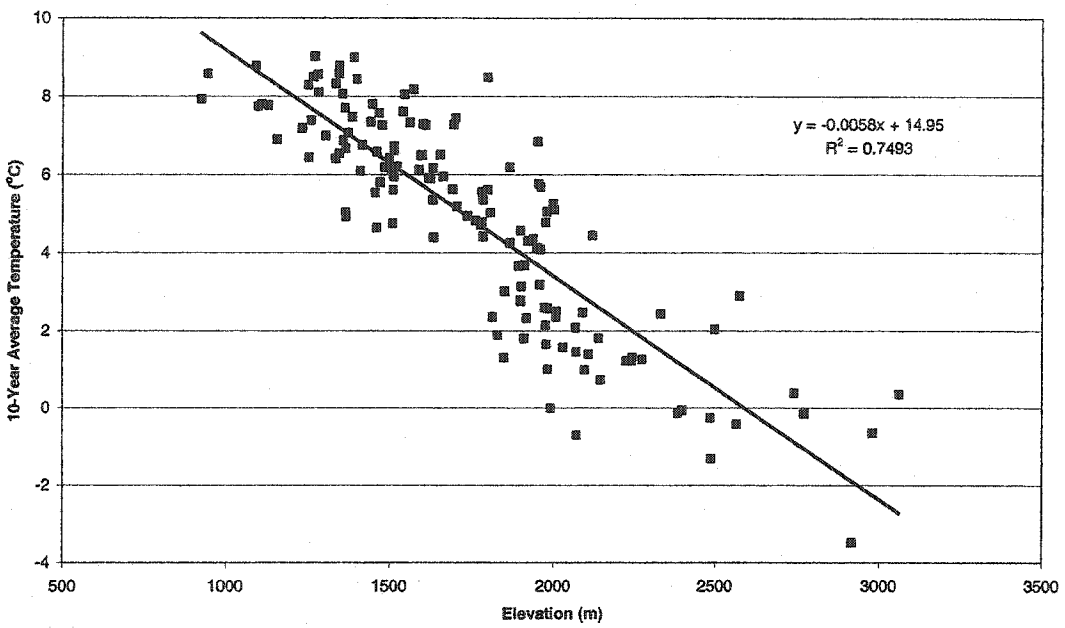


Figure 6: Regression of 10-year average temperature on elevation for GYA stations reporting at least 5 years quality assured data.

As with temperature, pressure observations were first standardized to sea level, interpolated to grid points, and finally adjusted to individual grid point elevations. Pressure p_2 at elevation z_2 is calculated from pressure p_1 at elevation z_1 using the hypsometric equation, neglecting water vapor effects:

$$p_2 = p_1 \exp\left(\frac{-g(z_2 - z_1)}{R\bar{T}}\right) \tag{11}$$

Here, g is the acceleration due to gravity (9.8 m s^{-2}) and R is the dry air gas constant (287 J kg^{-1} K^{-1}). $\bar{T}$ in (11) represents the mean temperature of a fictitious air column extending from z_1 to z_2. This was taken as the average of the temperature at z_1 and

the temperature that would be found at z_2 assuming the COESA (1976) U.S. Standard Atmosphere lapse rate of -6.5 K km^{-1}. Thus,

$$\overline{T} = T(z_1) + 3.25(z_1 - z_2). \tag{12}$$

It should be noted that the use of the U.S. Standard Atmosphere lapse rate is more appropriate in (12) than the previously mentioned lapse rate of -5.77 K km^{-1} since temperature is being estimated for a fictitious column of air rather than for near-surface observations.

22.3..2 Solar radiation

Solar radiation observations in the GYA are only available from four observation sites with varying periods of record – the three surface airway stations (Billings, Montana; Lander, Wyoming; and Pocatello, Idaho) for 1984-1990 and the Agrimet site (Malta, Idaho) for 1985-1993. Due to the dearth of observations, modeling of solar radiation was performed for the time periods lacking data at the surface airway and Agrimet sites, as well as for the entire period of study at the remaining GYA observation sites. This modeling was based on diurnal temperature range using the method of Bristow and Campbell (1984). Here, downwelling solar radiation Q_s is given by:

$$Q_s = \Gamma S_o \cos(\theta_s) \tag{13}$$

where S_o is the solar constant (1370 W m^{-2}) and θ_s is the solar zenith angle. Γ is the atmospheric transmissivity, which is assumed to be accounted for in the magnitude of the diurnal temperature range ΔT relative to the monthly-averaged diurnal range $\overline{\Delta T}$:

$$\Gamma = a\left(1 - exp\left(-b\Delta T^{c}\right)\right) \tag{14}$$

$$b = 0.036\, exp\left(-0.154\overline{\Delta T}\right) \tag{15}$$

Using two measurement sites, Bristow and Campbell (1984) found empirical parameters a and c in (14) to be equal to 0.8 and 2.4, respectively. While Tarboton and Luce (1996) subsequently found these values to be transferable to other sites, optimization of the parameters using data from the four solar radiation observing sites in the GYA was performed. Values of a = 0.65 and c = 2.65 resulted in somewhat lower root mean square differences and substantially reduced bias (table 2).

Table 2: Difference between observed and modeled solar radiation using Malta observations corrected for differences in zenith angle, the Bristow and Campbell (1984) model with their suggested values for parameters a and c, and the Bristow and Campbell model with optimized values for parameters a and c.

Modeling Technique	Malta Observations Corrected for Zenith Angle		Bristow & Campbell a = 0.8, c = 2.4		Bristow & Campbell a = 0.65, c = 2.65	
Station	Mean Difference* (W/m^2)	RMS Difference (W/m^2)	Mean Difference* (W/m^2)	RMS Difference (W/m^2)	Mean Difference* (W/m^2)	RMS Difference (W/m^2)
Billings (1984-1990)	-12.1	154	26.2	100	7.1	85
Lander (1984-1990)	-36.4	169	21.5	103	0.0	94
Pocatello (1984-1990)	-22.3	123	18.7	100	0.1	87
Malta (1985-1993)	-	-	27.9	125	9.4	106

*Modeled - Observed

To evaluate the effectiveness of using the Bristow and Campbell model, solar radiation was simulated at each of the surface airway stations based on observed solar radiation at the Agrimet site. This replicates how SHEELS input solar radiation data might be determined without use of the Bristow and Campbell model for the 1991-1993 period lacking surface airway solar radiation data. The Agrimet observations were corrected for geographically induced differences in zenith angles between the Agrimet site and the surface airway stations such that

$$Q_{SA} = Q_{Ag} \frac{cos\theta_{SA}}{cos\theta_{Ag}}. \tag{16}$$

The subscripts in (16) indicate values for a surface airway station (SA) or the Agrimet site (Ag). As may be seen from table 2, while the root mean square differences remain relatively high even with regionally optimized values of a and c, the Bristow and Campbell (1984) model performs considerably better than using zenith angle-corrected observations from a single station. Consequently, the Bristow and Campbell (1984) method with regionally optimized parameters was used in supplementing the GYA solar radiation observations. Due to the use of diurnal temperature range, solar radiation was left as missing for stations with missing temperature data. Barnes (1973) spatial interpolation was then performed using both the modeled and observed downwelling solar radiation values.

2.4 Modeling of Downwelling Longwave Radiation

Following the creation of gridded fields of the other six SHEELS meteorological inputs, downwelling longwave radiation was modeled at each grid point. Downwelling longwave radiation is an infrequently measured meteorological variable, and no data exist within the GYA for the 1984-1993 period.

Estimates of downwelling longwave radiation were made through use of a physically-based formulation developed by Brutsaert (1975). This formulation utilizes near-surface observations of air temperature and relative humidity to determine clear-sky effective emissivity and atmospheric emittance. These values are then adjusted to account for cloud cover using a method developed by Crawford and Duchon (1999). Fractional cloud cover C_f is determined by the ratio of downwelling solar radiation S_{obs} to the estimated clear-sky value of downwelling solar radiation S_{clear}:

$$C_f = S_{obs} / S_{clear} \tag{17}$$

S_{clear} in (17) is a function of the day of year, time of day, and the shortwave atmospheric transmissivity, which is based on atmospheric pressure and dewpoint using the formulation of Myers and Dale (1983). For nighttime values when S_{obs} is zero, cloud fraction is estimated by linear interpolation of near-sunset values from the previous evening to near-sunrise values the following morning.

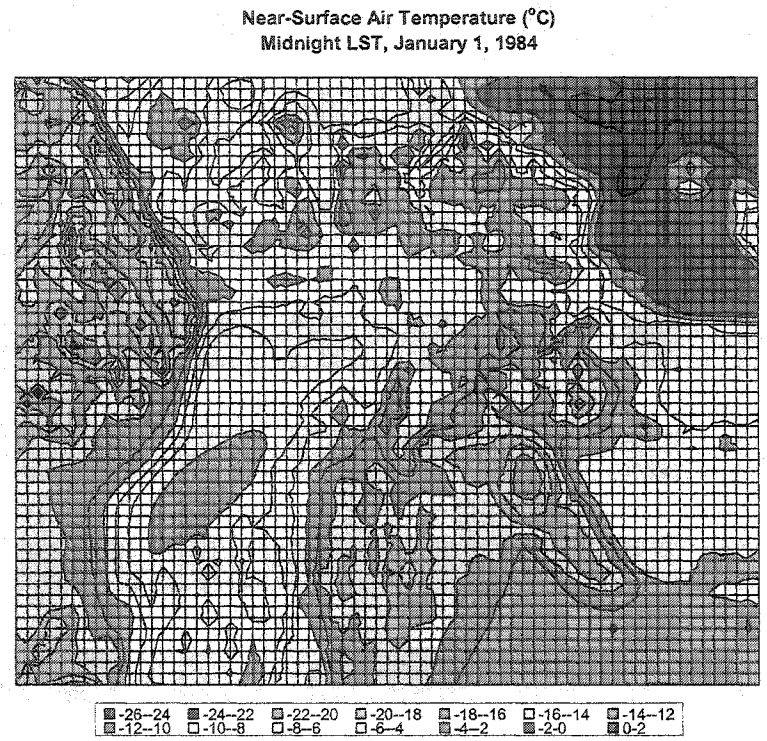
2.5 Example Meteorological Input Fields

Over 600,000 hourly, 8-km resolution input fields were produced for the seven meteorological forcing variables of the SHEELS model, each with data for the 3685 grid points within the GYA domain. Figures 7 and 8 illustrate four such fields as typical examples.

Temperature at midnight local standard time on January 1, 1984 is displayed in figure 7a). Elevation influences on the temperature field are evident in this figure, as can be noted from comparing it to figure 5. The high-elevation peaks of the Wyoming Range to the southeast of the domain center are considerably cooler than their surroundings. Also, warmer temperatures prevail in the Snake River basin extending southwestward from the domain center, and in the low-lying areas near Billings, Montana, in the northeast corner of the GYA. While indications of the Wyoming Range remain in the temperature field for noon local standard time on July 1, 1984 (figure 7b), elevation effects are generally not as prominent. Noticeable in both 7a and 7b is the lack of detail in the southeastern corner of the domain, resulting from relatively sparse observations in that area.

Figure 8a shows downwelling solar radiation for noon local standard time on the summer solstice of 1984. The low zenith angle of the sun for this particular time step results in solar radiation flux approaching 1000 Wm^{-2} in the southeastern portion of the GYA. Towards the northwest, however, solar radiation is considerably reduced,

(a)



(b)

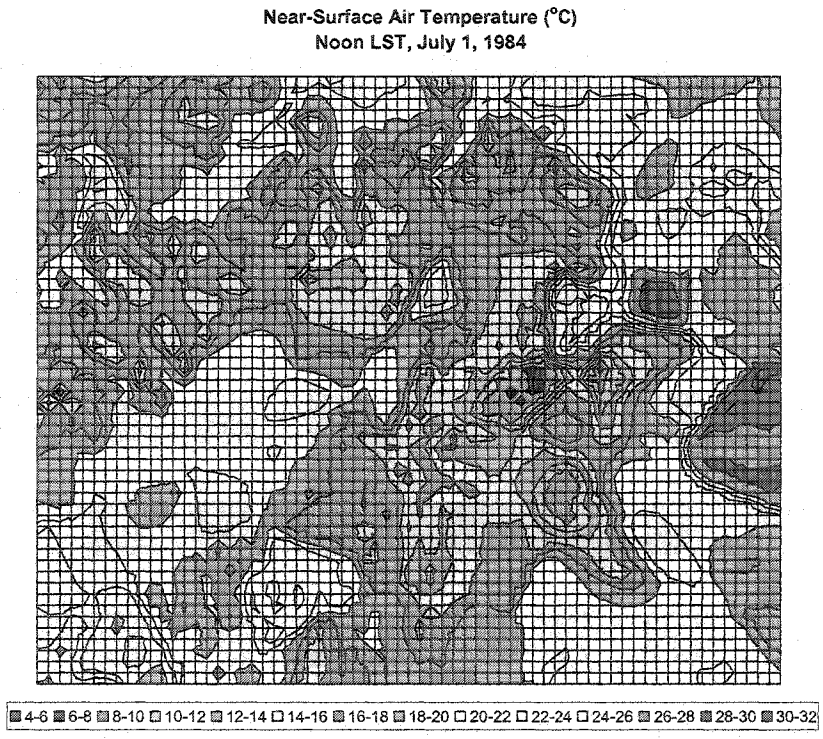
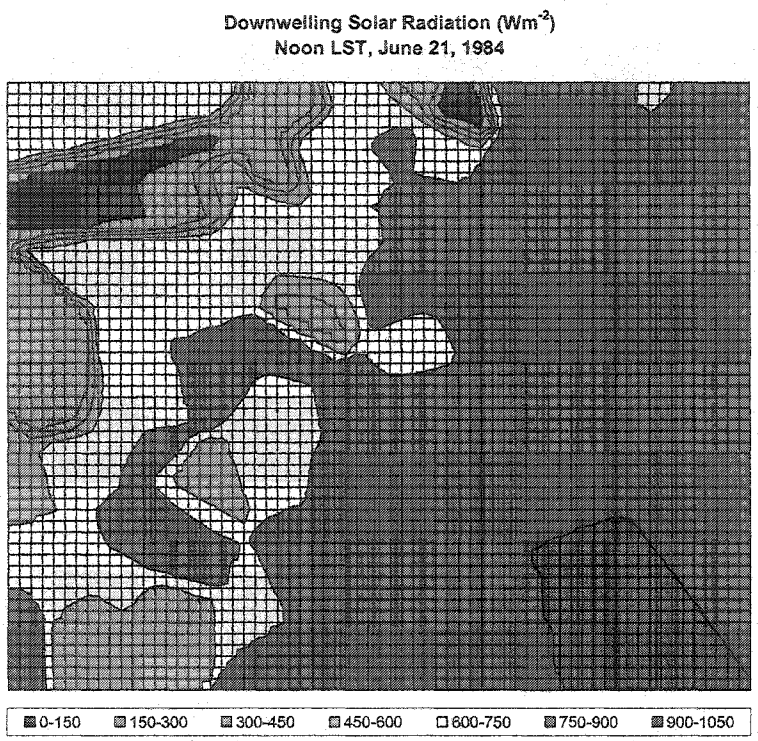


Figure 7: Gridded 8-km resolution input temperature field for (a) midnight local standard time, January 1, 1984 and (b) noon local standard time, July 1, 1984.

(a)



(b)

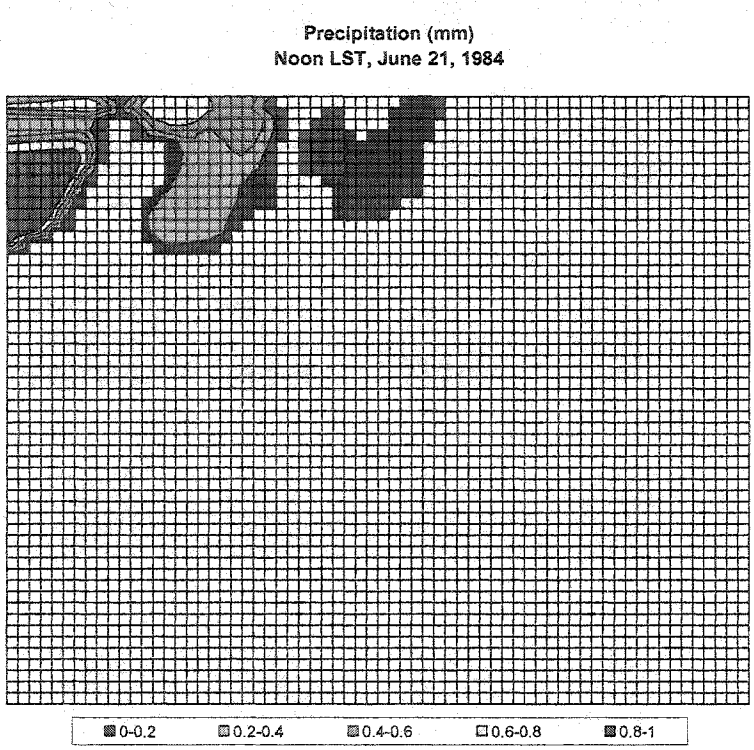


Figure 8: Gridded 8-km resolution input (a) downwelling solar radiation and (b) precipitation for noon local standard time, June 21, 1984.

presumably as a result of cloudiness. This hypothesis is corroborated by precipitation occurring at the time in that area (figure 8b). It should be noted that although downwelling solar radiation values are in part modeled based on diurnal temperature range, precipitation data are not used in the modeling, such that these are independently derived fields.

Clearly, the fields discussed here represent a tiny fraction of the complete meteorological datasets that have been produced. These quality-assured, gridded datasets are capable of providing not only meteorological input for the SHEELS model, but also input for other numerical simulations of similar spatial resolution. Such applications need not be limited to land-atmosphere processes, but could also include use of the data for running hydrological, ecological, or climatological models.

3 The SHEELS Model

The Simulator for Hydrology and Energy Exchange at the Land Surface (SHEELS) is a numerical model derived from the Biosphere-Atmosphere Transfer Scheme (BATS) of Dickinson et al. (1993). Smith et al. (1993) provide the original description of the "Ex-BATS" model that became SHEELS, and their work remains the definitive reference for many aspects of the model. Where substantial changes have not been made, this chapter will summarize SHEELS, with the reader referred to Smith et al. (1993) for details. Several improvements and additions have been implemented within SHEELS since the Smith et al. (1993) paper, however, and these will be explicitly described. Figure 2 provides a schematic diagram of the SHEELS model.

As it is used in this study, SHEELS uses directly measured meteorological inputs. However, the model also can be coupled to a GCM. Nominal model temporal resolution is one hour, resulting in 87,672 time steps over the 10-year period of study. Horizontal resolution is user-selectable and has been set to 8 km, as this represents the resolution of the coarsest input dataset, the fractional vegetation cover derived from 8-km global area coverage Normalized Difference Vegetation Index (described in section 3.1.2). Use of a relatively coarse 8-km resolution also reduces computational costs in terms of model run time and size of input and output files. When fully optimized and run on an IBM Regatta p690 supercomputer, a 10-year

simulation over the 3685 grid points of the GYA requires approximately 200 hours of computational time and produces roughly 6 GB of output data.

3.1 Vegetation

The SHEELS model includes a one-layer treatment of vegetation and allows for partial coverage of grid cells. Total vegetation biomass, in the form of fractional vegetation cover and leaf area index (LAI), is then used to model transpiration and within-canopy turbulent fluxes, as well as account for surface albedo differences arising from the presence of vegetation. Most vegetation parameters within SHEELS are temporally constant functions of prescribed land cover type, as will be discussed in section 3.1.1. Grid cell fractional vegetation cover, however, varies in time using methods described in section 3.1.2.

3.1.1 Land cover type-dependent vegetation parameters

The University of Maryland Global Land Cover Facility (GLCF) has produced a 1-km resolution global land cover type database through automated classification of Advanced Very High Resolution Radiometer (AVHRR) data from 1981-1994 (Hansen et al., 2000). Utilizing both the optical and thermal infrared bands of the AVHRR instrument, classification of images resulted in discrimination of 14 land cover types: water, evergreen needleleaf forest, evergreen broadleaf forest, deciduous needleleaf forest, deciduous broadleaf forest, mixed forest, woodland, wooded

grassland, closed shrubland, open shrubland, grassland, cropland, bare ground, and urban.

For SHEELS model input, cartographically unprojected 1-km GLCF data were resampled to match the 8-km square grids used in the GYA. Resampling was accomplished through selection of the land cover type occurring with greatest frequency in each 8-km grid cell. In the case of two or more land cover types occurring with equal frequency within a grid cell, the land cover type occurring nearest the center of the 8-km cell was selected.

Vegetation parameters in SHEELS that vary with land cover type include LAI, canopy height, canopy albedos in the visible and near-infrared wavelengths, maximum leaf dimension, and minimum stomatal resistance. In addition to the vegetation parameters, soil surface emissivity is also prescribed based on land cover type. Values of these parameters used for this study are summarized in table 3.

Table 3: Land cover type-dependent properties.

Land Cover Type	LAI[*]	Canopy Height (m)[+]	Maximum Leaf Dimension (m)[+]	Minimum Stomatal Resistance (s m^{-1})[*]	Surface Emissivity[@]	Minimum Canopy Visible Albedo[+]	Minimum Canopy Near-Infrared Albedo[+]	Manning's Coefficient (s $m^{-1/3}$)[%]
Water	NA	NA	NA	NA	0.95	NA	NA	0.010
Evergreen Needleleaf Forest	5.5	17.0	0.06	200	0.98	0.05	0.23	0.080
Evergreen Broadleaf Forest	5.5	35.0	0.10	150	0.98	0.04	0.20	0.080
Deciduous Needleleaf Forest	3.5	17.0	0.06	200	0.98	0.05	0.23	0.080
Deciduous Broadleaf Forest	3.5	20.0	0.15	200	0.98	0.08	0.28	0.080
Mixed Forest	4.5	20.0	0.10	200	0.98	0.06	0.24	0.080
Woodland	4.5	17.0	0.10	200	0.98	0.06	0.24	0.080
Wooded Grassland	3.5	1.0	0.30	200	0.95	0.08	0.27	0.055
Closed Shrubland	5.5	0.5	0.03	200	0.95	0.06	0.25	0.070
Open Shrubland	3.5	0.5	0.03	200	0.95	0.08	0.28	0.035
Grassland	2.5	1.0	0.30	200	0.92	0.09	0.29	0.030
Cropland	3.5	1.0	0.30	120	0.95	0.10	0.30	0.030
Bare Ground	0.0	NA	NA	NA	0.94	NA	NA	0.020
Urban	0.5	0.5	0.10	200	0.95	0.10	0.30	0.014

Values based on: [*] - Dickinson et al., 1993; [+] - Sellers et al., 1996; [@] - Oke, 1987; [%] - Bedient and Huber, 2002

3.1.2 Fractional vegetation cover

Hale and Duchon (2003) have shown that inclusion of a temporally-varying component of vegetation amount in the SHEELS model significantly improves estimated surface temperature. They further theorize that such improvements should result in more accurate simulation of turbulent and ground heat fluxes, as these are functions of surface temperature. To this end, satellite-derived estimates of fractional vegetation cover have been utilized within SHEELS. In addition to allowing for seasonal changes in vegetation amount, inclusion of such estimates is particularly important in this study to capture the fire-induced vegetation changes that occurred within the GYA.

As part of the National Aeronautics and Space Administration (NASA)/National Oceanic and Atmospheric Administration (NOAA) Pathfinder AVHRR Land (PAL) dataset, surface reflectance values for channels 1 (0.58 to 0.68 μm) and 2 (0.725 to 1.10 μm) have been calibrated, corrected for atmospheric attenuation, rectified, and resampled to an 8 km by 8 km grid (Agbu and James, 1994). Differences between AVHRR instruments flown on the three NOAA polar orbiting satellites used in the period of record have been also taken into account.

In addition to daily data, PAL contains 10-day maximum value composites of reflectance for channels 1 and 2. These composites retain data from the satellite

overpass that produces the maximum Normalized Difference Vegetation Index (NDVI) value in a 10-day period. This acts to reduce the potential for cloud contamination since the high visible albedo of clouds decreases NDVI.

The 10-day maximum value composite data were obtained for the area roughly corresponding to 42° to 46° N and 108° to 114° W. ESRI ArcInfo was used to extract data within the burn area perimeter (figure 1), as determined by the Yellowstone National Park Spatial Analysis Center (2003). The burn area includes regions affected by either canopy fires or ground fires of varying burn intensity.

Channel 1 surface reflectances (ρ_{RED}) and channel 2 surface reflectances (ρ_{NIR}) were used to produce three vegetation indices: the Normalized Difference Vegetation Index (NDVI), the Soil-Adjusted Vegetation Index (SAVI), and the Modified Soil-Adjusted Vegetation Index 2 (MSAVI2). Developed by Tucker (1979), NDVI uses the difference between reflectances in these two channels, normalized by their sum:

$$NDVI = \frac{\rho_{NIR} - \rho_{RED}}{\rho_{NIR} + \rho_{RED}}. \qquad (18)$$

While NDVI has a long history of use in vegetation biomass estimation and land use/land cover change research, it has been shown to be somewhat sensitive to soil brightness in addition to vegetation amount (Leprieur et al., 1994). As a result, noise can be introduced into the vegetation index as a result of variations in soil composition or soil moisture.

Huete (1988) developed SAVI in an effort to reduce the sensitivity of NDVI to soil brightness:

$$\mathrm{SAVI} = \frac{\rho_{\mathrm{NIR}} - \rho_{\mathrm{RED}}}{\rho_{\mathrm{NIR}} + \rho_{\mathrm{RED}} + \mathrm{L}}(1 + \mathrm{L}). \tag{19}$$

Here, L represents a soil adjustment factor that varies from 0 for high density vegetation to 1 for bare soil. Since the vegetation density is usually unknown, and in fact is often the variable to be retrieved, a somewhat arbitrary value of L = 0.5 is frequently employed.

Qi et al. (1994) derived an empirical function for L based on the NDVI and the Weighted Difference Vegetation Index (WDVI):

$$\mathrm{L} = 1 - 2.12 \times \mathrm{NDVI} \times \mathrm{WDVI}. \tag{20}$$

They then solved (19) to arrive at the MSAVI2:

$$\mathrm{MSAVI2} = \frac{2\rho_{\mathrm{NIR}} + 1 - \sqrt{(2\rho_{\mathrm{NIR}} + 1)^2 - 8(\rho_{\mathrm{NIR}} - \rho_{\mathrm{RED}})}}{2}. \tag{21}$$

The soil adjustment factor in MSAVI2 is thus a dynamic function of the channel 1 and channel 2 reflectances, rather than an arbitrary constant value as in SAVI.

To determine which of these indices best captured the fire-induced vegetation changes (i.e. demonstrated the largest difference between pre-fire and post-fire values), time series of spatial averages over the burn area were made for each index. These were then compared to a time series of NDVI data that have been spatially averaged for the entire GYA. As can be seen from figure 9, NDVI over the entire GYA region increased slightly after the fires as compared to before the fires. Also of interest is the annual cycle in the spatial standard deviation resulting from low values in the winter when snow cover is considerable and much vegetation is dormant throughout the region, to high values in the summer when variations in land cover (e.g. forest versus urban areas) dominate.

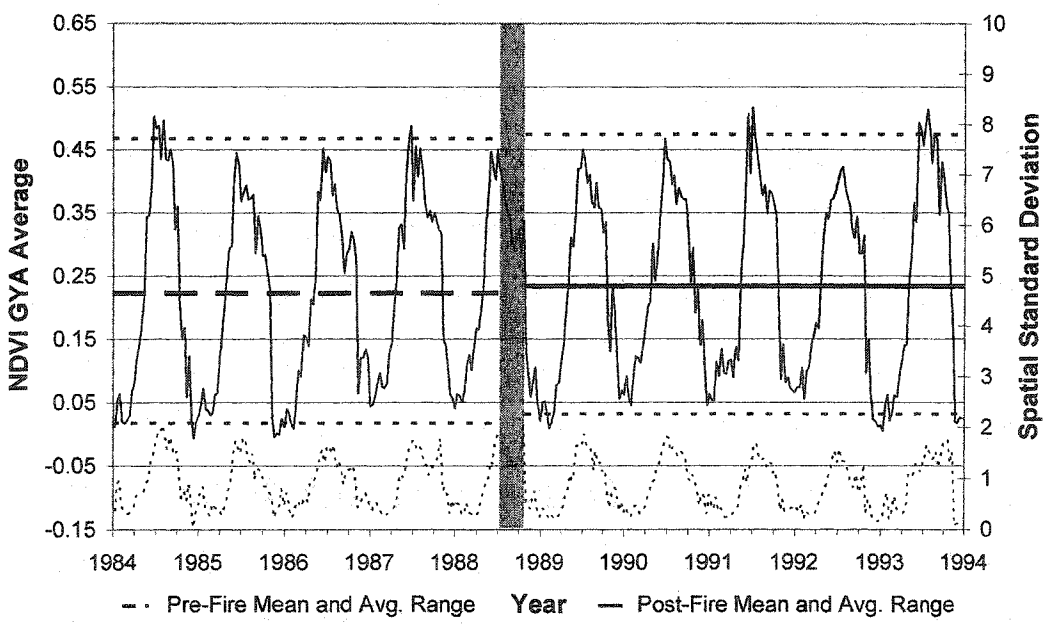


Figure 9: Time series of NDVI spatially averaged over the entire GYA model domain and its associated spatial standard deviation. The time period of the fires is shaded.

In contrast to figure 9, NDVI over the burn regions shows a marked decrease in post-fire versus pre-fire average and annual maximum and minimum values (figure 10). This is also true for SAVI (figure 11) and MSAVI2 (figure 12). Spatial standard deviations for all three indices remain low throughout the time period, indicating relatively uniform vegetation amounts within the burn area. A peak in the spatial standard deviation of NDVI occurs during the time period of the fires, however it is impossible to determine whether this occurs primarily as a result of differences in vegetation amount, or is an artifact of smoke contamination of the satellite image.

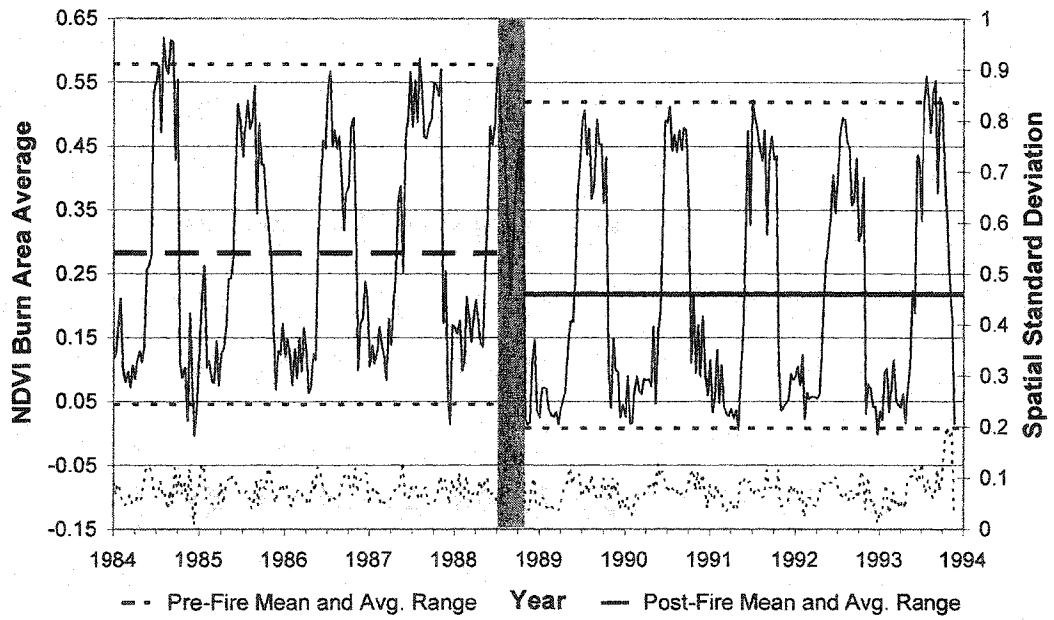


Figure 10: Time series of NDVI spatially averaged over the burn area and its associated spatial standard deviation. The time period of the fires is shaded.

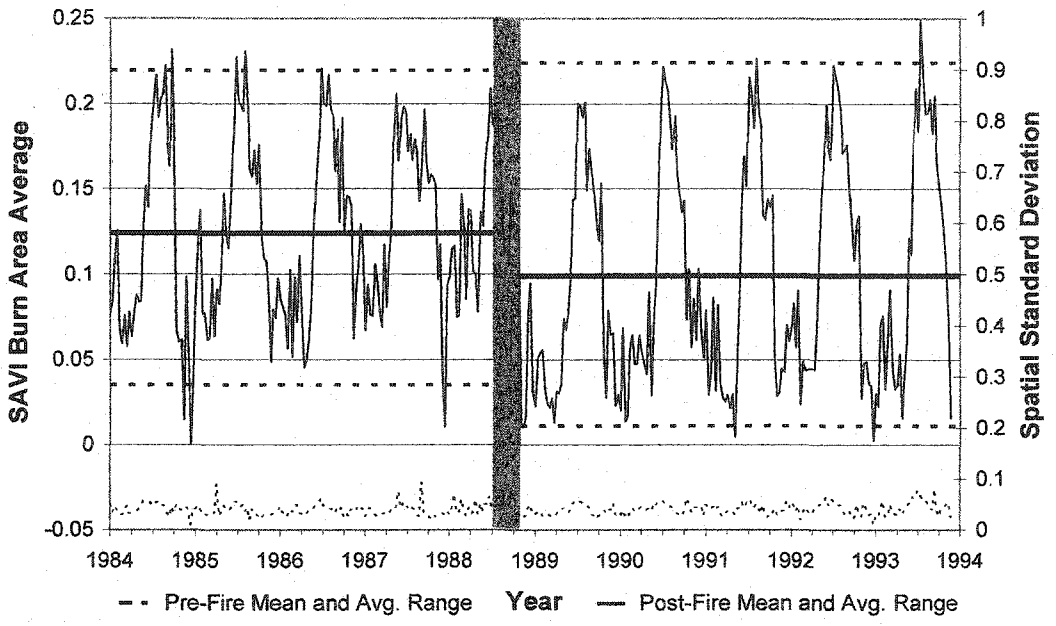


Figure 11: Time series of SAVI spatially averaged over the burn area and its associated spatial standard deviation. The time period of the fires is shaded.

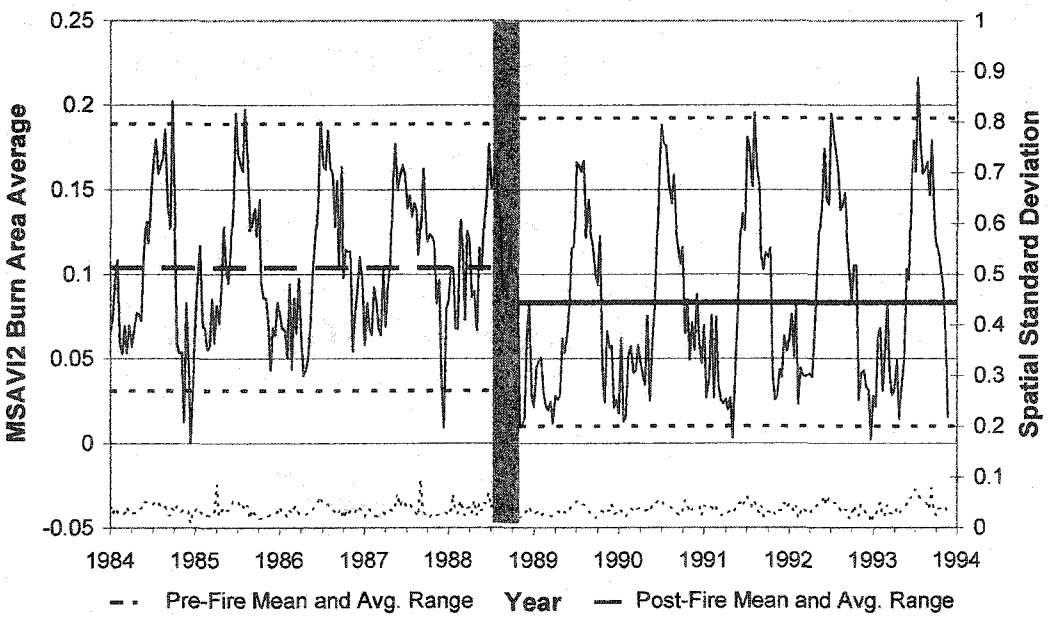


Figure 12: Time series of MSAVI2 spatially averaged over the burn area and its associated spatial standard deviation. The time period of the fires is shaded.

As has been previously reported (e.g. Leprieur et al., 1994), NDVI has a larger dynamic range than the other two vegetation indices. However, the pre-fire versus post-fire change in the spatially and temporally averaged indices as a percentage of their observed 10-year ranges is nearly the same for NDVI and SAVI, and only slightly less for MSAVI2 (table 4). Also, the temporally averaged spatial standard deviation as a percent of range is lower for NDVI than the other two indices. Based on this and the ubiquity of NDVI in land cover change research, NDVI was selected for parameterization of vegetation amount in the SHEELS model.

Table 4: Vegetation index statistics.

Area/Index	GYA NDVI	Burn Area NDVI	Burn Area SAVI	Burn Area MSAVI2
Pre-Fire Average (1984-1987)	0.222	0.283	0.124	0.104
Post-Fire Average (1989-1993)	0.233	0.218	0.099	0.083
10-Year Range of Index	0.523	0.623	0.249	0.217
Change as % of Range	2.11	-10.43	-10.09	-9.51
10-Year Avg. of Spatial Standard Deviation	0.891	0.076	0.040	0.036
Avg. Standard Deviation as % of Range	170.39	12.15	16.20	16.80

Fractional vegetation cover σ_f is then varied within SHEELS as a function of NDVI based on the formulation developed by Gillies et al. (1997)

$$\sigma_f \approx \left(\frac{NDVI - NDVI_o}{NDVI_s - NDVI_o} \right)^2 \quad (22)$$

where $NDVI_o$ and $NDVI_s$ are NDVI values for bare soil and fully vegetated areas, respectively. Values of -0.040 and 0.764 were used for $NDVI_o$ and $NDVI_s$, respectively. These were derived by averaging the highest or lowest observed single-pixel NDVI value from each of the 10 years of the study period. Maximum single-pixel values ranged from 0.640 to 0.992 with a standard deviation of 0.119. Minimum single-pixel values ranged from -0.064 to -0.024 with a standard deviation of 0.013.

3.2 The Soil Column

3.2.1 Soil zones and soil layers

While SHEELS is similar to BATS in many respects, significant differences exist, especially in subsurface parameterizations. Unlike BATS in which the soil column consists of three nested zones, the soil column in SHEELS is divided into three discrete zones: upper, root, and lower. The upper zone acts as an interface between the remaining soil column and the overlying atmosphere. At the soil column's upper surface, both turbulent and radiative fluxes occur, as well as the addition or removal of moisture via infiltration or evaporation. It is thus necessary that the upper zone be

relatively thin so as to best approximate the large temperature and soil moisture gradients that may exist within it. Past studies involving the SHEELS model (e.g. Martinez et al., 2001; Hale and Duchon, 2003) have employed a 0.05 m thick upper zone, and this thickness has been utilized here as well.

The root zone is the portion of the soil column containing the major proportion of root biomass and is a source of water for transpiration. As different floral species have different rooting depths, the thickness of the root zone is dependent upon the type of vegetation present. However, to minimize computational costs, the SHEELS model assumes invariant thickness of each soil zone across the model domain. Examining a study site in Wyoming near the GYA, Pearson (1982) found that over 90% of the root biomass of lodgepole pines occurs in the top 0.40 m of soil. Since lodgepole pine comprise 77% of forests in Yellowstone National Park and are the dominant tree species in the GYA (Schullery, 1989), a domain-wide root zone thickness of 0.40 m has been used.

Heat transfer and percolation of water extend into the lower zone in SHEELS, which may have either a permeable or impermeable lower boundary. Using U.S. Department of Agriculture (USDA) Natural Resource Conservation Service (NRCS) data (described below), the average depth to bedrock in the GYA has been calculated and used as the impermeable lower boundary of the soil column. The resulting total soil column depth is 1.10 m, divided into an upper zone of 0.05 m thickness, a root zone of 0.40 m thickness, and a lower zone of 0.65 m thickness.

Each of the three soil zones are further subdivided into layers. Input soil parameters are specified for each zone, but do not vary between layers within a zone. Infiltration and percolation are then separately determined for each soil layer using an algorithm developed by Capehart and Carlson (1994). Modeling water movement between layers in this manner results in the potential for different layers within a zone to have different fractional water content. Thus, by allowing zones to be divided into layers, a non-linear vertical gradation in soil water content within a zone is possible, which results in better estimates of water and heat fluxes at the surface.

The number of layers into which each soil zone is divided is arbitrary. The large gradients of heat and moisture in the upper zone necessitate relatively thin layers, and thus were divided into five 0.01 m layers. Martinez et al. (2001) examined the optimal number of layers into which a 2.5 m deep soil column should be divided to minimize computational expense with negligible effect on accuracy. They found that a 1.25 m thick root zone should be divided into a minimum of nine layers. Based on this, the 0.40 m thick root zone in this study was divided into 3 layers, each 0.133 m thick. The relatively inactive lower zone will remain undivided, as recommended by Martinez et al. (2001).

3.2.2 Soil property parameters

The State Soil Geographic (STATSGO) database includes nation-wide soil data compiled by the NRCS (USDA-NRCS, 1994) in the form of ArcInfo 7.0 coverages. These data are based on detailed Soil Survey Geographic transects and samples that have been aggregated to a 1:250,000 scale quadrangle. In the STATSGO database, digital vector polygons (map units) delineate areas of similar soil type, relief, and drainage, with a minimum polygon size of about 6.25 km^2 (Davis, 2001). Each map unit is comprised of up to 21 component soils. While STATSGO includes the percent composition of each component within the map unit, individual components are not mapped and thus cannot be geographically located. Additionally, components comprise one or more vertical layers (see figure 13).

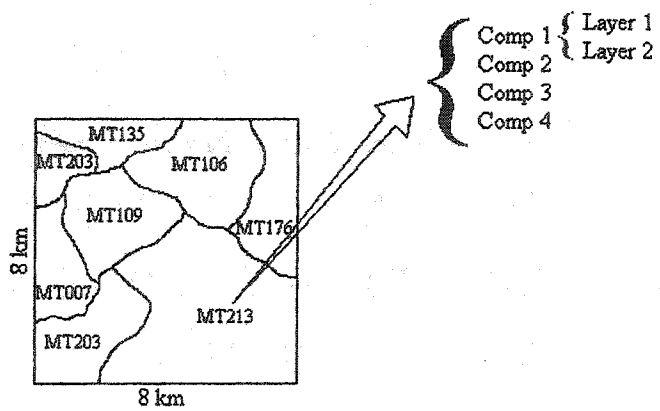


Figure 13: Schematic diagram of STATSGO map units, components, and layers.

Component soil layers are connected to attributes in the Soil Interpretations Record database, which contains numerous physical, chemical, and hydrologic properties. Soil bulk density, fractional clay component, and particle size information from this database were used to calculate necessary soil parameters for each component occurring within the GYA. Soil texture class is based on NRCS standards (Soil Survey Staff, 1998), while effective porosity, wetting front suction head, and saturated hydraulic conductivity are determined from the Brooks and Corey (1964) soil water retention curves using empirical parameterizations developed by Rawls (1983) and Rawls and Brakensiek (1985). Saturated soil suction and a parameter used for calculating soil diffusivity (Clapp and Hornberger, 1978) are then derived from wetting front suction head and the soil texture. Finally, bulk density ρ_b is used to find total porosity ϕ_{tot} and wilting point WP by

$$\phi_{tot} = 1 - \frac{\rho_b}{2650 \text{ kg m}^{-3}} \tag{23}$$

$$WP = \frac{\phi_{tot} - \phi_{eff}}{\phi_{tot}} \tag{24}$$

where ϕ_{eff} is the effective porosity and 2650 kg m^{-3} is the assumed density of the mineral portion of the soil.

Map unit coverages for each county within the GYA were geospatially intersected with the model domain grid cells using ESRI ArcView. The resulting percentage composition of map units within grid cells was used in conjunction with the

percentage composition of soil components and their layers within each map unit to determine areal weighting of component properties to arrive at grid cell-mean values. That is, grid cell-averaged soil properties were derived from component properties weighted by their spatial extent in both the horizontal and vertical dimensions. It should be noted that while hydrophobicity can occur as a result of high intensity ground fires (DeBano, 1981), Shovic (1988) reported no substantial increase in soil hydrophobicity within Yellowstone National Park following the 1988 fires. Consequently, fire-induced hydrophobicity is neglected in this study and post-fire soil parameters are equivalent to those used for the pre-fire period.

There are instances in which a grid cell contains both land and water components at the resolution of the NRCS map unit coverages. In such cases, the GYA land cover classification (section 3.1.1) took precedence, such that any water components of grid cells classified as land were excluded in averaging and any soil components of grid cells classified as water were ignored.

The Soil Interpretations Record database also includes values for the observed range of depth to bedrock for each soil component in a map unit. Depth to bedrock for each map unit was computed as an average of that of each of its soil components' depth to bedrock, weighted by the component percentage composition of the map unit. Areally-weighted averaging of the resultant map unit depth to bedrock values yielded a GYA-wide average depth to bedrock of 1.088 m. This was then used to define the

total soil column thickness and lower impermeable boundary in the SHEELS model as 1.10 m.

3.3 Snow Parameterizations

Past studies involving SHEELS have modeled surface fluxes over Oklahoma (Hale and Duchon, 2003; Martinez et al., 2001), central Kansas (Crosson et al., 1993; Smith et al., 1993), and the Tarrawarra catchment in Australia (Martinez, 1999). Snow and ice accumulation over these areas were minimal for the time periods studied, and thus there was no need to accommodate frozen water within SHEELS. Snowfall in the GYA, however, is substantial, and in fact constitutes the majority of the annual precipitation (Dirks and Martner, 1982). For this reason, the SHEELS model has been modified to account for the effects of snow cover. Such effects include storage of water at the surface in the winter and spring months prior to infiltration or runoff, increase in surface albedo, and thermal insulation of the underlying soil column. This section addresses partitioning of precipitation into rain or snowfall, the model snow layers, and densification and albedo changes associated with the aging of snow. Thermal and radiative balances of the snow layers and the partitioning of snow ablation into losses through sublimation, evaporation of meltwater, and infiltration of meltwater to the soil surface are discussed in section 3.5.

3.3.1 Partitioning of precipitation into model snow layers

Precipitation type (rain versus snow) is prescribed in SHEELS as a function of near-surface air temperature based on data from the U.S. Army Corps of Engineers (1956). Here, precipitation type is assumed to be entirely liquid at temperatures greater than 3.0 °C and entirely frozen at temperatures below -0.5 °C. Between these two temperatures, the precipitation is separated into liquid and frozen fractions in a linear fashion.

Once input liquid water precipitation has been partitioned into rainfall and snowfall, new snowfall accumulates in the topmost of a maximum of four model snow layers. Depth of newly fallen snow is determined through parameterization of snow density based on near-surface air temperature. Anderson and Crawford (1964) found that new snow density $\rho_{newsnow}$ in kg/m^3 may be described as

$$\begin{aligned} \rho_{newsnow} &= 50 + 1000\left(T_{air}/100\right)^2 \qquad T_{air} > 0\,^{\circ}\mathrm{F} \\ \rho_{newsnow} &= 50 \qquad\qquad\qquad\qquad\quad T_{air} < 0\,^{\circ}\mathrm{F} \end{aligned} \tag{25}$$

where T_{air} is the near-surface air temperature in °F. While there is considerable variation in observed new snow densities from values derived from this formulation, this provides more realistic values than the often used new snow density of 100 kg/m^3.

Maximum thickness of each of the top three model snow layers is 50, 100, and 200 mm, while the bottom snow layer depth is unbounded. Once a layer reaches its maximum thickness, additional snow results in a shift of snow from that layer to the next lower layer. In such instances, the thermal characteristics of the shifted snow amount are averaged with those of the next lower layer, weighted by their respective snow water equivalents. For example, consider a case in which the top layer has a depth of 50 mm, snow water equivalent of 10 mm, and temperature of 270 K, and the second layer has a depth of 60 mm, snow water equivalent of 21 mm, and temperature of 266 K. If new snowfall occurs with depth of 15 mm, then 15 mm of the original top layer will be shifted into the second snow layer since the top layer is already at its maximum thickness. The second snow layer would consequently have a depth of 75 mm (60 mm + 15 mm), snow water equivalent of 24 mm (21 mm + 15 mm/50 mm * 10 mm), and temperature of 266.5 K (266 K * 21 mm/24 mm + 270 K * 3 mm/24 mm). In a similar fashion, the temperature of the new top layer is an average of the original top layer temperature and the temperature of the new snowfall (taken as equivalent to the near-surface air temperature), weighted by the original top layer snow water equivalent (10 mm) and the liquid water equivalent of the new snowfall.

A complication in the implementation of snow parameterizations in the SHEELS model is the potential for canopy interception of snow. Over the course of a season, a considerable portion of the total snowpack may initially be intercepted by the canopy (Storck and Lettenmaier, 1999). A primary consequence of this interception is an

increase in canopy albedo and corresponding decrease in heating via absorption of solar radiation. Explicit modeling of this interception would substantially increase the computational complexity of SHEELS since it would necessitate introduction of not only a canopy snow layer, but also snow layers below the canopy that would differ from the snow layers modeled in the unvegetated portion of a grid cell.

In order to capture the canopy albedo changes resulting from intercepted snow while keeping the model computationally manageable, new snow is added to the canopy to a maximum thickness of 50 mm. Canopy albedo is determined then as a linear function of the amount of snow in the canopy, with albedo values ranging from the input vegetation albedo in the case of no canopy snow to the age-adjusted snow albedo in the case of a completely filled (50 mm thick) canopy snow layer.

Snow ablation within the canopy occurs at a rate identical to that in the top ground snow layer. Since the water input of new snow has already been accounted for in the ground snow layers, the movement of water from the canopy snow layer through latent heat flux or drip of melt water is not tracked, thereby maintaining the model water balance. The net effect of these parameterizations is a computationally simpler algorithm in which snow within and outside of the vegetated regions of a grid cell are treated identically in terms of both heat transfer and hydrology, however the canopy albedo effects of intercepted snow are maintained.

3.3.2 Age-dependent snow density and albedo

After entering the snowpack, snow density increases with age and total snowpack depth due to compaction by overlying layers (Bras, 1990). Snow thermal conductivity, critical to accurate modeling of snow surface temperature and the flux of heat into the snowpack, is a function of snow density, necessitating that density changes be taken into account. The method used in SHEELS closely follows that of the SNTHERM model developed by Jordan (1991). Specifically, snow viscosity ν is modeled as a function of density ρ_{snow} and snow surface temperature T_{sfc} from the previous time step:

$$\upsilon = \upsilon_o \, exp\left(-c_1 T_{sfc} + c_2 \rho_{snow}\right) \tag{26}$$

Here, ν_o is the viscosity of snow at 0 °C extrapolated to zero density (3.6 x 10^6 N s m^{-2}) and c_1 and c_2 are constants with value 0.08 $°C^{-1}$ and 0.021 m^3 kg^{-1}, respectively. Snow density may then be incremented from its previous value as

$$\rho_{snow}^{t} = \rho_{snow}^{t-1}\left(1 - \frac{g\rho_{wat}SWE}{2\upsilon}\Delta t\right) \tag{27}$$

where g is the acceleration due to gravity (9.81 m s^{-2}), ρ_{wat} is the density of liquid water (1000 kg m^{-3}), SWE is the snowpack-total snow water equivalent, and Δt is the model time step in seconds. Density within each layer is limited to a maximum value of 525 kg/m^3. Finally, snowpack depth in each snow layer is adjusted such that

$$D_i = W_i \rho_{wat} / \rho_{snow} \tag{28}$$

where D_i and W_i are the depth and snow water equivalent of the i-th snow layer.

In addition to snow density increasing with age, the albedo of snow changes over time due to increasing grain size and accumulation of contaminants (Langham, 1981). Snow albedo also varies considerably with solar zenith angle θ_s. In the BATS model, Dickinson et al. (1993) employ an empirical algorithm to adjust snow albedo based on age and zenith angle, and this same method will be utilized here. Visible (wavelength ≤ 0.7 μm) albedo α_V and near-infrared (wavelength > 0.7 μm) albedo α_{IR} are treated separately:

$$\alpha_V = 0.95 - 0.19F_{age} + f(\theta_s)(0.02 + 0.076F_{age}) \tag{29}$$

$$\alpha_{IR} = 0.65 - 0.325F_{age} + f(\theta_s)(0.14 + 0.13F_{age}). \tag{30}$$

In (29) and (30), the first term represents the albedo of new snow with low zenith angle (0.95 for visible wavelengths), the second term accounts for the decrease in albedo with snow age (described below), and the third term adjusts the albedo for increases that occur at high solar zenith angles ($\theta_s > 60°$):

$$\begin{aligned} f(\theta_s) &= \frac{1 - 2cos(\theta_s)}{1 + 4cos(\theta_s)} \qquad \theta_s > 60° \\ f(\theta_s) &= 0 \qquad \theta_s \leq 60° \end{aligned} \tag{31}$$

The snow age factor F_{age} in (29) and(30) is given by

$$F_{age} = \tau / (1+\tau) \tag{32}$$

where τ is a nondimensional snow age incremented at each time step N by:

$$\begin{aligned} \tau^{N+1} &= (\tau^N + \Delta\tau)(1 - 100\Delta D) && \Delta D \le 0.01\ \text{m} \\ \tau^{N+1} &= 0 && \Delta D > 0.01\ \text{m} \end{aligned} \tag{33}$$

and

$$\Delta\tau = (0.3 + r_1 + r_2)\,\Delta t / 10^6\ \text{s} \tag{34}$$

$$r_1 = exp\left[5000\left(\frac{1}{273.16} - \frac{1}{T_{snowsfc}}\right)\right] \tag{35}$$

$$\begin{aligned} r_2 &= r_1^{10} && r_1 \le 1 \\ r_2 &= 1 && r_1 > 1 \end{aligned} \tag{36}$$

ΔD is the change in snowpack depth in meters over the length of a model time step Δt. As can be seen in (33), an addition of 0.01 m of snowfall resets the snow albedo to that of new snow. The three terms of (34) account for changes in snow albedo due to accumulation of particulates, grain growth through vapor deposition, and grain growth through refreezing of melt water.

3.4 Model Orography

In addition to elevation influences on input temperature and pressure fields, elevation also is used in SHEELS for determining slope, which affects runoff, and aspect, an

important factor in determining insolation. The U.S. Geological Survey (USGS) has developed a hydrologically correct global elevation dataset based on a 30 arc-second digital elevation model (DEM; USGS, 2001). This HYDRO1k dataset provides raster-based elevation data at a 1-km resolution in which natural hydrologic sinks have been maintained, while artificial sinks have been removed. HYDRO1k data for the GYA were aggregated to an 8-km resolution by assigning the elevation of the 1-km pixel containing the center of the 8-km grid to the entire 8-km grid.

Using the 8-km resolution elevation data, slope and aspect were computed for overland flow and solar radiation absorption purposes. For each 8-km pixel, an average elevation was computed for each of the four sides of the pixel. This average was weighted based on the center-of-pixel distances to the three adjacent pixels on each side. For example, the northern average elevation $\overline{E}_N$ is given by

$$\overline{E}_N = w_c E_{NW} + w_m E_N + w_c E_{NE} \tag{37}$$

where E_{NW}, E_N, and E_{NE} are the elevations of the pixels lying to the northwest, north, and northeast, respectively, and the weights are

$$w_c = \frac{1}{2+\sqrt{2}} \tag{38}$$

$$w_m = \frac{\sqrt{2}}{2+\sqrt{2}}. \tag{39}$$

Slope across the grid cell γ was then computed using the average elevations

$$\gamma = \left[\left(tan^{-1} \frac{\overline{E}_E - \overline{E}_W}{2 \cdot 8000\text{m}} \right)^2 + \left(tan^{-1} \frac{\overline{E}_N - \overline{E}_S}{2 \cdot 8000\text{m}} \right)^2 \right] \tag{40}$$

where the subscripted E, W, N, and S represent the cardinal directions. Similarly, aspect β is given by

$$\beta = tan^{-1} \frac{tan^{-1}\left(\overline{E}_N - \overline{E}_S\right)}{tan^{-1}\left(\overline{E}_E - \overline{E}_W\right)}. \tag{41}$$

This value is then subtracted from either 270° [denominator in (41) is positive] or 90° [denominator in (41) is negative] such that aspect is measured clockwise from north.

3.5 Modeling of the Surface Energy Budget

SHEELS calculates the terms of the surface energy budget given by

$$R_{net} = H + LE + G + Q_{precip} \tag{42}$$

where R_{net} is net radiation, H sensible heat flux, LE latent heat flux, G ground heat flux, and Q_{precip} the flux of energy due to precipitation falling on the surface. As is customary, radiative fluxes in (42) are taken as positive towards the surface, whereas all other fluxes are positive away from the surface. Energy storage within the canopy and conversion of energy through biochemical processes are considered negligible. It should also be noted that the "ground" heat flux term in (42) represents a flux of energy into or out of the combined snow-soil column when snow cover exists.

3.5.1 Radiative fluxes

Net radiation R_{net} is the sum of incoming and outgoing shortwave and longwave radiation. Incoming shortwave (solar) radiation is a model input, as discussed in Section 22.3..2. However, downwelling solar radiation input into the SHEELS model is measured or modeled incident to a horizontal plane. That is, it is assumed that the measurement is made normal to the gravitational acceleration vector. Terrain slope and aspect may then result in increased or decreased absorption of solar radiation by the surface since the local ground plane may face more towards or away from the sun's position in the sky at any given time of day. Since terrain variations are considerable over the GYA domain, the equivalent slope concept of Lee (1964) has been implemented within SHEELS. This concept states that there is a point with latitude ϕ_{eq} and longitude λ_{eq} where the radiation incident to a horizontal plane is equal to that incident to a sloped plane at latitude ϕ and longitude λ. This equivalent point is given by

$$\lambda_{eq} = \lambda + tan^{-1}\left(\frac{sin\gamma\, sin\beta}{cos\beta cos\phi - sin\beta sin\phi cos\gamma}\right) \tag{43}$$

$$\phi_{eq} = sin^{-1}\left(sin\beta cos\gamma cos\phi + sin\phi cos\beta\right) \tag{44}$$

where γ is the slope angle and β is the aspect (measured positive from north).

Top-of-atmosphere solar radiation incident to a horizontal plane is computed for each model grid cell (k_{TOA}) and it's equivalent slope point (k_{eq}) for each time step such that

$$k_{TOA} = S_o[sin\delta sin\phi + cos\delta cos\phi cos(\omega t)] \quad (45)$$

$$k_{eq} = S_o[sin\ \delta\ sin\ \phi_{eq} + cos\ \delta cos\ \phi_{eq}\ cos\ (\omega t_{eq})] \quad (46)$$

where S_o is the solar constant (1370 Wm^{-2}), δ is the solar declination, ω is the angular velocity of the earth (15 $°hr^{-1}$), and t and t_{eq} are differences between local solar time at the grid point or equivalent slope point and local solar noon, positive after solar noon. By taking the ratio of these two values at each time step, a time-varying slope adjustment factor s_{fac} is calculated

$$s_{fac} = k_{eq}/k_{TOA} = \frac{sin\delta sin\phi_{eq} + cos\delta cos\phi_{eq} cos(\omega t_{eq})}{sin\delta sin\phi + cos\delta cos\phi cos(\omega t)}. \quad (47)$$

The slope adjustment factor is then used to scale the input value of downwelling solar radiation k_{input} to correct for terrain slope and aspect:

$$k_{corrected} = s_{fac} k_{input}. \quad (48)$$

Reflection of shortwave radiation is determined by soil albedo, plant surface albedo, and fractional vegetation cover, all model inputs, in addition to the previously described snow albedo. It should be mentioned here that while surface albedo may change considerably following the 1988 GYA fires, the majority of this change is through removal of vegetation. Knowles (1993) reports fire-associated soil albedo

increases of about 0.05 for the GYA. Tests with SHEELS indicate that such small changes in soil albedo have negligible effect on model results, thus soil albedo changes resulting from the fires have not been considered. Alterations in total albedo resulting from vegetation loss will be captured through use of NDVI to vary fractional vegetation cover with time as described above.

Emission of longwave (terrestrial) radiation $L_{emitted}$ is given by the Stefan-Boltzmann equation applied to the vegetated and unvegetated portions of each model grid cell:

$$L_{emitted} = \sigma[(1-\sigma_f)\varepsilon_{sfc}T_{sfc} + \sigma_f T_{can}]. \quad (49)$$

Here, σ is the Stefan-Boltzmann constant (5.67×10^{-8} W m^{-2} K^{-1}), ε is emissivity, T is temperature, and the sfc and can subscripts distinguish values for the unvegetated snow or soil surface and the canopy, respectively. As was illustrated in table 3, soil surface emissivity is a function of input land cover type, whereas the canopy is taken as a blackbody emitter. Modeling of T_{sfc} and T_{can} is described in section 3.5.4 The final radiative flux, downwelling longwave radiation, is an input variable and was discussed in section 2.4.

3.5.2 Turbulent fluxes

Bulk aerodynamic parameterizations are used within SHEELS to estimate fluxes of latent and sensible heat over bare soil, vegetated, snow, and liquid water surfaces. In vegetated areas, fluxes occur between the ground and within-canopy air, between

plant surfaces and within-canopy air, and between within-canopy air and above-canopy air. In areas lacking vegetation, fluxes occur only between the ground, water, or snow surface and the overlying atmosphere. Partitioning of fluxes from bare snow or soil versus those from vegetated surfaces is controlled through the fractional vegetation cover σ_f described above.

In calculating sensible and latent heat fluxes, the bulk aerodynamic approach relies on differences between atmospheric temperature T_a or specific humidity q_a and the surface values of these quantities T_s or q_s, as well as wind speed U and a drag coefficient for heat exchange C_h or moisture exchange C_m:

$$H = \rho c_p C_h U(T_a - T_s) \tag{50}$$

$$LE = \rho L C_m U(q_a - q_s). \tag{51}$$

Air density ρ is calculated on the basis of input values of atmospheric temperature, humidity, and pressure, while the latent heat of vaporization L is a function of temperature only. c_p is the specific heat of dry air at constant pressure (1004 $J\,kg^{-1}\,K^{-1}$).

Drag coefficients C_h and C_m in (50) and (51) must be adjusted to account for stability influences. Stability is determined by a surface bulk Richardson number that is a function of the input above-canopy air temperature and wind speed, and modeled values of the within-canopy air temperature and soil surface temperature. Drag

coefficients, canopy and soil temperatures, and surface fluxes must be solved in an iterative fashion due to the dependence of the bulk Richardson stability criterion on the within-canopy and soil surface temperatures, and their dependence on the surface energy balance.

Latent heat flux from the ground or snow surface is based on the saturation specific humidity at the calculated surface temperature (potential evapotranspiration), which is then adjusted to account for water availability using the approach of Federer (1982). Water availability is determined by antecedent precipitation and evapotranspiration, as described below.

3.5.3 Soil moisture

Input rainfall may be intercepted by the vegetation canopy, infiltrate into the soil column, or pond on the soil surface. Canopy interception is a function of the fractional vegetation cover within a model grid cell. Infiltration of rainfall or snow melt is controlled through input soil properties for each soil zone using Richard's equation, as described below. Rain or snow melt in excess of the infiltration rate is stored as surface ponding or becomes runoff from a model grid cell. Sources of liquid water available for evaporation include canopy-intercepted rainfall and liquid water in the upper soil zone or top snow layer. Sublimation may occur from the top snow layer in the absence of liquid water within that layer. Furthermore, root zone soil moisture may enter the atmosphere via transpiration, which differs from direct

evaporation via a modeled stomatal resistance term that is dependent upon the available soil moisture, air temperature, and vegetation type as suggested by Jarvis (1976).

In addition to modifications for modeling of snow within SHEELS being necessary for its use in the GYA, the extremely cold wintertime temperatures encountered in this area necessitate modeling of frozen soil physics. Specifically, energy used in water phase changes must be accounted for in computation of the vertical soil temperature profile (section 3.5.4) and the hydrologic effects of frozen water in soil layers must be modeled.

The formation of ice crystals in the soil matrix and ice lenses (horizontal layers of ice) within the soil column impede the infiltration of liquid water. The complexity of such processes prevents explicit, physically realistic modeling of the concomitant changes in hydraulic conductivity in a computationally feasible manner. However, much research has been done attempting to quantify these ice-induced changes through the use of an empirically derived *effective* hydraulic conductivity K_f. Often, K_f is related to the actual hydraulic conductivity K in an exponential manner. Lundin (1990) provides the formulation

$$K_f = 10^{-E_i \alpha} K \tag{52}$$

where the thermal quality α can be related to the fractional liquid water and ice contents (per pore volume) by

$$\alpha = \frac{f_{ice}}{f_{ice} + 1.09\, f_{wat}}. \tag{53}$$

E_i in (61) is an empirical impedance factor that varies with soil type, such that E_i is generally proportional to soil particle size. Table 5 shows impedance factor values used for the eleven soil types in SHEELS, which are based on Lundin's (1990) review of the pertinent literature. The unimpeded hydraulic conductivity K is a function of total soil moisture and can be expressed as

$$K = K_{sat}\left(f_{wat} + f_{ice}\right)^{(2b+3)} \tag{54}$$

where b is a soil type-dependent empirical parameter (Clapp and Hornberger, 1978).

Table 5: Hydraulic conductivity impedance factors for various soil types.

Soil Type	Impedance Factor E_i
Sand	8
Loamy sand	7
Sandy loam	6
Silt loam	5
Loam	5
Sandy clay loam	4
Silty clay loam	4
Clay loam	4
Sandy clay	3
Silty clay	2
Clay	2

Richard's equation is used to determine the time rate of change of the soil sublayer fractional water content resulting from diffusion and gravitational drainage

$$\partial f_{wat}/\partial t = 1/\phi\left[\partial/\partial z\left(K_f\,\partial\psi/\partial z\right) + \partial K_f/\partial z\right] \tag{55}$$

where t is time, ϕ is the soil porosity, and z is depth. The soil water potential ψ is based on f_{wat}, f_{ice}, and the input saturated soil water potential ψ_{sat} using the formulation of Clapp and Hornberger (1978):

$$\psi = \psi_{sat}\left(f_{wat} + f_{ice}\right)^{-b}. \tag{56}$$

Equation (55) can be rewritten as

$$\partial f_{wat}/\partial t = 1/\phi\left\{\partial/\partial z\left[D\left(\partial f_{wat}/\partial z + \partial f_{ice}/\partial z\right)\right] + G_{wat}\,\partial f_{wat}/\partial z + G_{ice}\,\partial f_{ice}/\partial z\right\} \tag{57}$$

where

$$D = K_f\,\partial\psi/\partial f_{wat} = K_f\,\partial\psi/\partial f_{ice} = \frac{-bK_f\psi}{f_{wat} + f_{ice}}, \tag{58}$$

$$G_{wat} = \partial K_f/\partial f_{wat} = K_f\left(\frac{1.09E_i\alpha\,ln10}{f_{ice} + 1.09f_{wat}} + \frac{2b+3}{f_{ice} + f_{wat}}\right), \tag{59}$$

and

$$G_{ice} = \partial K_f/\partial f_{ice} = K_f\left(-\frac{E_i f_{wat}1.09\,ln10}{\left(f_{ice} + 1.09f_{wat}\right)^2} + \frac{2b+3}{f_{ice} + f_{wat}}\right). \tag{60}$$

This is similar to the derivation of Martinez et al. (2001), except that the hydraulic conductivity is now a function of the fractional ice content of the soil layer as well as the fractional liquid water content, resulting in different D and G_{wat} formulations and the addition of the G_{ice} term in (57).

3.5.4 Ground heat flux and soil and snow temperatures

Calculation of soil and snow temperatures, including surface temperature, is through semi-implicit solution of the thermal diffusion equation,

$$\rho_s c_{p,s} \frac{\partial T}{\partial t} = Q + \nabla \cdot (k \nabla T) \tag{61}$$

where ρ_s is the soil or snow density, $c_{p,s}$ and k are the specific heat at constant pressure and thermal conductivity, T is the temperature at the surface or within a layer, and ∇T represents the vertical gradient of temperature in the combined snow-soil column. Surface thermal forcing by net radiation, atmospheric turbulent fluxes, and heat transport via precipitation are represented by Q.

Both specific heat and thermal conductivity are adjusted to account for soil moisture or snow layer liquid water content. In the case of soil, thermal conductivity within the layers is assumed to not change with the presence or absence of ice in the layer. Thus, the thermal conductivity is a function soil type and the fractional content of water within the layer, regardless of the water's phase ($f_{wat} + f_{ice}$). For snow layers, a

dry snow thermal conductivity k_{dry} is calculated first. Sturm et al. (1997) made nearly 500 measurements of snow density and thermal conductivity over a 12-year period and have developed a regression relationship between these two variables:

$$k_{dry} = 0.138 - 1.01\left(\frac{\rho_{snow}}{1000}\right) + 3.233\left(\frac{\rho_{snow}}{1000}\right)^2 \qquad 156 \le \rho_{snow} \le 600$$
$$k_{dry} = 0.023 + 0.234\left(\frac{\rho_{snow}}{1000}\right) \qquad \rho_{snow} < 156 \tag{62}$$

where ρ_{snow} is in kg m^{-3} and the resulting value of k_{dry} is in W m^{-1} K^{-1}. For snow densities greater than 600 kg m^{-3}, thermal conductivity is based on a linear extrapolation of (62) to the thermal conductivity of ice (2.51 W m^{-1} K^{-1}) at a density of 1000 kg m^{-3}. The dry snow thermal conductivity is then adjusted for liquid water content using data from Singh (1999) such that

$$k = k_{dry} + 0.17\ \mathrm{Wm^{-1}K^{-1}}\frac{D_{lw}}{D_{snow}} \tag{63}$$

where D_{lw} is the depth of liquid water occurring in the snow layer having thickness D_{snow}.

Water phase changes can provide a significant source or sink of thermal energy, especially within snow layers. To accommodate this, individual soil and snow layer temperatures are compared to their previous values following solution of the heat diffusion equation. If the temperature of a layer crosses the freezing point, the temperature of that layer is set to the freezing point and the additional loss or gain of

energy from the layer is used in water phase changes. Only once all water within the layer has become either liquid or solid is the temperature of that layer allowed to change beyond the freezing point. Since this isothermal period of phase change alters the previous solution of the heat diffusion equation, the equation is recomputed for the remainder of the soil-snow column.

It is through the above mechanism that model snow layers melt. This, as well as rainfall on the snow surface, act to increase the snow layer liquid water content. The maximum allowable liquid water content $D_{lw\text{-}max}$ is computed in a manner identical with that of the Interactions between Soil, Biosphere, and Atmosphere – Explicit Snow (ISBA-ES) model as reported by Boone and Etchevers (2001):

$$\begin{aligned} D_{lw-max} &= W\left[0.03 + \frac{0.07(200 - \rho_{snow})}{200}\right] && \rho_{snow} < 200 \text{ kg m}^{-3} \\ D_{lw-max} &= 0.03\, W && \rho_{snow} \geq 200 \text{ kg m}^{-3} \end{aligned} \tag{64}$$

where W is the layer snow water equivalent and ρ_{snow} is the layer snow density. Liquid water in excess of the maximum is transferred to the next lower layer. Cumulative water transferred out of the bottom-most layer forms ponded water which is subsequently infiltrated into the soil or runoff.

Coincident with the conversion of snow to liquid water is a reduction in snow layer thickness. Simultaneous solution of the soil or snow surface temperature and the resulting latent and sensible heat fluxes to the atmosphere requires an iterative

approach in which the number of iterations is inversely proportional to layer thicknesses. Consequently, snow layers cannot be allowed to become excessively thin or computational time for solution of the diffusion equation grows unboundedly. To alleviate this potential problem, snow ablation resulting in layer thickness becoming less than 2.5 mm results in combination of that layer with an adjacent snow layer. Similarly, if the total snowpack depth falls below 2.5 mm, the remaining snow water equivalent is converted to liquid water.

In addition to (61) providing solution to the soil surface and subsurface temperatures, evolution of ∇T also provides a means for determining ground heat flux. Changes in temperature within the top snow or soil layer and fluxes of heat from that layer to the layer below are summed within the model to calculate this final surface energy budget variable.

4 Analysis of Model Output for the GYA

With the meteorological and topographic inputs described in chapters 2 and 3, SHEELS is capable of estimating a diverse range of meteorological and hydrological variables for the Greater Yellowstone Area model domain. Four model scenarios have been run to examine the effects of the 1988 fires on surface energy budget and soil moisture variables within various areas of the GYA. The scenarios and area subsets are described in section 4.1, while time series and diurnal averages of model outputs are presented in sections 4.2 and 4.3. These results are then discussed in section 4.4.

4.1 Areas of Comparison and Model Scenarios

To elucidate the impact of the fire-induced vegetation changes in the GYA, four different model scenarios have been utilized. Each scenario employs distinct combinations of meteorological and vegetation input data. Results from these model runs have been compared for three subset areas in the GYA: a burn region consisting of areas experiencing either crown fires or surface fires, a region upwind from the burn area, and a region downwind from the burn area. Here, "upwind" and "downwind" are in reference to the climatological wind direction, found by Dirks and Martner (1982) to be generally west to southwest in the GYA. Analysis of wind direction data from the three surface airway stations within the GYA also demonstrates a predominantly southwesterly flow (figure 14). The upwind area is

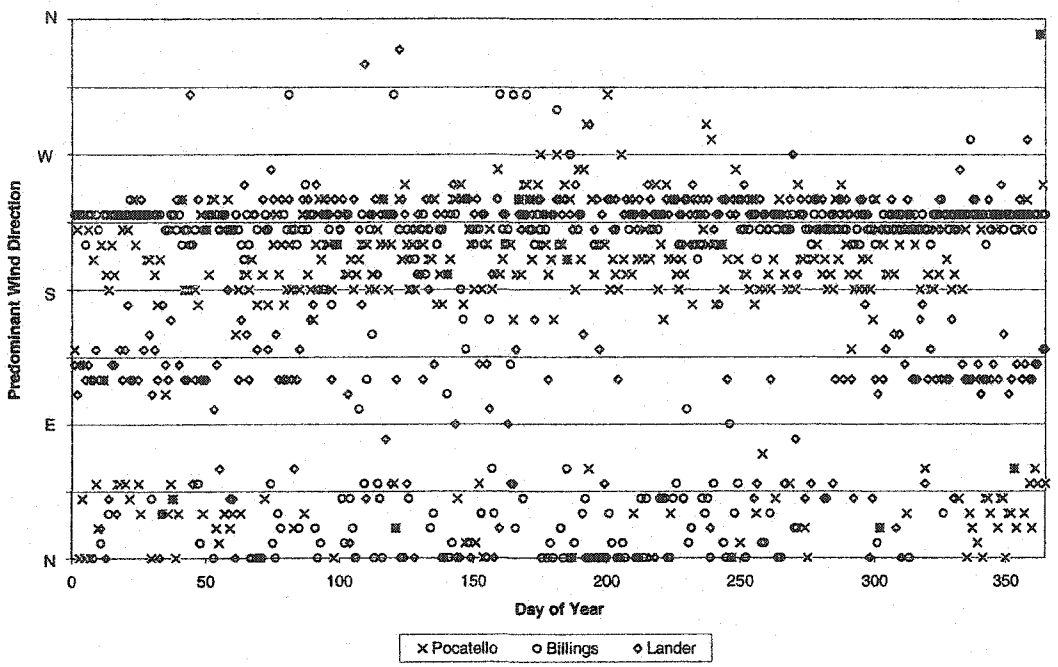


Figure 14: Predominant wind direction by day of year for the three surface airway stations in the GYA. Based on 1984-1993 observations.

thus of identical shape and size as the burn area, but is displaced to the west-southwest so as to have no overlap with the burn area. The downwind area is similarly displaced to the east-northeast of the burn area.

To aid discussion of the dataset comparisons, it is beneficial to identify the four possible manners in which SHEELS output may be affected by vegetation and meteorology in the GYA. First, changes in vegetation amount occur both seasonally and interannually, regardless of wildland fire. These changes will be termed "unassociated vegetation changes." A second manner in which output may be altered is through differences in meteorological forcing that are not associated with the fires.

These "unassociated climate changes" may result from random fluctuations in the atmospheric system, or more deterministic causes such as El Niño or the Pacific Decadal Oscillation.

While the previous two ways in which model output may be altered are independent of the 1988 fires, the other two ways are consequences of the fires. The alteration in vegetation brought about by the fires is expected to affect both evapotranspiration and total surface albedo. Resulting "fire vegetation changes" occur only in the burn area, not the upwind or downwind areas. Lastly, the fire vegetation changes may then alter atmospheric water vapor dynamics, leading to changes in regional precipitation patterns and creating "fire climate changes" that affect soil moisture and atmospheric fluxes. Walker and Rowntree (1977), Yeh et al. (1984), and Zheng and Eltahir (1998) have shown that soil moisture anomalies can be self-sustaining to an extent, as anomalies in soil evaporation produce precipitation anomalies. Thus, the effect of fire climate changes on modeled soil moisture and latent heat flux could be substantial.

4.1.1 Control (CTRL) dataset

The first set of model output values is a control set, in which model forcing is obtained directly from observations throughout the time period of the study. That is, observed meteorological and vegetation data have been input into the model both prior to and after the fires. Resulting hourly values of soil moisture, snow water

equivalent, and surface energy budget variables have been spatially averaged for each of the three subset areas and represent indigenous conditions over the GYA.

4.1.2 Vegetation forcing repeated (VFR) dataset

The second model scenario is one in which output variables are derived from repeating the vegetation forcing from the pre-fire period (1984-1988) during the post-fire period (1989-1993). Meteorological forcing in this scenario remains as observed for the entire 10-year period. In this manner, interannual and seasonal changes in vegetation are maintained, but the large-scale removal of vegetation by the 1988 fires is not realized within the model. Differences between vegetation forcing repeated dataset values and control dataset values over the burn area reflect the direct effects of the fire induced vegetation changes, as well as any unassociated vegetation changes, on soil moisture and surface energy budget variables. In contrast, a similar comparison between VFR and CTRL in the upwind and downwind areas allows determination of the degree to which unassociated vegetation changes alone affected soil moisture and fluxes. Consequently, differences over the burn area that arise from both fire and unassociated vegetation changes can be compared to differences over the upwind and downwind areas where only unassociated vegetation changes have occurred. This helps clarify how much of the differences seen in soil moisture and fluxes in the burn area arise solely as a result of the fire-induced vegetation changes.

4.1.3 Meteorological forcing repeated (MFR) dataset

Repeating the meteorological forcing while using observed vegetation data throughout the study period produced the third dataset of surface energy budget, soil moisture, and snow water equivalent values. In this case, the day-to-day weather for the post-fire period is identical to that of the pre-fire period, but effects from the fire-induced vegetation changes are preserved. By comparing output from this model run to the control run over the upwind area, differences in water variables and fluxes resulting from unassociated climate changes may be determined. Differences in the burn and downwind areas between values from this dataset and the control dataset reflect both unassociated climate changes and fire climate changes.

4.1.4 Both forcings repeated (BFR) dataset

The fourth dataset consists of values derived by repeating the meteorological and vegetation forcing from the period before the fires during the model period after the fires. Thus, changes resulting from the fires will not be represented in the model, however interannual variability in vegetation amount and meteorological forcing will remain. It should be noted that, aside from short-lived changes resulting from slightly different initial conditions, the second half of this dataset is identical to the first half and is included in this discussion for completeness. The actual model run used to produce this dataset simulated only the 1984-1988 period to minimize computer time.

Model results for this dataset reflect soil moisture, snow water equivalent, and atmospheric fluxes had the major vegetation changes, and any possible ensuing changes in atmospheric forcing, not occurred. Over the upwind area, differences between soil moisture, snow water equivalent, and flux values from this dataset and those from the control dataset demonstrate the degree to which these variables in the upwind region were impacted by unassociated vegetation changes and unassociated climate changes. Over the burn area, differences between this dataset and the control dataset reflect the total impact of all changes: unassociated vegetation changes, fire vegetation changes, unassociated climate changes, and fire climate changes. The differences over the downwind area from the control dataset represent changes brought about by unassociated vegetation changes and both unassociated and fire climate changes.

4.2 Spatially Averaged Time Series

This section presents time series of daily-averaged data that also have been spatially averaged over the subset areas. These data include radiative, turbulent, and ground heat fluxes, snow water equivalent, and soil total liquid water content. As previously stated, the 1989-1993 BFR dataset is identical to all of the pre-fire period datasets. Thus, the pre-fire period will not be explicitly discussed, but can be inferred from the BFR comparisons.

4.2.1 Radiative fluxes

Figures 15-17 illustrate the radiation budget for the burn, upwind, and downwind areas during the post-fire period for each of the four model scenarios. Most evident in these figures is the large annual variation in net shortwave radiation. Low solar elevation, short periods of solar insolation, and the high albedo of snow cover all contribute to very low wintertime values of absorbed solar radiation.

Less obvious is the annual cycle in net longwave radiation, which is best seen in the burn and upwind areas (figures 15 and 16). Net longwave minima occur in early October when cool atmospheric temperatures result in weak downwelling longwave radiation while the soil is still relatively warm and consequently emitting a large amount of thermal radiation. Accumulation of snow on the soil surface quickly attenuates this large emittance, causing a rapid increase in net longwave radiation as winter progresses. This results in a highly non-sinusoidal annual cycle.

As might be expected, differences in the radiation budget between the CTRL and VFR scenarios are quite small for the upwind area (figure 16 a and c). Such differences would result solely from changes in vegetation amount from the pre-fire period to the post-fire period, and since this area was not affected by the 1988 fires, the change in vegetation forcing was small. This is similarly true for the downwind area (figure 17 a and c). Root mean square (RMS) differences between VFR and

CTRL net shortwave flux were 1.9 Wm^{-2} and 2.5 Wm^{-2} for the upwind and downwind areas, respectively (see table 6). RMS differences were also small for net longwave flux, with an upwind area difference of 1.8 Wm^{-2} and a downwind area difference of 2.3 Wm^{-2}. These RMS differences were calculated after removal of the average difference, as is the case for all RMS differences presented subsequently.

Radiation budget differences between the VFR and CTRL scenarios were slightly larger over the burn area (figure 15 a and c), but still small. Here, RMS differences for net shortwave and net longwave fluxes were 5.9 Wm^{-2} and 3.7 Wm^{-2}. Average differences of these fluxes were 2.8 Wm^{-2} and -2.6 Wm^{-2}, indicating somewhat more absorption of solar radiation, apparently resulting in warmer surface temperatures and slightly greater longwave emittance.

Table 6: Average and RMS differences in radiative fluxes for the various model scenarios.

		Net Shortwave Flux (Wm^{-2})		Net Longwave Flux (Wm^{-2})	
		Avg. Diff.	RMS Diff.*	Avg. Diff.	RMS Diff.*
Burn	VFR-CTRL	2.82	5.85	-2.60	3.66
	MFR-CTRL	1.59	37.25	-1.96	16.94
	BFR-CTRL	4.89	38.77	-4.70	18.19
Upwind	VFR-CTRL	0.06	1.91	0.20	1.82
	MFR-CTRL	-1.25	37.38	-0.74	17.83
	BFR-CTRL	-1.49	37.81	-0.25	18.13
Downwind	VFR-CTRL	0.02	2.52	0.47	2.29
	MFR-CTRL	0.73	42.48	-1.81	17.45
	BFR-CTRL	0.82	42.88	-1.48	17.55

* RMS differences after removal of the mean difference.

Comparisons of the net shortwave and net longwave fluxes between the CTRL and MFR datasets (figures 15-17 a and b) show considerably larger RMS differences for all three area subsets. This is also seen in a comparison between the CTRL and BFR datasets (figures 15-17 a and d), which have RMS differences of similar magnitude. The large RMS differences resulting from repeating the meteorological forcing indicate that disparities between the pre-fire and post-fire climate had a substantially larger effect on variability of radiative fluxes than did vegetation changes.

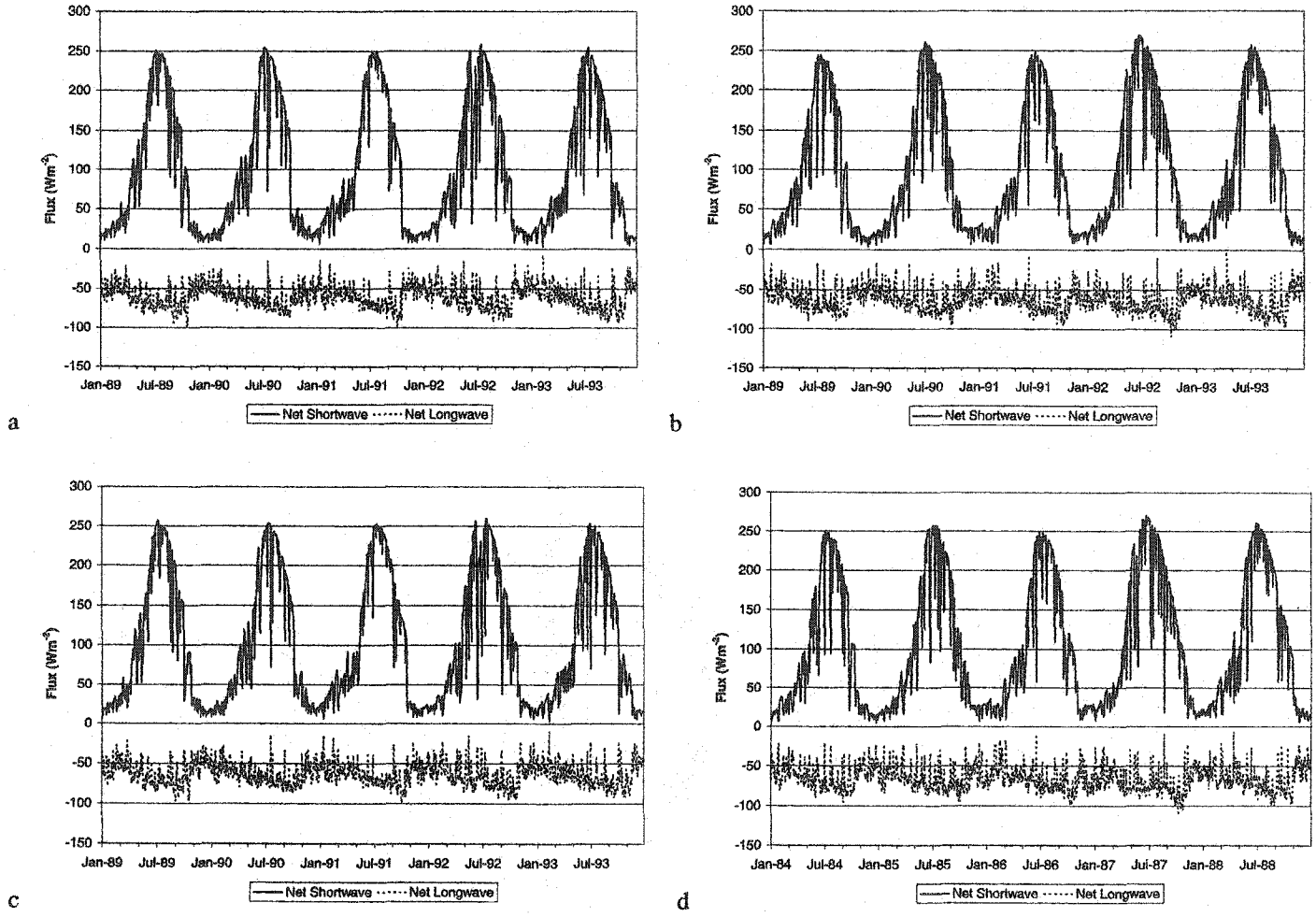


Figure 15: Spatially averaged time series of radiative fluxes over the burn area for a) CTRL, b) MFR, c) VFR, and d) BFR scenarios.

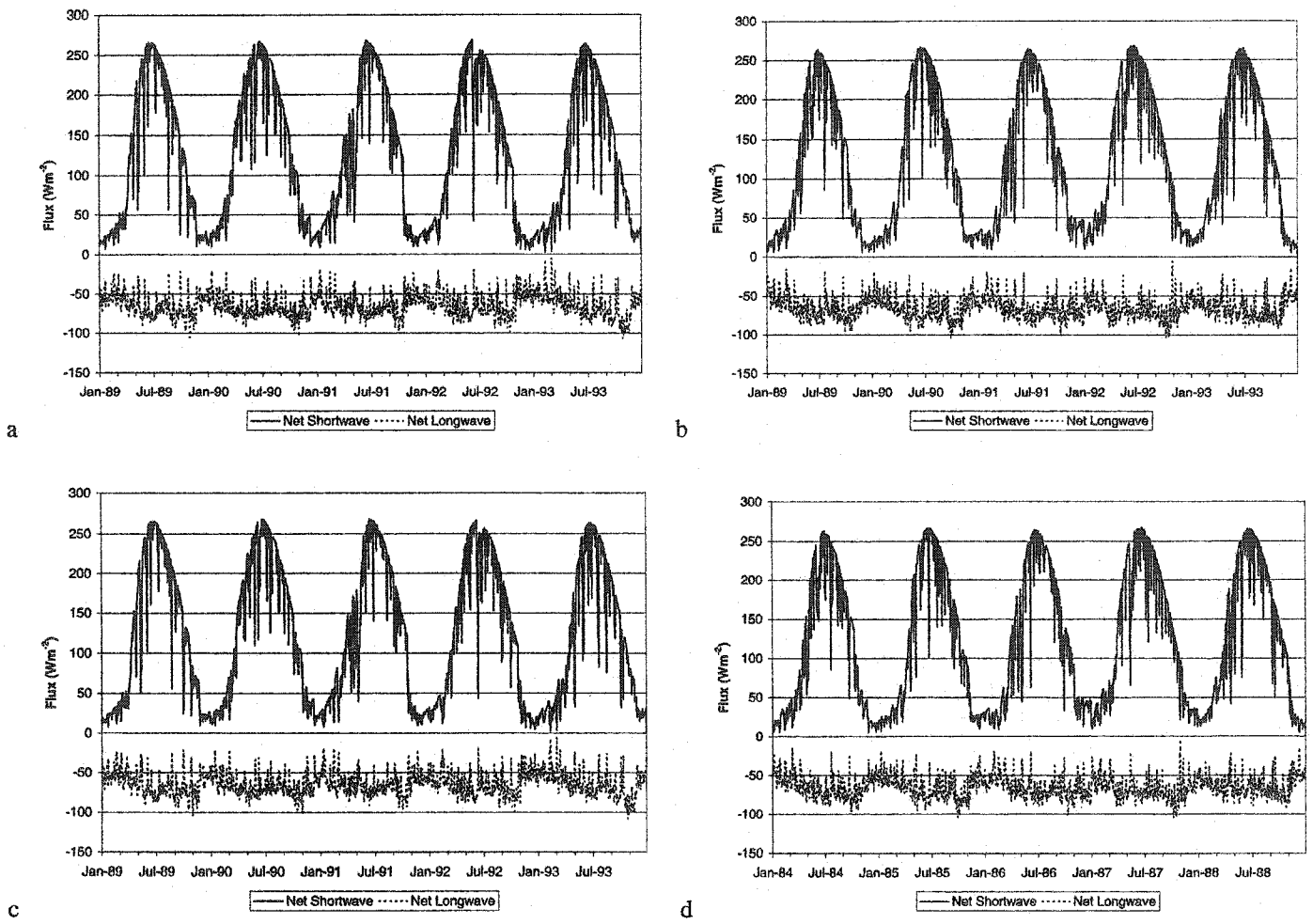


Figure 16: Spatially averaged time series of radiative fluxes over the upwind area for a) CTRL, b) MFR, c) VFR, and d) BFR scenarios.

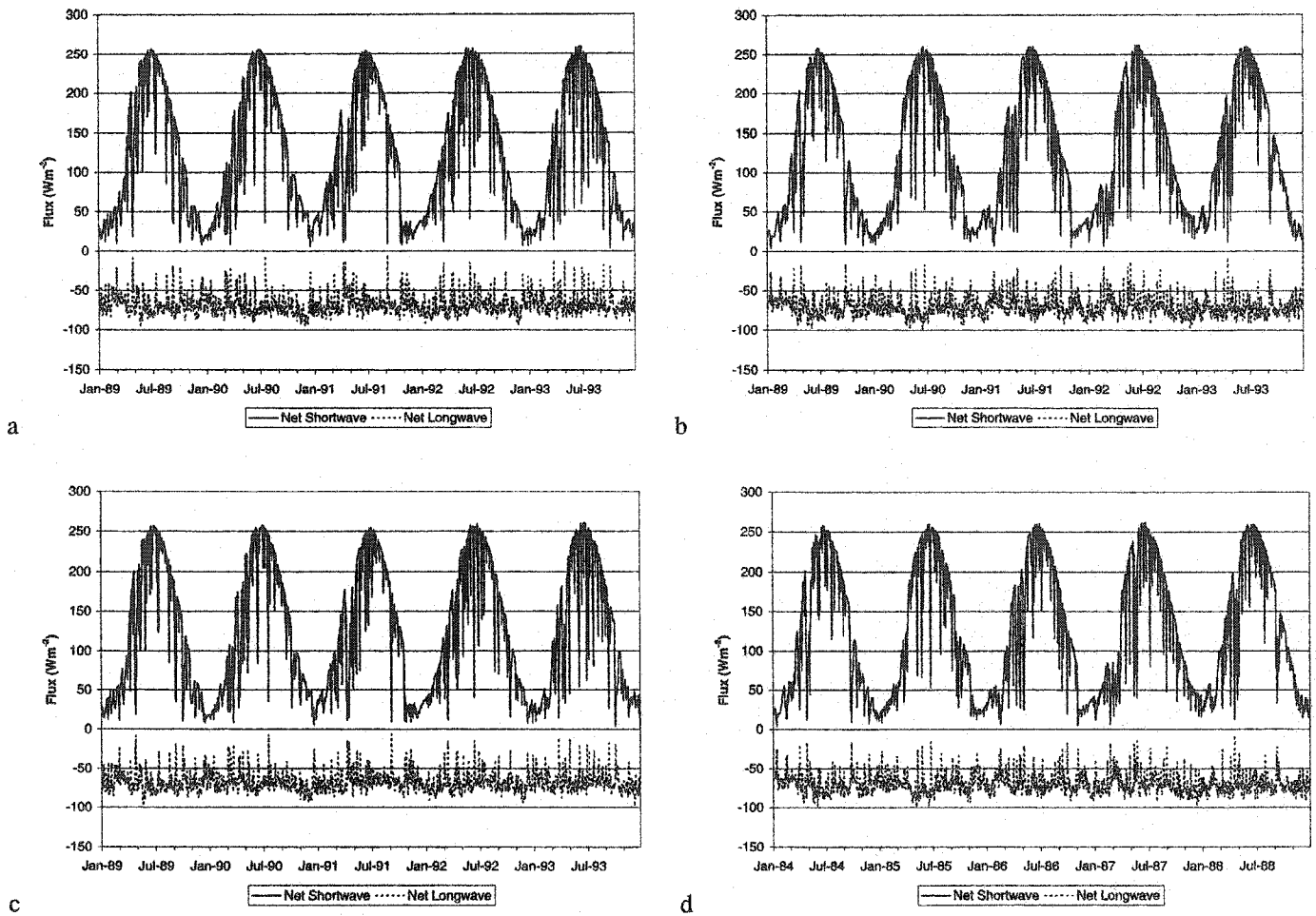


Figure 17: Spatially averaged time series of radiative fluxes over the downwind area for a) CTRL, b) MFR, c) VFR, and d) BFR scenarios.

4.2.2 Turbulent and ground heat fluxes

Time series of latent, sensible, and ground heat fluxes are illustrated in figure 18 (burn area), figure 19 (upwind area), and figure 20 (downwind area). Noteworthy are the consistently negative sensible heat fluxes and predominantly positive ground heat fluxes for all three area subsets. A possible explanation for these unusual results is discussed in section 4.4. Also apparent in these figures is the considerably smaller latent heat flux over the downwind area relative to the upwind and burn areas, regardless of the model run being examined. Smaller latent heat flux values indicate that the downwind area is generally drier than the other two areas, as will be shown in the next section.

As with the radiative fluxes, RMS differences between the CTRL and VFR model runs are considerably smaller than the RMS differences between the CTRL and MFR or BFR simulations for all three fluxes (table 7). Average differences are generally of similar magnitude for all of these comparisons as well, with the important exceptions of latent and sensible heat fluxes over the burn area. For these, average differences between CTRL and VFR are similar to those between CTRL and MFR, but considerably smaller than the CTRL-BFR differences. This alludes to a synergistic effect over the burn area where the combination of different vegetation and different climate results in greater changes in latent and sensible heat fluxes than are observed for either forcing difference acting alone. This synergism is not seen in the upwind or

downwind areas where differences in latent and sensible heat fluxes between the CTRL and BFR scenarios are similar to those found comparing the CTRL scenario with the VFR or MFR simulations.

Table 7: Average and RMS differences in turbulent and ground heat fluxes for the various model scenarios.

		Latent Heat Flux (Wm^{-2})		Sensible Heat Flux (Wm^{-2})		Ground Heat Flux (Wm^{-2})	
		Avg. Diff.	RMS Diff.*	Avg. Diff.	RMS Diff.*	Avg. Diff.	RMS Diff.*
Burn	VFR-CTRL	8.59	20.17	-7.63	17.28	-0.73	5.25
	MFR-CTRL	12.43	50.86	-8.01	41.32	-4.81	36.34
	BFR-CTRL	23.60	59.27	-16.37	46.75	-7.05	36.74
Upwind	VFR-CTRL	-0.91	6.28	0.63	6.11	0.55	2.98
	MFR-CTRL	4.56	57.28	-2.96	52.71	-3.58	39.71
	BFR-CTRL	2.92	58.40	-2.05	53.57	-2.61	39.53
Downwind	VFR-CTRL	0.76	6.50	-1.99	7.58	1.71	5.45
	MFR-CTRL	5.32	49.34	-4.59	54.06	-1.79	44.69
	BFR-CTRL	3.76	49.25	-3.24	54.89	-1.19	44.18

* RMS differences after removal of the mean difference.

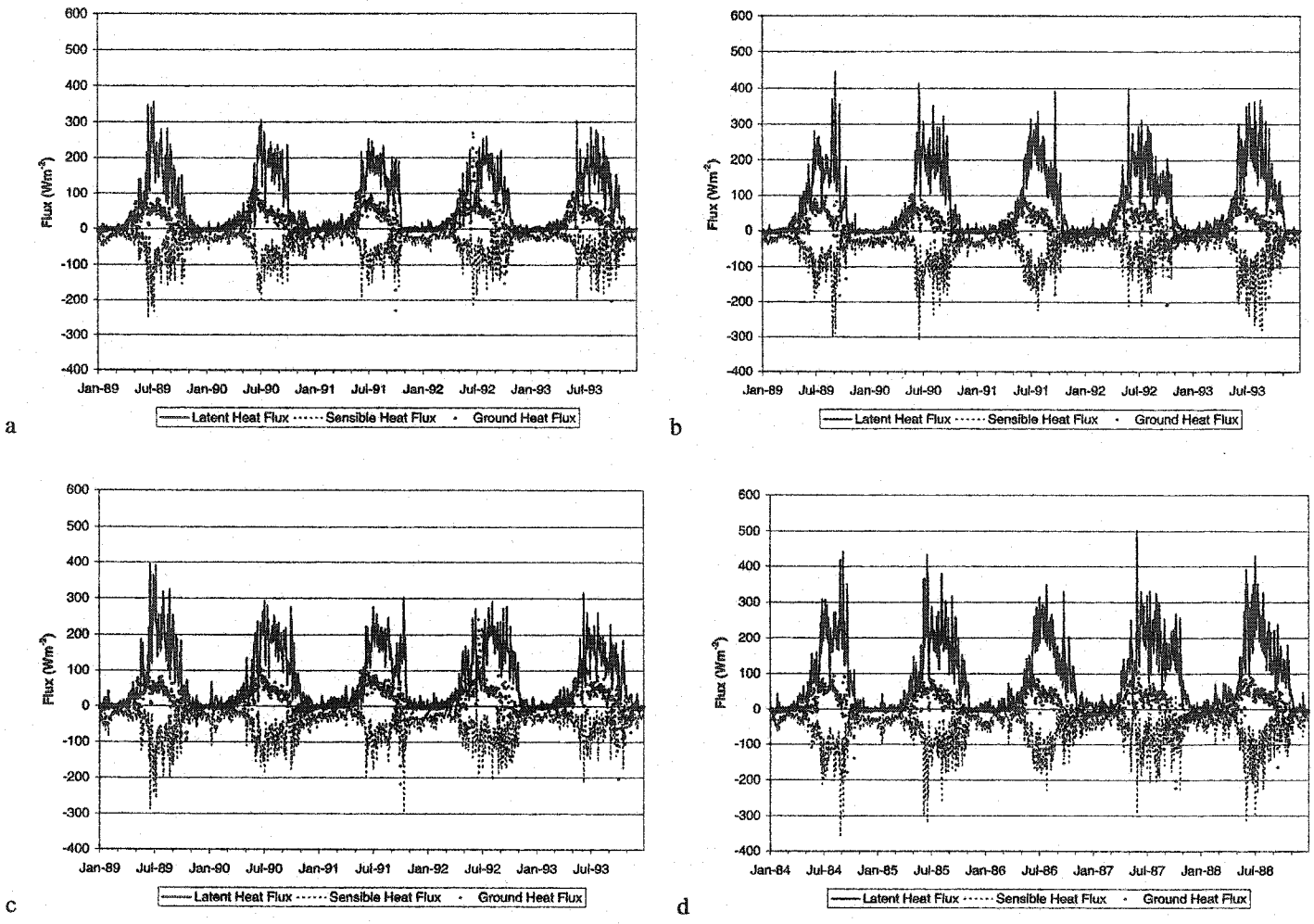


Figure 18: Spatially averaged time series of turbulent and ground heat fluxes over the burn area for a) CTRL, b) MFR, c) VFR, and d) BFR scenarios.

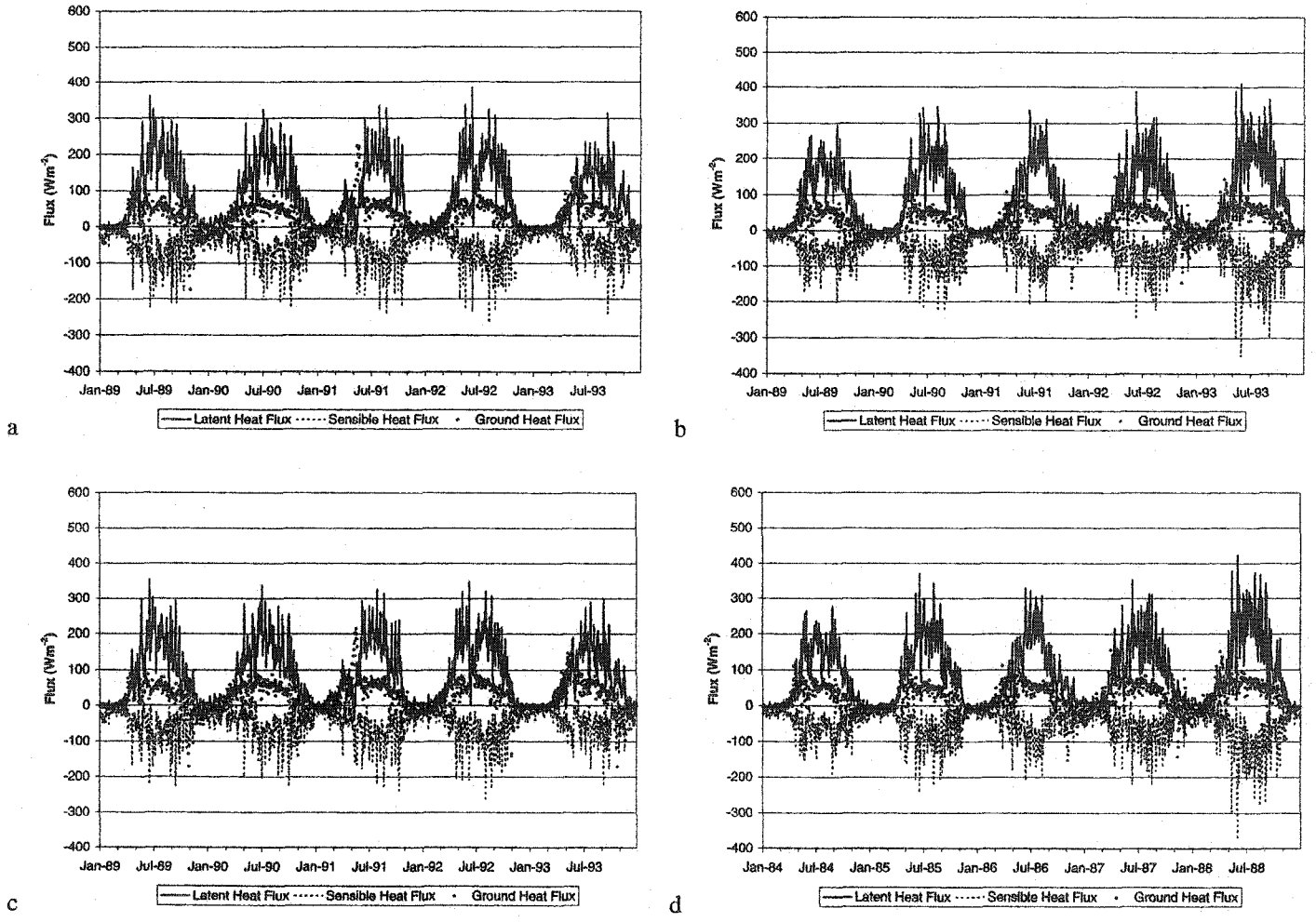


Figure 19: Spatially averaged time series of turbulent and ground heat fluxes over the upwind area for a) CTRL, b) MFR, c) VFR, and d) BFR scenarios.

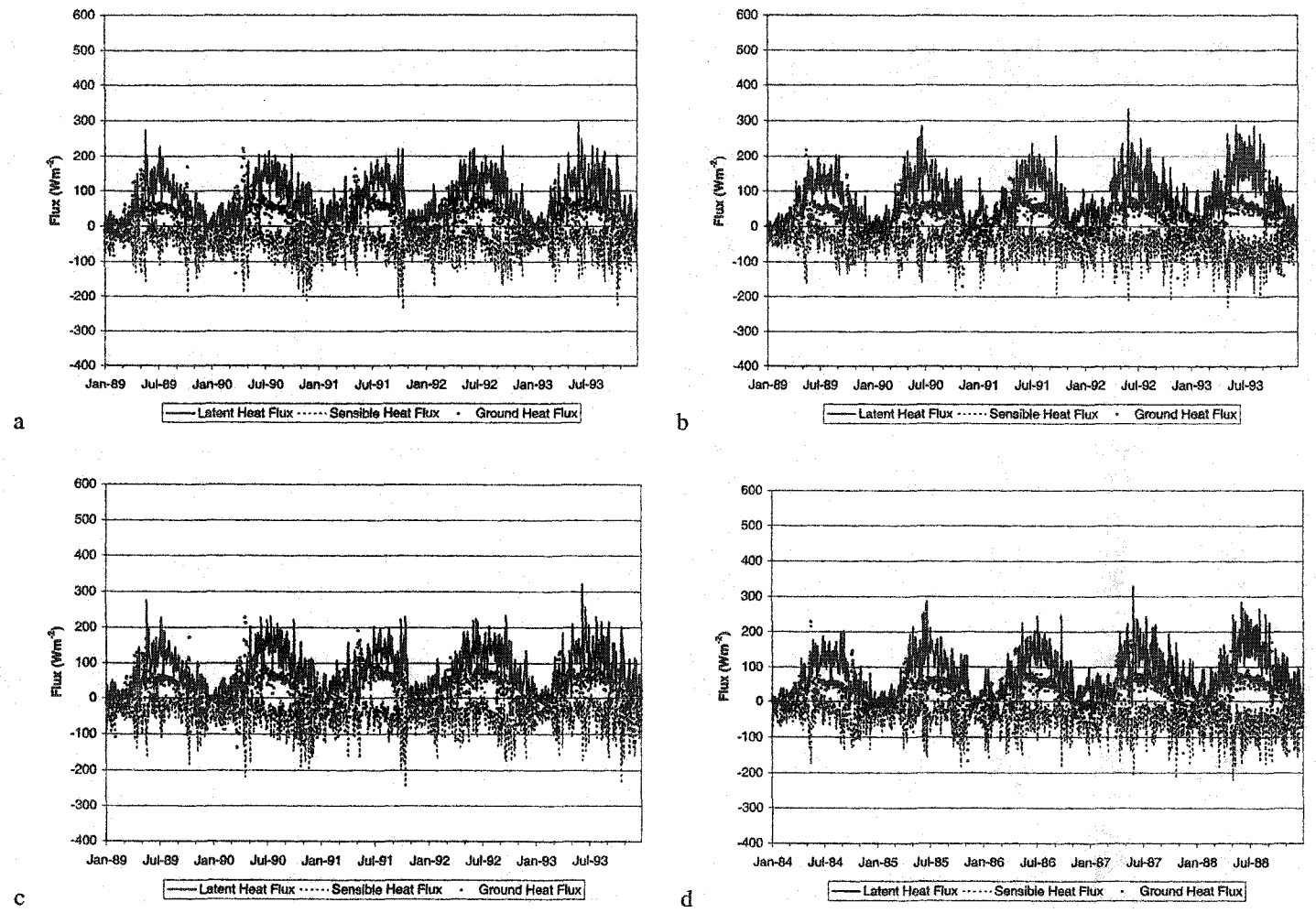


Figure 20: Spatially averaged time series of turbulent and ground heat fluxes over the downwind area for a) CTRL, b) MFR, c) VFR, and d) BFR scenarios.

4.2.3 Soil water content and snow water equivalent

Figures 21, 22, and 23 present spatially averaged time series of snow water equivalent and total depth of liquid water within the soil column for the burn, upwind, and downwind areas. Most obvious is the large difference in peak snow water equivalent between the burn, upwind, and downwind regions. Elevations of these three areas are considerably different, with the burn area having an average elevation of 2490 m, while the upwind and downwind area average elevations are 1760 m and 1510 m, respectively. Cooler air and soil temperatures associated with the higher elevation of the burn area result in greater snowfall amounts and longer snowpack persistence in the burn area. The sparse snowpack and substantially lower soil water content of the downwind area help explain the relatively low latent heat fluxes observed in this region, as noted in section 4.2.2.

Again, RMS differences from the CTRL model run for the VFR run are considerably smaller than those for the other two model runs (table 8). The one exception to this is soil liquid water content over the downwind area. In this case, the VFR-CTRL RMS difference of 10 mm is roughly half that of the MFR-CTRL and BFR-CTRL comparisons. Also, the average difference for the VFR-CTRL comparison is nearly the same magnitude, although of opposite sign, as the MFR-CTRL and BFR-CTRL average differences. The VFR-CTRL differences in soil moisture occur in spite of

negligibly small deviations in snow water equivalent and differences in latent heat flux similar to those of the other areas.

Table 8: Average and RMS differences in soil liquid water content and snow water equivalent for the various model scenarios.

		Soil Liquid Water Content (mm)		Snow Water Equivalent (mm)	
		Avg. Diff.	RMS Diff.*	Avg. Diff.	RMS Diff.*
Burn	VFR-CTRL	-0.26	3.27	-6.14	7.08
	MFR-CTRL	-2.68	23.95	-11.85	48.86
	BFR-CTRL	-2.82	23.45	-17.77	50.47
Upwind	VFR-CTRL	-1.55	2.95	-0.07	1.42
	MFR-CTRL	-0.67	21.84	4.42	23.82
	BFR-CTRL	-3.61	21.18	5.03	24.73
Downwind	VFR-CTRL	4.84	8.71	-0.25	1.15
	MFR-CTRL	-5.22	18.86	-1.12	5.78
	BFR-CTRL	-8.83	20.06	-1.09	6.23

* RMS differences after removal of the mean difference.

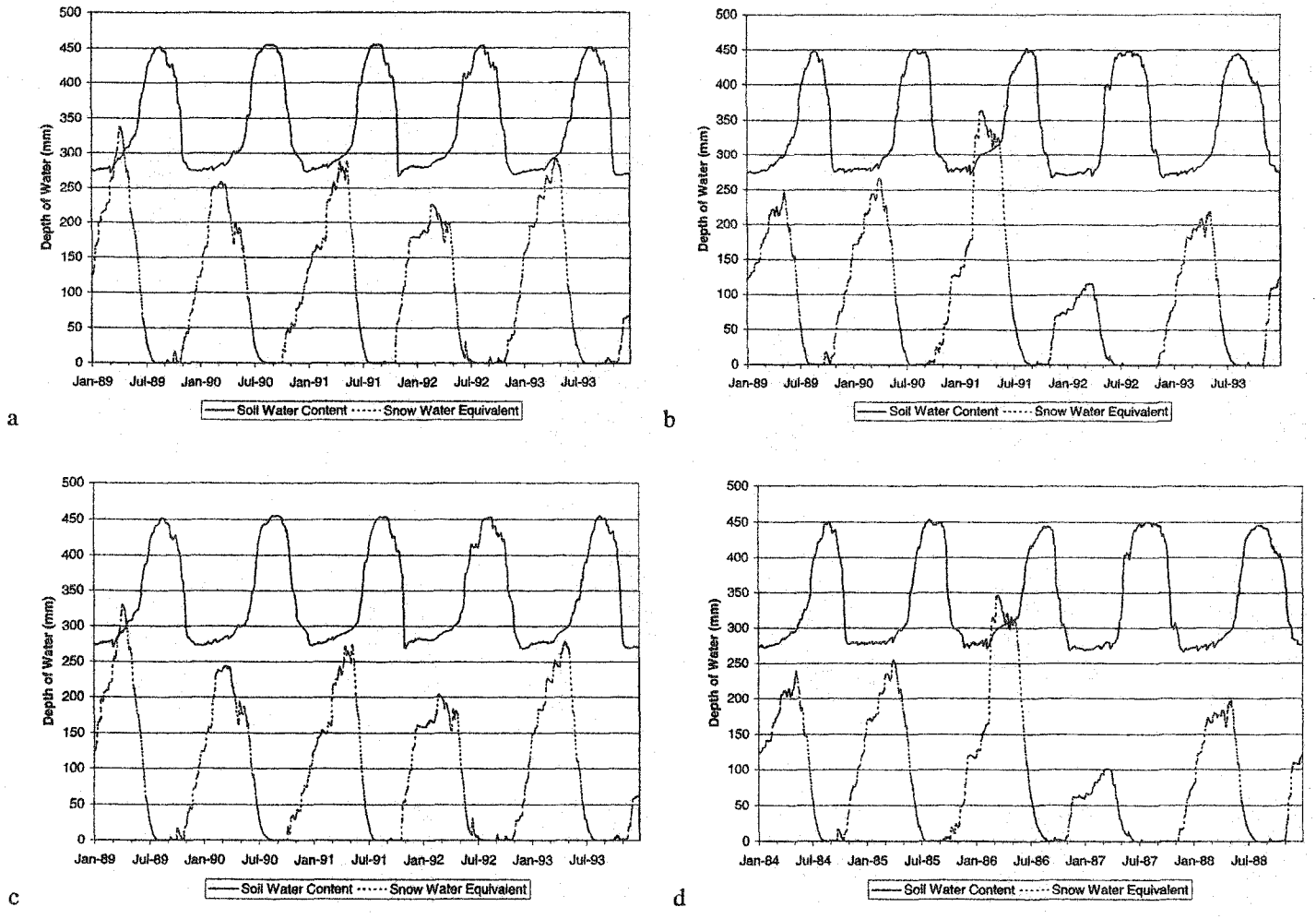


Figure 21: Spatially averaged time series of soil liquid water content and snow water equivalent over the burn area for a) CTRL, b) MFR, c) VFR, and d) BFR scenarios.

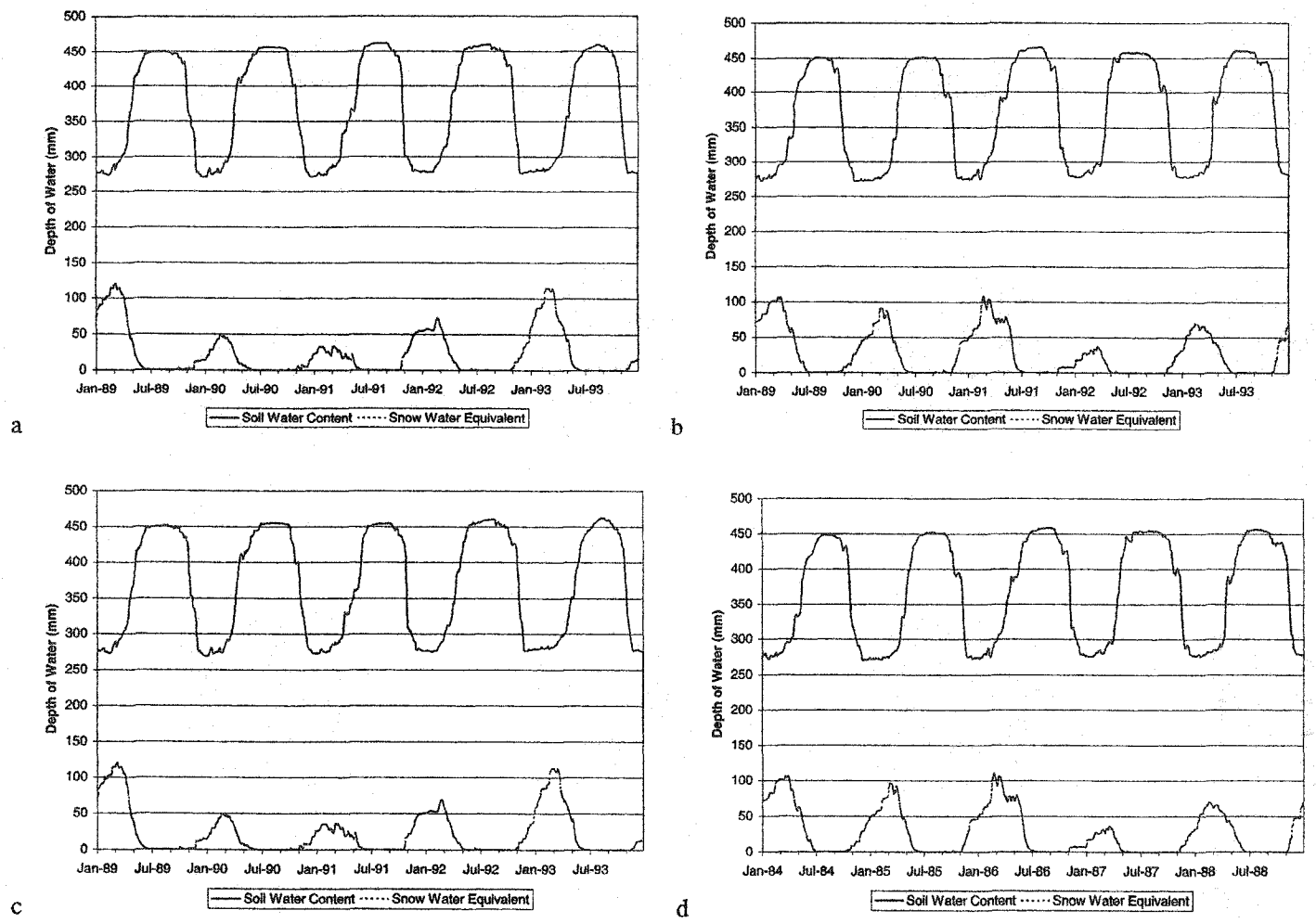


Figure 22: Spatially averaged time series of soil liquid water content and snow water equivalent over the upwind area for a) CTRL, b) MFR, c) VFR, and d) BFR scenarios.

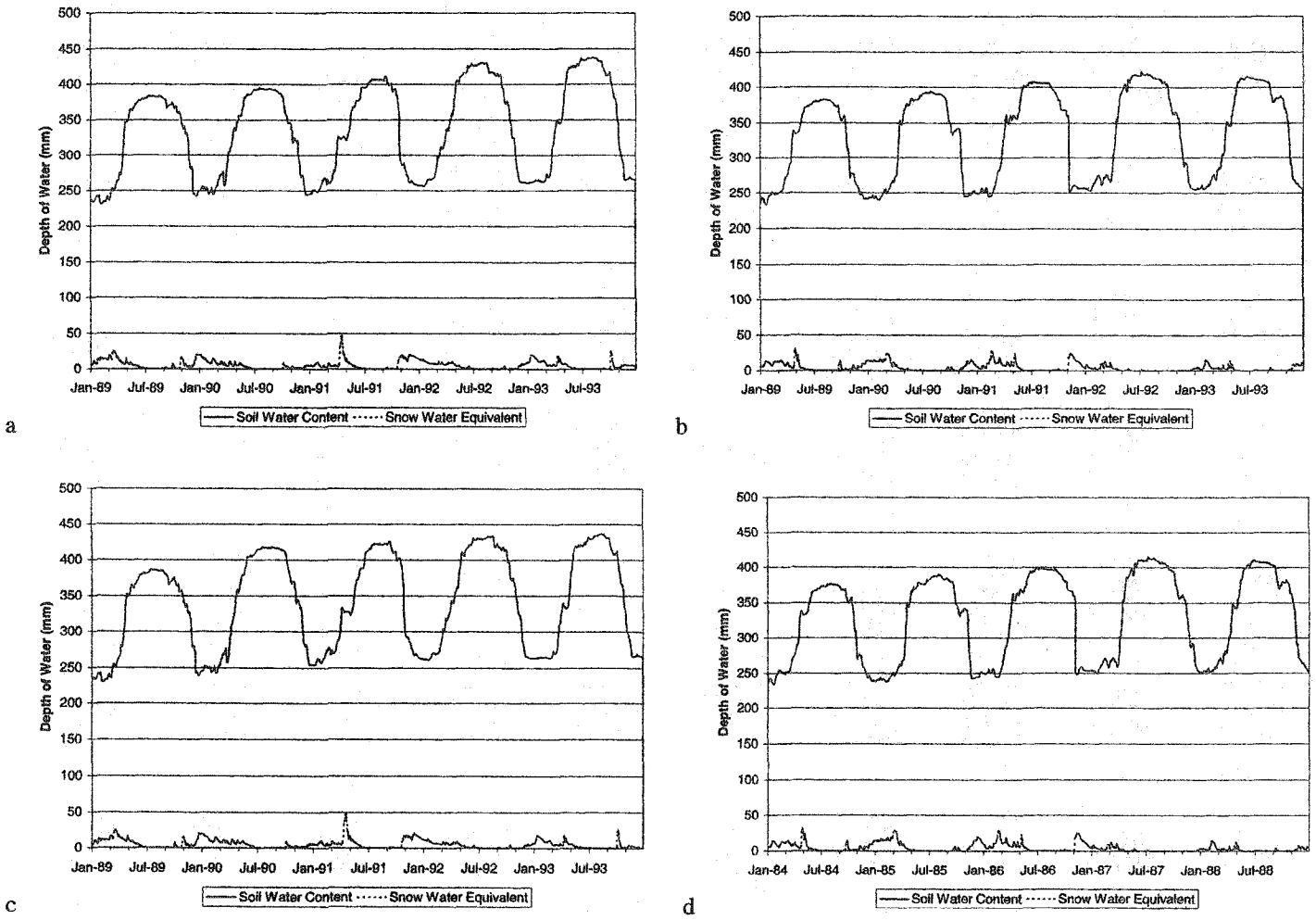


Figure 23: Spatially averaged time series of soil liquid water content and snow water equivalent over the downwind area for a) CTRL, b) MFR, c) VFR, and d) BFR scenarios.

4.3 Diurnal Averages

In addition to the time series of spatially averaged variables described above, diurnal averages also have been produced on both monthly and annual bases. As with the time series, these data have been spatially averaged over the burn, upwind, and downwind areas. Presented in this section are annual diurnal averages of surface and canopy temperatures, as well as diurnal averages of the surface energy budget components for the month of August.

4.3.1 Surface and canopy temperature

Figures 24-26 present diurnally averaged surface and canopy temperatures produced by averaging these fluxes by hour of day over the entire 5-year post-fire time period. Surface temperature is the top soil layer temperature in the absence of snow cover, or the top snow layer temperature when snow cover is present. Canopy temperature is the model-calculated leaf temperature. Surface temperatures generally reach their maximum values around 1400 LST, with minima occurring near 0800 LST. This very closely matches idealized surface temperature diurnal cycles (e.g. Oke, 1987) where maxima lag peak insolation by roughly two hours and minima tend to coincide with early morning air temperature minima. Canopy temperature minima and maxima in figures 24-26 occur slightly ahead of their surface temperature counterparts. This is due to a lack of energy storage capability in the modeled canopy causing temperatures to more closely coincide with insolation and air temperature

peaks and troughs. The lack of storage also results in a larger amplitude diurnal wave for the canopy temperatures relative to surface temperatures.

With the exception of the upwind area MFR-CTRL and BFR-CTRL cases, intercomparison of model runs show small average and RMS differences for surface temperature. Canopy temperature differences are generally larger, although still relatively small (table 9). The larger canopy temperature differences are most likely another consequence of zero heat storage within the model canopy, whereas heat storage within the soil column helps attenuate variations in surface temperature resulting from disparate model forcing scenarios.

Table 9: Average and RMS differences in diurnally averaged surface and canopy temperatures for the various model scenarios.

		Surface Temperature (K)		Canopy Temperature (K)	
		Avg. Diff.	RMS Diff.*	Avg. Diff.	RMS Diff.*
Burn	VFR-CTRL	0.55	0.30	-0.60	1.31
	MFR-CTRL	-0.03	0.18	-1.30	1.14
	BFR-CTRL	0.65	0.37	-0.67	1.56
Upwind	VFR-CTRL	0.01	0.05	-0.10	0.06
	MFR-CTRL	-0.58	0.17	-1.03	0.30
	BFR-CTRL	-0.49	0.24	-0.60	0.16
Downwind	VFR-CTRL	0.03	0.03	-0.65	0.66
	MFR-CTRL	0.26	0.19	-0.59	0.88
	BFR-CTRL	0.43	0.25	-0.33	0.71

* RMS differences after removal of the mean difference.

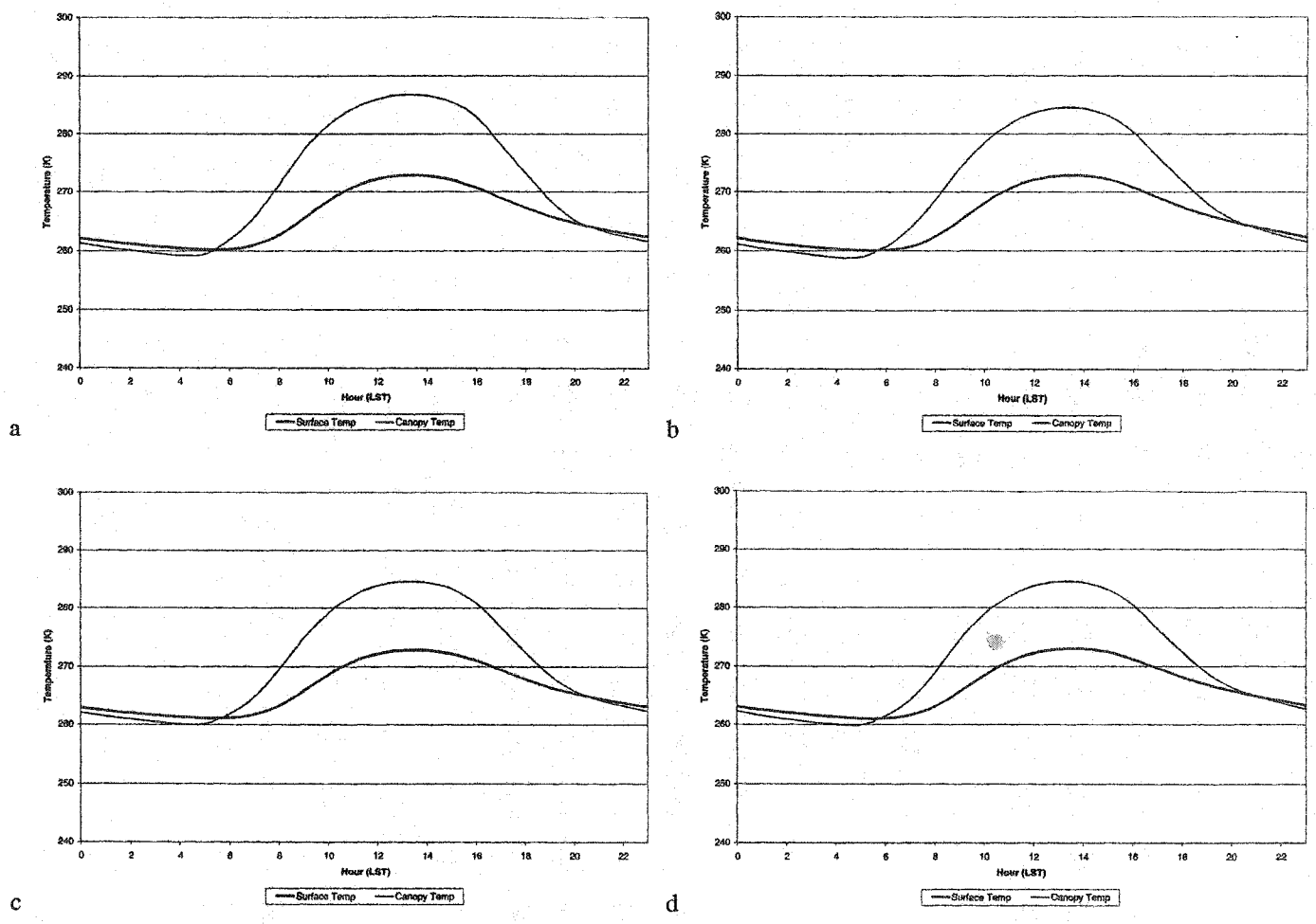


Figure 24: Diurnally averaged surface and canopy temperatures over the burn area for a) CTRL, b) MFR, c) VFR, and d) BFR scenarios.

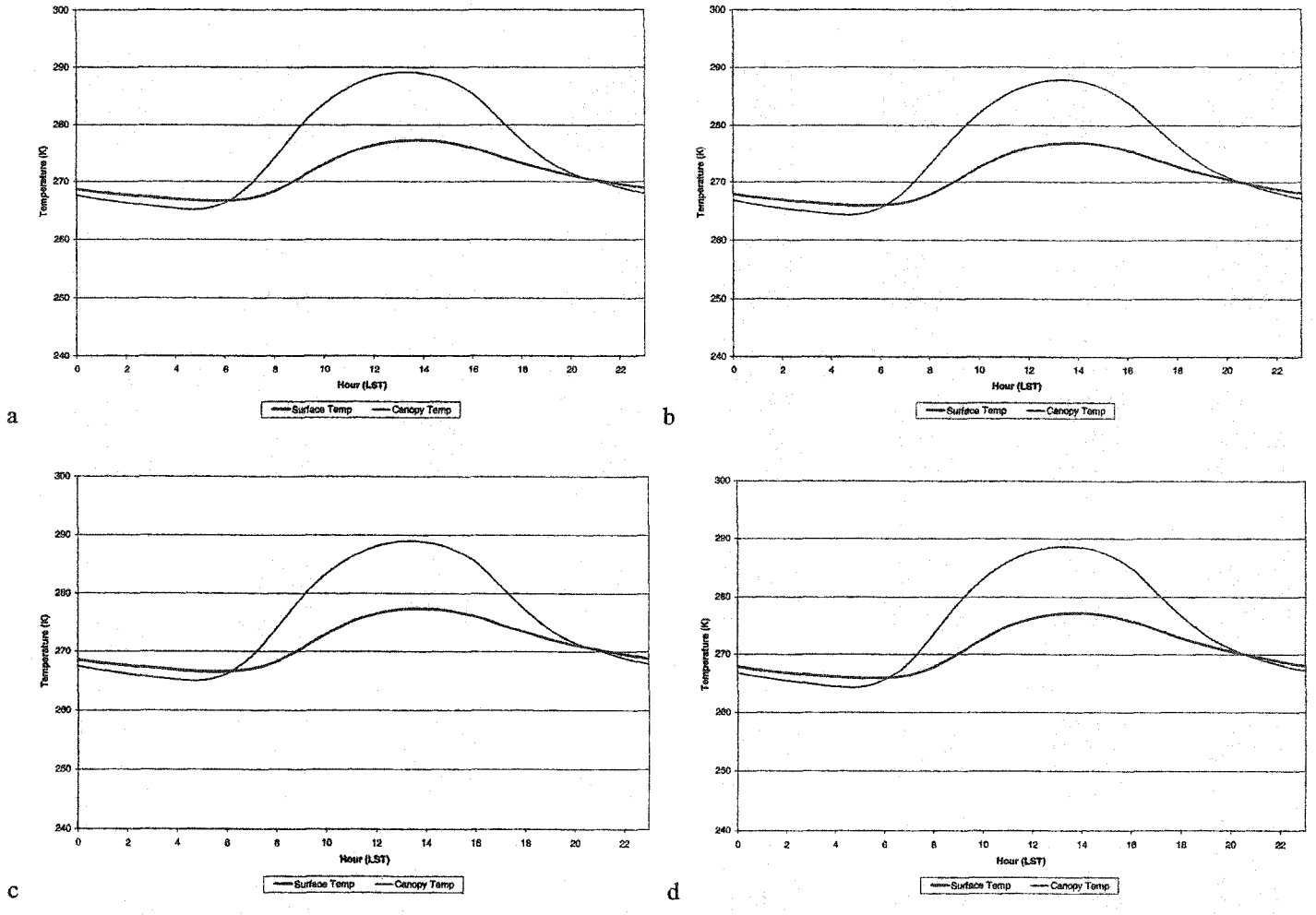


Figure 25: Diurnally averaged surface and canopy temperatures over the upwind area for a) CTRL, b) MFR, c) VFR, and d) BFR scenarios.

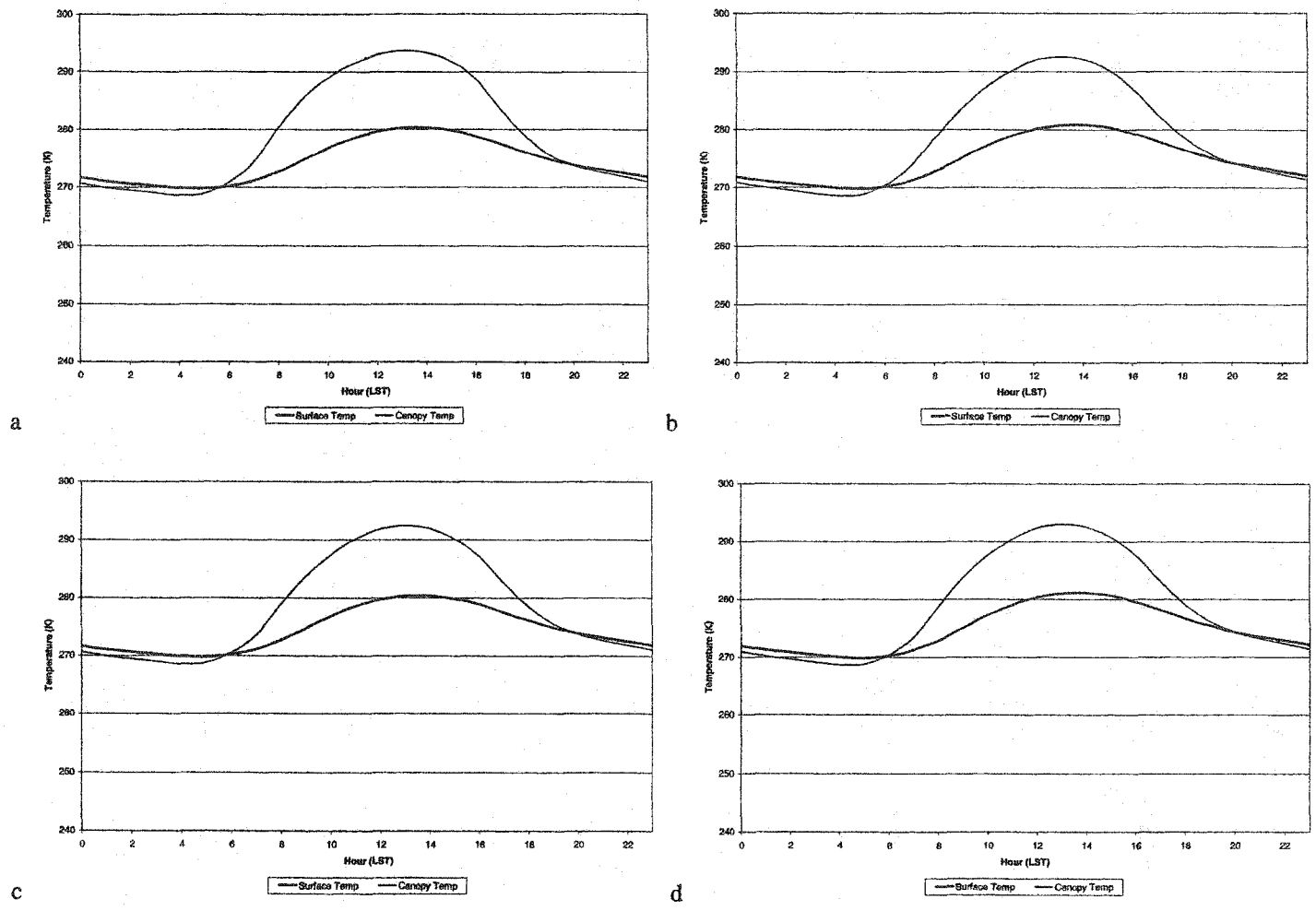


Figure 26: Diurnally averaged surface and canopy temperatures over the downwind area for a) CTRL, b) MFR, c) VFR, and d) BFR scenarios.

The MFR and BFR simulations generally resulted in lower canopy and surface temperatures than the control scenario. This reflects the fact that, spatially averaged over the entire model domain, input solar insolation was 1.2 $MJday^{-1}$ higher during the 1989-1993 post-fire period than during the 1984-1988 pre-fire period, an increase of 16%. It should be noted that this large increase in solar insolation is not found in comparing pre-fire versus post-fire values from the four stations in the GYA at which solar radiation is measured. Thus, the increase may be an artifact of the Bristow and Campbell (1984) method used to model solar radiation, and occurred in spite of an average increase in annual precipitation of 21 mm (6%) following the fires. Consequently, even though the modeled post-fire period had more precipitation, it also had more downwelling solar radiation leading to warmer canopy and surface temperatures. By repeating the meteorological forcing in the MFR and BFR scenarios, this increase in insolation was not realized and canopy and surface temperatures remained relatively cool.

While the MFR and BFR simulations lead to general decreases in canopy and surface temperatures, the timing of maximum and minimum values was not significantly altered. This is true for all three subset areas and each of the four model scenarios, indicating that although solar insolation was substantially higher for the post-fire period than the pre-fire period, the increase in radiation does not seem to have preferentially occurred during a specific portion of the day.

4.3.2 Surface energy budget variables

Diurnally averaged surface energy budget variables for the month of August are presented in figures 27-29. These August diurnal averages are similar to diurnal averages for the entire post-fire time period, however differences between model scenarios are more easily seen due to the larger magnitude of the fluxes during the summer months. As was noted in section 4.2.2 and will be discussed further in the next section, integrated values of the ground heat flux are consistently positive, while those of the sensible heat flux are negative. Since solar noon occurs at approximately 1230 for the GYA in August, peak net radiation is seen in figures 27-29 to occur slightly after 1200 LST. Peak latent heat flux values occur around 1400 LST, corresponding to the previously discussed maxima in surface and canopy temperatures. Peaks in ground heat flux precede those of net radiation by roughly two hours, when the rate of change of soil temperature is the greatest. Sensible heat fluxes, however, do not follow the commonly observed diurnal cycle resembling that of the latent heat fluxes. Instead, maxima within the upwind and burn areas occur near 0800 LST and minima occur at approximately 1800 LST. The downwind area demonstrates a substantially different diurnal sensible heat flux curve with a broad maximum near 1200 LST.

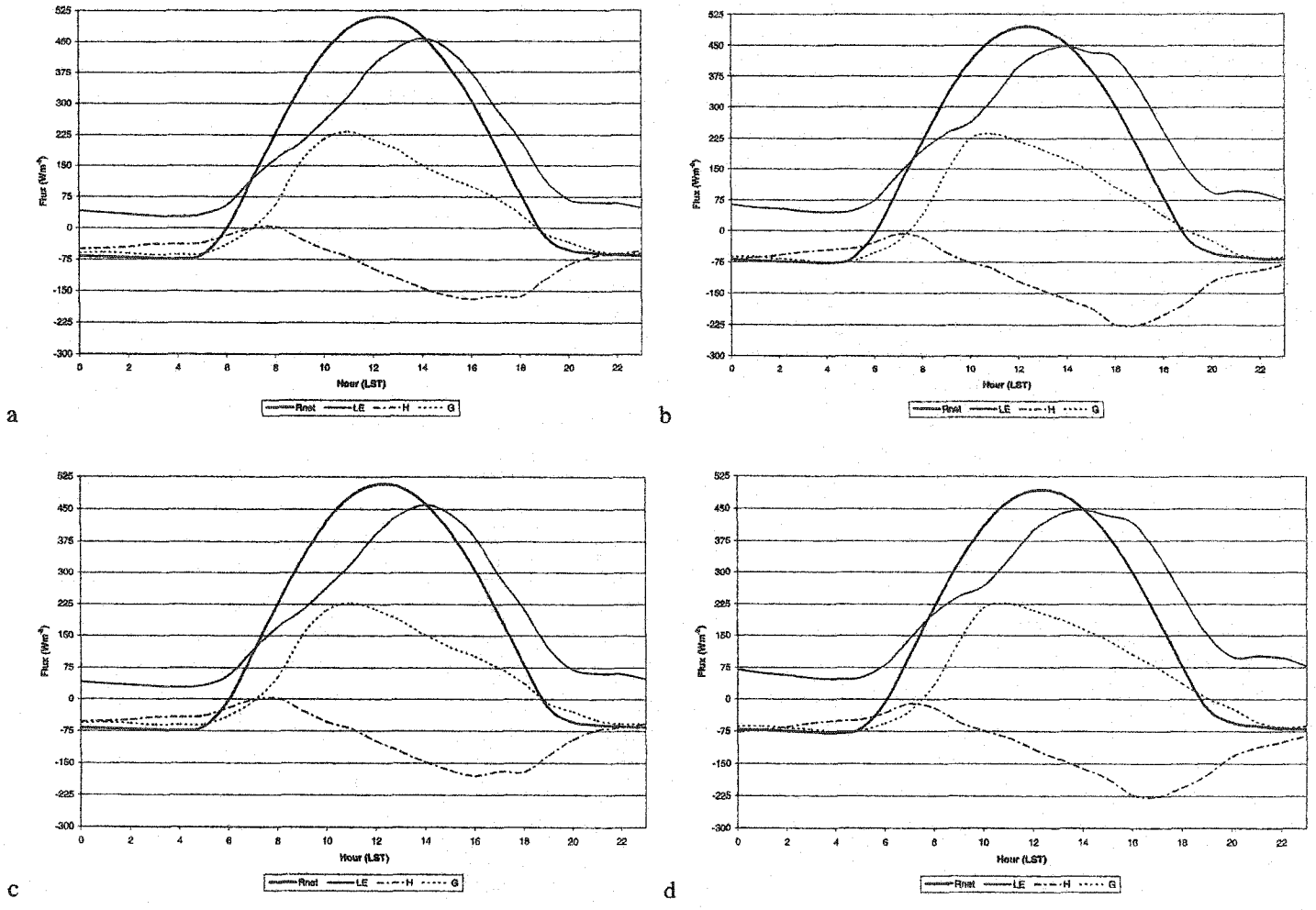


Figure 27: Diurnally averaged surface energy budget variables for the month of August over the burn area for a) CTRL, b) MFR, c) VFR, and d) BFR scenarios.

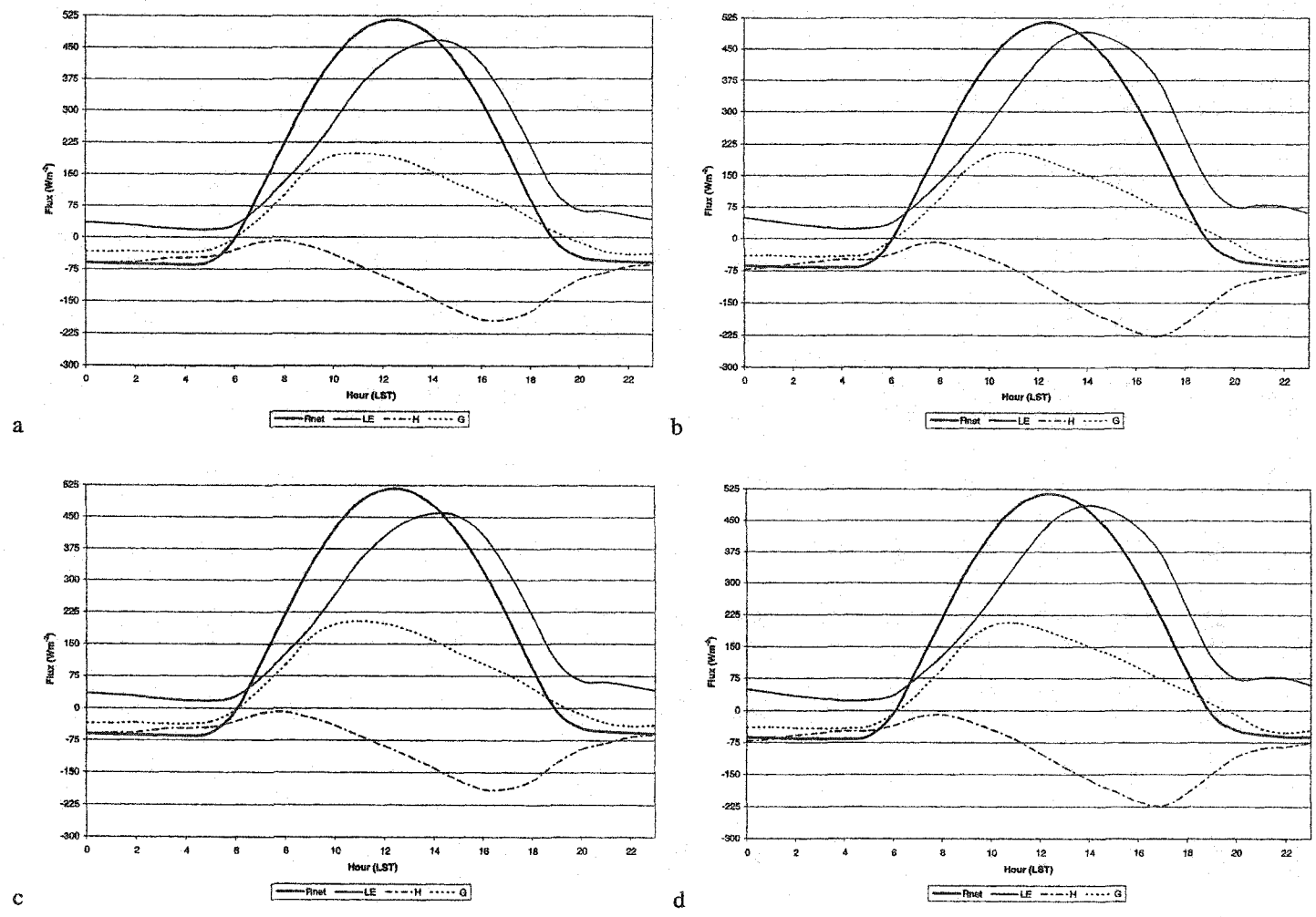


Figure 28: Diurnally averaged surface energy budget variables for the month of August over the upwind area for a) CTRL, b) MFR, c) VFR, and d) BFR scenarios.

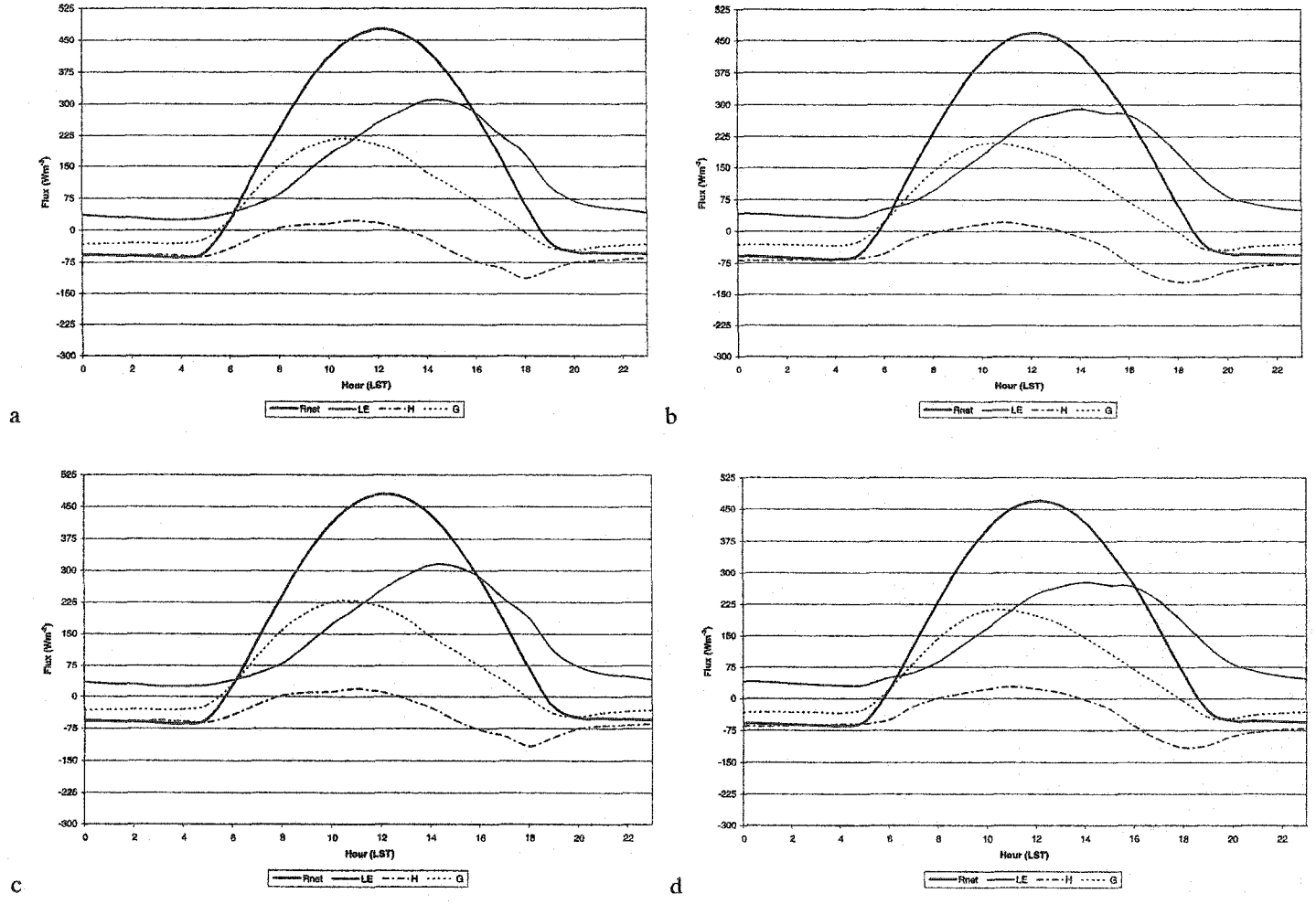


Figure 29: Diurnally averaged surface energy budget variables for the month of August over the downwind area for a) CTRL, b) MFR, c) VFR, and d) BFR scenarios.

Table 10 shows the surface energy budget average and RMS differences between annual diurnally averaged output from the CTRL model run and the other three scenarios for the upwind, downwind, and burn areas. Differences are small for all three comparisons over the downwind area, while differences in the upwind area are considerably larger for the MFR-CTRL and BFR-CTRL comparisons than for the VFR-CTRL comparison. The burn area demonstrates similar differences between the VFR-CTRL and the MFR-CTRL comparisons, but much larger differences are seen for turbulent fluxes in the BFR-CTRL comparison. This was seen previously in comparing the spatially averaged turbulent flux time series (section 4.2.2). In general, repeating of model forcings had a larger impact over the burn area than the other two areas. Timing of flux minima and maxima was mostly unaffected by repeating model forcings.

Table 10: Average and RMS differences in annual diurnally averaged surface energy budget components for the various model scenarios.

		Net Radiation (Wm^{-2})		Latent Heat Flux (Wm^{-2})		Sensible Heat Flux (Wm^{-2})		Ground Heat Flux (Wm^{-2})	
		Avg. Diff.	RMS Diff.*	Avg. Diff.	RMS Diff.*	Avg. Diff.	RMS Diff.*	Avg. Diff.	RMS Diff.*
Burn	VFR-CTRL	0.22	3.88	8.54	7.29	-7.59	2.96	-0.73	2.54
	MFR-CTRL	-0.38	3.32	12.39	3.75	-7.95	3.30	-4.82	2.27
	BFR-CTRL	0.17	7.47	23.51	9.20	-16.28	6.76	-7.05	2.48
Upwind	VFR-CTRL	0.26	0.18	-0.91	0.69	0.63	0.73	0.55	1.24
	MFR-CTRL	-1.99	0.89	4.50	2.10	-2.95	1.79	-3.55	0.90
	BFR-CTRL	-1.75	1.21	2.85	2.71	-2.04	1.41	-2.58	1.22
Downwind	VFR-CTRL	0.48	0.40	0.75	1.45	-1.97	2.31	1.70	2.44
	MFR-CTRL	-1.06	1.13	5.23	2.11	-4.52	2.86	-1.75	2.00
	BFR-CTRL	-0.67	1.18	3.69	2.86	-3.18	3.01	-1.18	1.51

* RMS differences after removal of the mean difference.

4.4 Discussion of Results

In examining time series and diurnal averages of surface energy budget variables, soil liquid water content, and snow water equivalent over the upwind and downwind areas for the VFR scenario it becomes apparent that unassociated vegetation changes had relatively small effects. Conversely, the fire-associated vegetation changes occurring in the burn area are considerably larger. Generally, removal of vegetation by the 1988 fires caused increases in sensible heat flux with comparable decreases in latent heat flux. This increase in the Bowen ratio occurred in spite of slightly cooler surface temperatures and increased snow water equivalent.

Unlike the unassociated vegetation changes, unassociated climate changes, illustrated over the upwind area in the MFR scenario, had a noticeable impact on turbulent fluxes, surface temperatures, and snow water equivalent. This is not particularly surprising since substantial climate differences between the pre-fire and post-fire periods would not be unusual due to both random and deterministic causes. Vegetation changes outside the burn area, however, would likely be relatively small, and thus have little impact on the variables examined. Unassociated climate changes resulted in somewhat decreased latent heat flux, increased sensible heat flux, warmer surface temperatures, and reduced snow water equivalent.

In the burn area, and to a lesser extent in the downwind area, the MFR scenario revealed fire climate changes resulting in a reduction of latent heat flux and increase in sensible heat flux considerably larger than those changes seen in the upwind area. Also, snow water equivalent was increased in the burn and downwind areas after the fires, contrary to the decrease seen in the upwind area. It is interesting to note that the increase in snow water equivalent seems contradictory to the increased Bowen ratio observed in the burn and downwind areas.

The combined effects of vegetation and climate changes are elucidated in comparing the BFR simulation to the control model run. Here, the greatest impact is over the burn area where both fire-associated and unassociated changes are realized. Latent heat flux is considerably reduced, while sensible heat flux is increased as a consequence of post-fire changes in vegetation and climate. Also, snow water equivalent is substantially increased. Average differences in surface energy budget variables and snow water equivalent are generally smaller for the upwind and downwind areas where fire-associated vegetation changes are not realized. However, slightly larger differences in turbulent heat fluxes are realized in the downwind area than the upwind area, indicating that fire-associated climate changes advected over the downwind area may act to amplify differences induced by the unassociated climate and vegetation changes in this area.

While the sizeable differences in surface energy budget variables and snow water equivalent attributable to fire-induced vegetation changes are of considerable interest,

it is important at this point to comment on the limitations and possible sources of error in this study. As with any model results, caution must be exercised in attributing differences in output to physical causes, when these differences may actually arise from purely numerical origins. This especially needs to be considered here since the snow and frozen soil algorithms newly implemented in the SHEELS model have not been tested against observations. Model input fields and parameters may also lead to erroneous results.

For example, the persistently negative sensible heat flux and positive ground heat flux values mentioned in section 4.2.2 may be a consequence of initial bottom soil layer temperatures being too low. Initialization of temperature within the soil column was accomplished through use of the 10-year mean near-surface air temperature. Attenuation of the annual (and diurnal) temperature wave with soil depth results in a finite level at which the amplitude of the wave becomes negligible, and the temperature approaches a constant value equal to that of the mean surface temperature. Since numerical solution of the heat diffusion equation in SHEELS necessitates the bottom-most soil layer having constant temperature, it thus seems logical to initialize this temperature to the climatological mean near-surface air temperature. This method was employed for modeling of the GYA, with the exception that bottom soil layer temperatures were initialized at a value of 0.5 °C in lieu of the mean near-surface air temperature in instances where the mean was less than 0.5 °C. This prevented a permanently frozen bottom soil layer. Resulting bottom soil layer temperatures are depicted in figure 30.

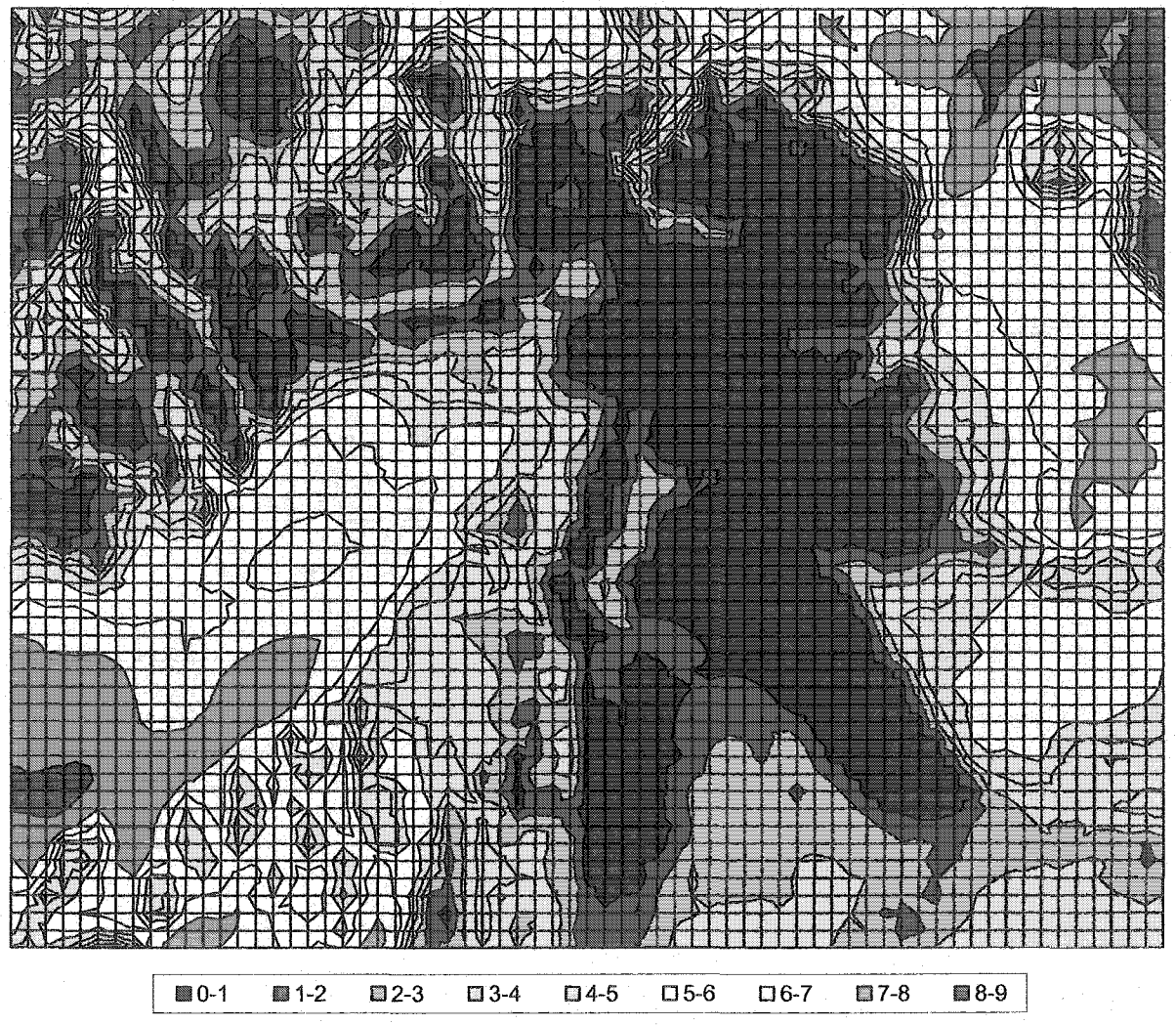


Figure 30: Map of initial bottom soil layer temperatures (°C).

Top soil layer temperature was initialized to the near-surface air temperature of the first time step (midnight, January 1, 1984). Initial temperatures of the remaining soil layers were computed by linear interpolation between the top and bottom layer temperatures based on each layer's depth.

In retrospect, the insulating qualities of the snowpack act to reduce the influence of cold wintertime near-surface air temperatures on the deep soil temperature. Thus, the climatological mean near-surface air temperature should be lower than the actual deep soil temperature. By using the climatological mean to initialize the bottom-most soil layer temperature, which then does not change throughout the model time period, the soil column tends to remain excessively cold, with consequent high ground heat fluxes and persistent negative sensible heat fluxes.

This problem is especially noticeable in the burn area (e.g. figure 27). As would be expected, mean near-surface air temperature is lowest in high-elevation regions, and these are also the areas of greatest snowfall. Average bottom soil layer temperature within the burn area is 0.73 °C, as compared to averages of 4.41 °C and 6.06 °C in the upwind and downwind areas, respectively. Furthermore, as previously discussed, comparison of figures 21-23 reveals that snowpack depths are significantly greater in the burned area than the upwind and downwind areas, which would result in greater thermal insulation of the soil column during winter months and a larger discrepancy between the prescribed and actual temperatures of the bottom-most soil layer.

Also affecting soil column temperatures is the total depth of the column. The depth to the bottom of the soil column was selected from a hydrologic perspective, namely the average depth to impermeable bedrock in the GYA. The consequent total soil column thickness of 1.10 m is likely not deep enough to have negligible annual temperature changes justifying the constant bottom soil layer temperature within the SHEELS model. Oke (1987), for example, reports that the annual temperature wave in some soils may extend to a depth of 14 m. Clearly, this necessitates additional model soil layers that are thermally active, even if not hydrologically active.

5 Summary

The vast geographic scale of the 1988 Yellowstone fires provides a unique opportunity for research on the climatological, hydrological, and ecological impacts of wildland fire. While many scientists already have taken advantage of this opportunity, little prior research has been done to quantify the effects of fire-induced land cover change on long-term surface energy budget, snow water equivalent, and soil moisture values, either in the GYA or elsewhere. However, altered climatologies of these variables could have far-reaching implications, and the possibility that fire-induced land cover changes can bring about such alterations has been examined in this study.

Meteorological observations spanning the 10-year period of 1984-1993 have been collected from 178 stations within the GYA. The meteorological data were quality assured using range, step, and spatial tests before being interpolated to an 8-km spatial grid and 1-hour temporal resolution. Elevation-based corrections were applied to temperature and atmospheric pressure observations, and the spatially sparse observations of downwelling solar radiation were supplemented with values modeled on the basis of diurnal temperature range. Downwelling longwave radiation fields were modeled, as well. Ultimately, a quality assured meteorological dataset was produced, comprising hourly data for seven variables: near-surface air temperature, relative humidity, precipitation, wind speed, atmospheric pressure, and downwelling

solar and longwave radiation. This dataset was then used in conjunction with vegetation, orographic, and soil data to run the SHEELS land-atmosphere model.

Uses of the meteorological dataset described above are not limited to SHEELS model input. The gridded, quality-assured data are ideal for use as input for a wide range of numerical models, including other land-atmosphere models, hydrologic models, and ecological models. Studies of regional and local-scale climate within the GYA are also possible with the meteorological dataset. Such studies are made more feasible by the format uniformity, quality assurance, and aggregation of data from a variety of observation networks.

In addition to amassing the meteorological and topographic inputs required for modeling land-atmosphere processes in the GYA, considerable modification of the SHEELS model was necessary to facilitate its use in this high elevation, mid-latitude region. Explicit modeling of snow and frozen soil processes was accomplished through addition of snow layers to the model, inclusion of the thermal effects of water phase changes in soil and snow layer temperature calculations, and reduction of hydraulic conductivity during periods of frozen soil. Inclusion of snow within the model also dramatically affects surface albedo, with snow albedo estimated as a function of snow age and solar zenith angle.

While implementation of the new snow and frozen soil algorithms within SHEELS was undertaken specifically for this research, these algorithms are in no way specific

to use in the GYA. As such, this work has considerably expanded the geographic range over which the SHEELS model may be used. While numerical models exist that have been designed specifically for simulation of snow temperature, accumulation, and melt, these do not model turbulent fluxes over snow cover or soil-atmosphere water and energy exchanges in the absence of snow. Also, vegetation is generally not included and soil moisture and temperature profiles are not explicitly modeled. Examples of these types of models include SNTHERM (Jordan, 1991) and CROCUS (Brun et al., 1989).

Conversely, most land-atmosphere models treat snow in a highly parameterized fashion that may negatively influence modeled results. For instance, snow within the BATS model is thermally indistinct from the soil column (Yang et al., 1997). This arises from soil-snow temperature determination based on the force-restore method, as opposed to solution of the heat diffusion equation, and results in an inability for snow to be melted by upward heat flux from a warmer underlying soil. Similar use of the force-restore method of temperature estimation is found in the Simplified Simple Biosphere (SSiB) model (Xue et al., 1991).

SHEELS, with its new snow and frozen soil algorithms, provides an alternative land-atmosphere model for use in regions prone to snowfall. Simulation of snow within SHEELS is not as complex as in some snow-specific models, but does provide a more physically realistic treatment than most land-atmosphere models currently in use. In addition to providing another methodology for modeling land-atmosphere processes,

this also creates opportunities to study the efficacy of parameterizations used in less complex models.

6 Conclusions and Recommendations for Future Research

6.1 Conclusions

Simulation of surface energy budget variables, soil water content, and snow water equivalent over the GYA utilizing the meteorological inputs and new model algorithms described above yielded an array of interesting results. Removal of vegetation over the burn area lead to a higher Bowen ratio, cooler surface temperatures, and an increase in snow water equivalent following the 1988 fires. Such effects were not seen in the upwind and downwind areas, indicating that these changes were brought about by the fire-induced vegetation changes over the burn area, not changes in pre-fire versus post-fire climate. Soil moisture, however, was largely unaffected by the vegetation changes.

Climate changes not associated with the 1988 fires were also seen to have substantial impacts, increasing the Bowen ratio, increasing surface temperatures, and decreasing snow water equivalent. However, in the burn area and, to a lesser extent, in the downwind area, the Bowen ratio was increased beyond that seen in the upwind area, and snow water equivalent was also increased following the fires. This would seem to indicate that regional climate was, in fact, affected by the fires, and some of the effects may have been advected over the downwind area.

These results must be viewed with some degree of caution, however, since they are derived from model simulations, not direct observations. This is especially true in light of the fact that the new snow and frozen soil algorithms in SHEELS have not yet been verified against observations. Also, initialization of soil temperature and thickness of the thermally active soil zone may be problematic in these comparisons, which could affect results.

Unfortunately, the temporally and spatially averaged comparisons presented here do not easily lend themselves to a statistical analysis of their significance. However, the substantial increases in Bowen ratio resulting from both the fire-associated vegetation changes and the fire-associated climate changes could have important consequences. Impacts of the fires were not only seen in the burned areas, but also downwind from these areas. If further studies prove such alterations to be a common outcome of wildland fires, the role of such fires in shaping regional climate can be addressed for purposes of water resource management, ecosystem sustainability, and fire suppression policy.

6.2 Future Research Opportunities

The work presented here opens up opportunities for a considerable array of further studies. Clearly, there is a need for testing of the new snow and frozen soil algorithms in the SHEELS model. Snow depth measurements from COOP stations within the GYA and observations of snow water equivalent from SNOTEL sites were

quality assured during assembly of the SHEELS meteorological inputs described in chapter 2. These data provide an obvious means of assessing the performance of the new model algorithms through comparison of modeled versus observed snow depth and snow water equivalent over a multi-year time span.

Also demonstrated in this research is the need for a deeper soil column to account for the large annual temperature range encountered in the GYA. Addition to the SHEELS model of thermally active soil layers that are not hydrologically active would provide a computationally cost-effective method of obtaining a more physically realistic soil temperature profile. This would, in turn, lead to more realistic simulations of the sensible and ground heat fluxes.

Finally, further studies conducted for different regions or for different time periods may be undertaken using methodologies similar to those presented here. It is only through numerous such studies that an accurate understanding of the typical effects of wildland fires on surface energy budget components and soil moisture may be achieved.

7 References

Agbu, P. A., and James, M. E., 1994. *The NOAA/NASA Pathfinder AVHRR Land Data Set User's Manual.* Greenbelt Maryland: Goddard Distributed Active Archive Center, NASA, Goddard Space Flight Center.

Allen, C. D., Savage, M., Falk, D. A., Suckling, K. F., Swetnam, T. W., Schulke, T., Stacey, P. B., Morgan, P., Hoffman, M., and Klingel, J. T., 2002. Ecological restoration of southwestern ponderosa pine ecosystems: A broad perspective. *Ecological Applications*, **12**:1418-1433.

Anderson, E. A. and Crawford, N. H. 1964. *The Synthesis of Continuous Snowmelt Runoff Hydrographs on a Digital Computer.* Tech. Report 36. Stanford, California: Stanford University Department of Civil Engineering.

Andreae, M. O., 1993. The influence of tropical biomass burning on climate and the atmospheric environment. In: *Biogeochemistry of Global Change: Radiatively Active Trace Gases*. Oremland, R. S., ed. New York: Chapman & Hall.

Balling, R. C., Meyer, G. A., and Wells, S. G., 1992. Climate change in Yellowstone National Park: Is the drought-related risk of wildfires increasing? *Climatic Change*, **22**:35-46.

Barnes, S. L., 1964. A technique for maximizing details in numerical weather map analysis. *Journal of Applied Meteorology*, **3**:396-409.

Barnes, S. L., 1973. *Mesoscale objective analysis using weighted time-series observations.* NOAA Technical Memo ERL NSSL-62. National Severe Storms Laboratory, Norman, Oklahoma. 60 pp.

Bedient, P. B. and Huber, W. C., 2002. *Hydrology and Flood Plain Analysis*. 3rd ed. Upper Saddle River, New Jersey: Prentice Hall. 763 pp.

Boone, A. and Etchevers, P., 2001. An intercomparison of three snow schemes of varying complexity coupled to the same land surface model: Local-scale evaluation at an alpine site. *Journal of Hydrometeorology*, **2**:374-394.

Bras, R. L. 1990. *Hydrology: An Introduction to Hydrologic Science*. New York: Addison-Wesley.

Bristow, K. L. and Campbell, G. S., 1984. On the relationship between incoming solar radiation and the daily maximum and minimum temperature. *Agricultural and Forest Meteorology*, **31**:159-166.

Brooks, R. H. and Corey, A. T., 1964. Hydraulic properties of porous media. *Hydrology Paper 3*, Colorado State University, Fort Collins, Colorado.

Brun, E., Martin, E., Simon, V., Gendre, C., and Coleou, C., 1989. An energy and mass balance model of snow cover suitable for operational avalanche forecasting. *Journal of Glaciology*, **35**:333-342.

Brutsaert, W., 1975. On a derivable formula for long-wave radiation from clear skies. *Water Resources Research*, **11**:742-744.

Capehart, W. J. and Carlson, T. N., 1994. Estimating near-surface soil moisture availability using a meteorologically driven soil-water profile model. *Journal of Hydrology*, **160**:1-20.

Charney, J. G., 1975. Dynamics of deserts and drought in the Sahel. *Quarterly Journal of the Royal Meteorological Society*, **101**:193-202.

Christensen, N. L. and 12 others, 1989. Interpreting the Yellowstone fires of 1988. *Bioscience*, **39**:678-685.

Clapp, R. B. and Hornberger, G. M., 1978. Empirical equations for some soil hydraulic properties. *Water Resources Research*, **14**:601-604.

COESA, 1976. *U.S. Standard Atmosphere, 1976*. Washington, DC: U.S. Government Printing Office.

Crawford, T. M. and Duchon, C. E., 1999. An improved parameterization for estimating effective atmospheric emissivity for use in calculating daytime downwelling longwave radiation. *Journal of Applied Meteorology*, **38**:474-480.

Cressman, G. P., 1959. An operational objective analysis system. *Monthly Weather Review*, **87**:367-374.

Crosson, W. L., Smith, E. A., and Cooper, H. J., 1993. Estimation of surface heat and moisture fluxes over a prairie grassland. Part IV: Impact of satellite remote sensing of slow canopy variables on performance of a hybrid biosphere model. *Journal of Geophysical Research*, **98**:4979-4999.

Davis, L., 2001. *State Soil Geographic (STATSGO) Data Base*. Available from: <http://www.ftw.nrcs.usda.gov/statsgo.html>.

DeBano, L. F., 1981. *Water repelent soils: A state-of-the-art*. USDA Forest Service General Technical Report PSW-46. Washington, DC: U.S. Government Printing Office.

Deeming, J. E., Burgan, R. E., and Cohen, J. D., 1977. *The National Fire-Danger Rating System - 1978*. General Technical Report INT-39. Ogden, Utah: U.S. Department of Agriculture, U.S. Forest Service, Intermountain Forest and Range Experiment Station. 66 pp.

Dickinson, R. E., Henderson-Sellers, A., and Kennedy, P. J., 1993. *Biosphere-Atmosphere Transfer Scheme (BATS) Version 1e as coupled to the NCAR Community Climate Model.* NCAR Technical Note NCAR/TN-387+STR. National Center for Atmospheric Research, Boulder, Colorado. 72 pp.

DiMego, G. J., 1988. The National Meteorological Center Regional Analysis System. *Monthly Weather Review*, **116**:977-1000.

Dirks, R. A. and Martner, B. E., 1982. *The Climate of Yellowstone and Grand Teton National Parks*. National Park Service occasional paper number six. Washington, DC: U. S. Government Printing Office.

Dirmeyer, P. A., 1994. Vegetation stress as a feedback mechanism in midlatitude drought. *Journal of Climate*, **7**:1463-1483.

Ewing, R., 1996. Postfire suspended sediment from Yellowstone National Park, Wyoming. *Journal of the American Water Resources Association*, **32**:605-627.

Federer, C. A., 1982. Transpirational supply and demand: plant, soil, and atmospheric effects evaluated by simulation. *Water Resources Research*, **18**: 355-362.

Franke, M. A., 2000. *Yellowstone in the afterglow: Lessons from the fires*. YCR–NR–2000–03. Mammoth Hot Springs, Wyoming: Yellowstone Center for Resources, Yellowstone National Park. 118 pp.

Gillies, R. R., Carlson, T. N., Cui, J., Kustas, W. P., and Humes, K. S., 1997. A verification of the `triangle' method for obtaining surface soil water content and energy fluxes from remote measurements of the Normalized Difference Vegetation Index (NDVI) and surface radiant temperature. *International Journal of Remote Sensing*, **18**:3145-3166.

Goldammer, J. G. and Price, C., 1998. Potential impacts of climate change on fire regimes in the tropics based on MAGICC and a GISS GCM-derived lightning model. *Climatic Change*, **39**:273-296.

Hale, R. C. and Duchon, C. E., 2003. Use of AVHRR-derived surface temperatures in evaluating a land-atmosphere model. *International Journal of Remote Sensing*, **24**:4527-4541.

Hansen, M., DeFries, R., Townshend, J. R. G., and Sohlberg, R., 2000. Global land cover classification at 1 km resolution using a decision tree classifier. *International Journal of Remote Sensing*, **21**: 1331-1365.

Horel, J., Splitt, M., Dunn, L., Pechmann, J., White, B., Ciliberti, C., Lazarus, S., Slemmer, J., Zaff, D., and Burks, J., 2002. Mesowest: Cooperative mesonets in the western United States. *Bulletin of the American Meteorological Society*, **83**:211-225.

Huete, A. R., 1988. A soil-adjusted vegetation index (SAVI). *Remote Sensing of Environment*, **25**: 295-309.

Jarvis, P. G., 1976. The interpretation of the variations in leaf water potential and stomatal conductance found in canopies in the field. *Philosophical Transactions of the Royal Society of London, Biological Sciences*, **273**:593-610.

Jordan, R. 1991. *A one-dimensional temperature model for a snow cover: Technical documentation for SNTHERM.89*. Special Report 91-16. Hanover, New Hampshire: U. S. Army Cold Regions Research and Engineering Laboratory.

Knowles, J. B., 1993. *The Influence of Forest Fire Induced Albedo Differences on the Generation of Mesoscale Circulations*. M.S. thesis, Colorado State University, Fort Collins, Colorado.

Koch, S. E., desJardin, M., and Kocin, P. J., 1983. An interactive Barnes objective map analysis scheme for use with satellite and conventional data. *Journal of Climate and Applied Meteorology*, **22**:1487-1503.

Koster, R. D., Suarez, M. J., and Heiser, M., 2000. Variance and predictability of precipitation at seasonal-to-interannual timescales. *Journal of Hydrometeorology*, **1**:26-46.

Langham, E. J., 1981. Physics and properties of snowcover. In: *Handbook of Snow: Principles, Processes, Management and Use*. Gray, D. M. and Male, D. H., eds. New York: Pergamon Press.

Lathrop, R. G., 1994. Impacts of the 1988 wildfires on the water quality of Yellowstone and Lewis Lakes, Wyoming. *International Journal of Wildland Fire*, **4**:169-175.

Lee, R., 1964. Potential insolation as a topoclimatic characteristic of drainage basins. *Bulletin of the International Association of Scientific Hydrology*, **9**:27-41.

Leopold, A. S., Cain, S. A., Cottam, C. M., Gabrielson, I. N., and Kimball, T. L., 1963. Wildlife management in the national parks. *Transactions of the North American Wildlife and Natural Resources Conference*, **24**:28-45.

Leprieur, C., Verstraete, M. M., and Pinty, B., 1994. Evaluation of the performance of various vegetation indices to retrieve vegetation cover from AVHRR data. *Remote Sensing Reviews*, **10**: 265-284.

Lorenc, A. C., 1981. A global three-dimensional multivariate statistical interpolation scheme. *Monthly Weather Review*, **109**:701-721.

Lotan, J. E., 1975. The role of cone serotiny in lodgepole pine forests. In: *Management of Lodgepole Pine Ecosystems*. Baumgartner, D. M., ed. Pullman, Washington: Washington State University Cooperative Extension Service.

Lundin, L.-C., 1990. Hydraulic properties in an operational model of frozen soil. *Journal of Hydrology*, **118**: 289-310.

Marston, R. A., and Haire, D. H., 1990. Runoff and soil loss following the 1988 Yellowstone fires. *Great Plains-Rocky Mountain Geographical Journal*. **18**:1-8.

Martinez, J. E., 1999. *Sensitivity of water and energy balance to the number of soil layers in a surface flux-hydrology model - Tarrawarra Catchment, Australia.* Thirteenth National Conference on Undergraduate Research, University of Rochester, Rochester, New York, April 8-10.

Martinez, J. E., Duchon, C. E., and Crosson, W. L., 2001. Effect of the number of soil layers on a modeled surface water budget. *Water Resources Research*, **37**:367-377.

McIntyre, M. J., and Minshall, G. W., 1996. Changes in transport and retention of coarse particulate organic matter in streams subject to fire. In: *The Ecological Implications of Fire in Greater Yellowstone: Proceedings of the Second Biennial Conference on the Greater Yellowstone Ecosystem.* Greenlee, J., ed. Fairfield, Washington: International Association of Wildland Fire.

Meyer, G. A. and Wells, S. G., 1997. Fire-related sedimentation events on alluvial fans, Yellowstone National Park. *Journal of Sedimentary Research*, **A67**:776-791.

Meyer, G. A, Wells, S. G., Balling, R. C., and Jull, A. J. T., 1992. Response of alluvial systems to fire and climate change in Yellowstone National Park. *Nature*, **357**:147-150.

Mihuc, T. B. and Minshall, G. W., 1995. Trophic generalists vs. trophic specialists: implications for food web dynamics in post-fire streams. *Ecology*, **76**:2361-2372.

Minshall, G., Royer, T., and Robinson, C., 2001. Response of the Cache Creek macroinvertebrates during the first 10 years following disturbance by the 1988 Yellowstone wildfires. *Canadian Journal of Fisheries and Aquatic Sciences*, **58**:1077-1088.

Myers, T. P. and Dale, R. F., 1983. Predicting daily insolation with hourly cloud height and coverage. *Journal of Climate and Applied Meteorology*, **22**:537-545.

National Interagency Fire Center, 2002. *Wildland Fire Statistics*. Available from: <http://www.nifc.gov/stats/wildlandfirestats.html>.

National Park Service, 1991. *Yellowstone National Park Wildland Fire Management Plan*. Yellowstone National Park, Rocky Mountain Region, National Park Service, Department of the Interior. 65 pp.

NCDC, 2003. *Data Documentation for Data Set 3200 (DSI-3200) Surface Land Daily Cooperative Summary of the Day*. Asheville, North Carolina: National Climatic Data Center. 16 pp.

NWS, 2000. *Cooperative Observer Program (COOP)*. Available from: <http://www.nws.noaa.gov/om/coop/Publications/coop.PDF>.

Nyland, R. D., 1999. Patterns of lodgepole pine regeneration following the 1988 Yellowstone fires. *Forest ecology and management*, **111**:23-34.

Oke, T. R., 1987. *Boundary Layer Climates*. 2nd ed. New York: Methuen. 435 pp.

Pearson, J. A., 1982. *Biomass Distribution and Ecosystem Development in Lodgepole Pine Forests of the Medicine Bow Mountains, Wyoming*. Doctoral dissertation, University of Wyoming, Laramie, Wyoming.

Pearson, S., Turner, M. G., Wallace, L. L., and Romme, W. H., 1995. Winter habitat use by large ungulates following fire in northern Yellowstone National Park. *Ecological Applications*, **5**:744-755.

Piñol, J., Terradas, J., and Lloret, F., 1998. Climate warming, hazard, and wildfire occurrence in coastal eastern Spain. *Climatic Change*, **38**:345-357.

Qi, J., Chehbouni, A., Huete, A. R., Kerr, Y. H., and Sorooshian, S., 1994. A modified soil adjusted vegetation index. *Remote Sensing of Environment*, **48**: 119-126.

Rawls, W. J., 1983. Agricultural management effects on soil water processes part I: Soil water retention and Green and Ampt infiltration parameters. *Transactions of the ASAE*, **26**:1747-1751.

Rawls, W. J. and Brakensiek, D. L., 1985. Prediction of soil water properties for hydrologic modeling. In: *Watershed Management in the Eighties*, Jones, E. and Ward, T. J., eds. Reston, Virginia: ASCE Press.

Romme, W. H. and Despain, D. G., 1989. Historical perspective on the Yellowstone fires of 1988. *Bioscience*, **39**:695-699.

Romme, W. H., Turner, M. G., Gardner, R. H., Hargrove, W. W., Tuskan, G. A., Despain, D. G., and Renkin, R. A., 1997. A rare episode of sexual reproduction in aspen (*Populus tremuloides* Michx.) following the 1988 Yellowstone fires. *Natural Areas Journal*, **17**:17-25.

Schullery, P., 1989. The fires and fire policy. *Bioscience*, **39**:686-694.

Sellers, P. J., Los, S. O., Tucker, C. J., Justice, C. O., Dazlich, D. A., Collatz, G. J., and Randall, D. A., 1996. A revised land surface parameterization (SiB2) for atmospheric GCMs. Part II: The generation of global fields of terrestrial biophysical parameters from satellite data. *Journal of Climate*, **9**:706-737.

Shafer, M. A., Fiebrich, C. A., Arndt, D. S., Frederickson, S. E., and Hughes, T. W., 2000. Quality assurance procedures in the Oklahoma Mesonetwork. *Journal of Atmospheric and Oceanic Technology*, **17**:474-494.

Shovic, H. F., 1988. *Postfire soil research.* Greater Yellowstone Postfire Ecological Assessment Workshop, Yellowstone National Park, Wyoming.

Shukla, J. and Mintz, Y., 1982. The influence of land surface evapotranspiration on Earth's climate. *Science*, **215**:1498-1501.

Singer, F. J. and Harter, M. K., 1996. Comparative effects of elk herbivory and 1988 fires on northern Yellowstone National Park grasslands. *Ecological Applications*, **6**:185-199.

Singh, A. K., 1999. An investigation of the thermal conductivity of snow. *Journal of Glaciology*, **45**:345-351.

Smith, E. A., Crosson, W. L., Cooper, H. J., and Weng, H.-Y., 1993. Estimation of surface heat and moisture fluxes over a prairie grassland. Part III: Design of a hybrid physical/remote sensing biosphere model. *Journal of Geophysical Research*, **98**:4951-4978.

Soil Survey Staff, 1998. *Soil Survey Handbook.* U.S. Department of Agriculture, Natural Resources Conservation Service, Handbook 18. Washington, DC: U.S. Government Printing Office.

Storck, P. and Lettenmaier, D. P., 1999. Predicting the effect of forest canopy on ground snowpack accumulation and ablation in maritime climates. *Proceedings of the Western Snow Conference*, **67**:1-12.

Sturm, M., Holmgren, J., König, M., and Morris, K., 1997. The thermal conductivity of seasonal snow. *Journal of Glaciology*, **43**:26-41.

Tarboton, D. G. and Luce, C. H., 1996. *Utah Energy Balance snow accumulation and melt model (UEB), computer model technical description and users guide.* Utah Water Research Laboratory and USDA Forest Service Intermountain Research Station. Available from: <http://www.engineering.usu.edu/dtarb/snow.html>.

Taylor, D. L., 1974. Forest fires in Yellowstone National Park. *Journal of Forest History*, **18**:69-77.

Tucker, C. J., 1979. Red and photographic infrared linear combinations for monitoring vegetation. *Remote Sensing of the Environment*, **8**:127-150.

U.S. Army Corps of Engineers. 1956. *Snow Hydrology*. Portland, Oregon: U.S. Army Corps of Engineers, North Pacific Division.

USDA-NRCS, 1994. *State Soil Geographic (STATSGO) Database: Data Use Information*. Misc. Publ. 1492. Fort Worth, Texas: National Cartography and GIS Center.

USGS, 2001. *HYDRO1k Documentation*. Available from: <http://edcdaac.usgs.gov/gtopo30/hydro/readme.html>.

Walker, J. M. and Rowntree, P. R., 1977. The effect of soil moisture on circulation and rainfall in a tropical model. *Quarterly Journal of the Royal Meteorological Society*, **103**:29-46.

Wotton, B. M. and Flannigan, M. D., 1993. Length of fire season in a changing climate. *The Forestry Chronicle,* **69**:187-192.

Wu, Y., Turner, M. G., Wallace, L. L. and Romme, W. H., 1996. Elk Survival Following the 1988 Yellowstone Fires: A Simulation Experiment. *Natural Areas Journal*, **16**:198-207.

Xue, Y., Sellers, P. J., Kinter III, J. L., and Shukla, J., 1991. A Simplified Biosphere Model for Global Climate Studies. *Journal of Climate*, **4**:345-364.

Yang, Z.-L., Dickinson, R. E., Robock, A., and Vinnikov, K. YA., 1997. Validation of the snow submodel of the Biosphere–Atmosphere Transfer Scheme with Russian snow cover and meteorological observational data. *Journal of Climate*, **10**:353-373.

Yeh, T. C., Wetherald, R. T., and Manabe, S., 1984. The effect of soil moisture on the short-term climate and hydrology change – a numerical experiment. *Monthly Weather Review*, **112**:474-490.

Yellowstone National Park Spatial Analysis Center, 2003. *1988 Fire Perimeter Map of Yellowstone National Park, Wyoming, Montana, Idaho*. Available from <http://www.nps.gov/gis/park_gisdata/wyoming/yell.htm>.

Zheng, X. and Eltahir, E., 1998. A soil moisture–rainfall feedback mechanism: 2. Numerical experiments. *Water Resources Research*, **34**:777–785.